UC Merced

UC Merced Electronic Theses and Dissertations

Title

Friction Induced Structural Transformation of Bulk Nanostructured MoS2 for Hydrogen Evolution Reaction

Permalink

https://escholarship.org/uc/item/3zx817p2

Author

Limsakoune, Vipawee

Publication Date

2018

Copyright Information

This work is made available under the terms of a Creative Commons Attribution-NonCommercial-ShareAlike License, availalbe at https://creativecommons.org/licenses/by-nc-sa/4.0/

Peer reviewed|Thesis/dissertation

eScholarship.org Powered by the California Digital Library
University of California

UNIVERSITY OF CALIFORNIA, MERCED

Friction Induced Structural Transformation of Bulk Nanostructured MoS_2 for Hydrogen Evolution Reaction

A dissertation submitted in partial satisfaction of the requirements
for the degree Doctor of Philosophy

in

Biological Engineering and Small-scale Technologies

by

Vipawee Limsakoune

Committee in charge:

Dr. Christopher Viney, Chair
Dr. Erik Menke
Dr. Min-Hwan Lee

2018

© Vipawee Limsakoune, 2018
All rights reserved.

The dissertation of Vipawee Limsakoune is approved, and it is acceptable in quality and form for publication on microfilm and electronically:

_____

Min-Hwan Lee Date

_____

Erik Menke Date

_____

Christopher Viney, Chair Date

University of California, Merced

Fall 2018

Acknowledgements

Biological Engineering and Small-scale technologies (BEST) Summer Fellowship 2013, travel award 2016. Teaching assistant opportunities from Fall 2012 to Spring 2018.
Dr. C. Viney for his help to follow up on progress, encourage, suggest experiments to prove hypothesis, share knowledge, and share experience with me.
Dr. V. Tung for his help to suggest articles to read, support on chemical, tools, and materials characterization.
Dr. E. Menke for his help to suggest articles to read, encourage, suggest experiments to prove hypothesis, allowing me to use electrochemical testing equipment.
Dr. M.-H. Lee for his help to encourage, share knowledge with me about EIS, and LSV.
Dr. J. Lu for her help to encourage, share knowledge with me about chemical synthesis, characterization, allowing me to use sample holder and Pt mesh.
Dr. K. McCloskey for suggesting me to be a graduate student mentor and connecting me with an experienced mentor.
Dr. H. Ishihara for his help to encourage, share knowledge with me about electrospray, chemical synthesis, creativity, and problem solving.
Dr. Y.-C. Chen, W. Zhan, X. Wei, J. Fu for their help to encourage, share knowledge with me about electrospray, chemical synthesis, and materials characterization.
B. Frank for his help to share knowledge with me about taking high quality photos.
J. Serrano for his help to share knowledge with me about creativity and problem solving.
W. Chen for sharing knowledge with me about summarizing literature in table form.
Y. Zeng, Dr. L. Reed, and M. Prado for their help to encourage and share knowledge with me about chemical synthesis.
P. Phummirat, C. Wu, K. Shirzad, B. Morales Perez, Dr. E. Reed, S. Wang, J. Perez. for their help to encourage me.
J.F. Flores, Y. Liu, Dr. J. Komadina, S. Sarang, K. Nikolaidou, A. Macedo Andrade, S. Grewal, K. Nguyen, and M. Dunlap for their help to encourage, share knowledge with me about chemical synthesis and characterization.
J. Hernandez for his help to encourage and share knowledge with me about literature searching.
J. Son for his help to encourage and share knowledge with me about open mind for constructive criticism.
Dr. L. Wong, R. Hatano, Dr. U.S. Ramasamy, V. Lopez, Dr. E. Gibb, J.F. Flores, S. Safar, W. Guan, J. Ramirez, L. Jin, R. Gupta, Dr. D. Davidian, D. Morgan, Dr. C. Melton, J. Pazzi, A. Karimaghaloo, M. Bartolo, N. Mothi, C. Ortuno-Quintana, Z. Slim, A.E. Tefera, T. Lien for their help to encourage and share knowledge with me about graduate student experience.
Dr. J. Shao for her help to share knowledge with me about AFM.
Dr. M.D. Moreno for his help to share knowledge with me about qualifying exam and TA preparation.
M. Manansala for his help to encourage, share knowledge with me about fixing Au sputter coating equipment.
T. Kou, M. Xu, A. Winek, Dr. C. Koehler, Dr. M. Zatz, Dr. C. Kello for their help to encourage, share knowledge with me about communication and writing.
Parents, siblings, relatives, friends, former teachers, TAs and students when I was a TA.

To people who are interested in materials synthesis and electrochemistry

Curriculum Vitae

EDUCATION

Ph.D. in Biological Engineering and Small-scale Technologies
University of California, Merced, California, USA August 2012 – Expected December 2018
M.S. in Petrochemical Technology
The Petroleum and Petrochemical College**,** Chulalongkorn University, Thailand.May 2010-April 2012
Coursework: Chemical Reaction Engineering, Advanced Chemical Engineering Thermodynamics, Transport Phenomena, Surfactant Science and Technology,
and Heterogeneous Catalysis. GPA 3.69/4.0
B.Eng. in Chemical engineering
King Mongkut's Institute of Technology Ladkrabang, Bangkok, Thailand March 2010
Coursework: Chemical Engineering Kinetics and Reactor Design, Heat and Mass Transfer, Fluid Mechanics, Thermodynamics, Waste Treatment and Pollution Control and Safety in Chemical Engineering GPA 3.11/4.0

ACADEMIC PROJECTS

- Working on unique aspects for electrode platform for energy harvesting
  - To optimize crumpled MoS_2 electrode for Hydrogen Evolution Reaction (HER)
  - To fabricate 3D Crumpled Graphene Nanostructure (CGNs) to use for photoanode
- 3D electrodes with densely packed nanoredox centers for green energy storage
  - To fabricate a 3D electrode platform to use for pseudocapacitor
- Study asphaltene instability by capillary deposition
  - To understand the mechanisms of asphaltene deposition to improve prediction and prevention of deposits
- Adsorption of α–Tocopherol on Silica from Rice Hull Products
  - To synthesize silica from rice hull products to use for adsorbing nutrients from palm oil

PROFESSIONAL EXPERIENCE

- **Teaching Assistant:** General Chemistry I (CHEM 002), Preparatory Chemistry (CHEM 001), Introduction to Nanotechnology and Nanoscience (MSE 118), Materials Thermodynamics (MSE 109), Introduction to Materials (ENGR 45), Capstone Project (MSE 120), Engineering Service Learning (ENGR 97/197)
  University of California, Merced, Merced, USA. August 2012-May 2018
- **MACES outreach programs with high school teachers** August 2016-November 2016
- **Graduate Peer Mentor** Spring 2016
- **Visiting Scholar in Chemical Engineering Department**
  Research: Petroleum Deposition
  University of Michigan, Ann Arbor, Michigan, USA. March 2011-March 2012
- **Thailand Institute of Scientific and Technological Research (TISTR)** April 2009 -May 2009
  Edited Sub-patent about Disposal of Sulfur Dioxide by using Ozone
  - Sulfur dioxide can be disposed by ozone to reduce environmental problem

  Edited Sub-patent about Continuously Wine Fermenting
  - To understand fermentation process and reduce cost of operation in wine production

AWARD/FELLOWSHIP

- Biological Engineering and Small-scale technologies (BEST) Summer Fellowship — Summer 2013
- Biological Engineering and Small-scale technologies (BEST) Summer Travel Award — May 2016

ANALYTICAL SKILLS

Experienced user of Scanning Electron Microscopy (SEM), Linear Sweep Voltammetry (LSV), Cyclic Voltammetry (CV), Electrochemical Impedance Spectroscopy (EIS), Fourier Transform Infrared Spectroscopy (FTIR), Thermogravimetric Analysis (TGA), Atomic Force Microscopy (AFM), Ultraviolet-Visible Spectroscopy (UV-Vis), Optical Microscopy

COMPUTER SKILLS

Aspen HYSYS, Microsoft Visio, MATLAB, C/C++

PUBLICATIONS AND PRESENTATIONS

- Contributing Author "Electrohydrodynamic-assisted Assembly of Hierarchically Structured, 3D Crumpled Nanostructures for Efficient Solar Conversions" *Scientific Reports*, **2016**, 6, pp 38701
- Second author "A Fundamental Study of Asphaltene Deposition" *Energy Fuels*, **2013**, 27 (2), pp 725
- Contributing Author "Direct Growth of Carbon Electrodes for Battery Applications", Electrochemical Society (ECS) Conference, 2013
- Guest Speaker in Special Topics: Materials (graduate level class, BEST 201, Fall 2018)

PROFESSIONAL ASSOCIATIONS

Society of Women Engineering (SWE) — February 2015-Present

Abstract

Friction Induced Structural Transformation
of Bulk Nanostructured MoS_2 for Hydrogen Evolution Reaction

Doctor of Philosophy

in

Biological Engineering and Small-scale Technologies

by

Vipawee Limsakoune

Professor Christopher Viney, Chair

University of California, Merced 2018

MoS_2 is a good candidate for Hydrogen Evolution Reaction (HER) catalyst because it has low overpotential at 10 mA/cm^2 and low Tafel slope close to platinum, is inexpensive, and is abundant. High surface area and mass loading of the Friction Induced Structural Transformation of crumpled MoS_2 (FIST c-MoS_2) could lower the overpotential at 10 mA/cm^2 and Tafel slope compared to c-MoS_2 and chemically exfoliated MoS_2 (ce-MoS_2). In this work, MoS_2 catalysts are synthesized at room temperature to preserve active basal plane for hydrogen adsorption. The overpotential at 10 mA/cm^2 of the catalyst after cyclic voltammetry is -196 mV vs. Reversible Hydrogen Electrode (RHE); the Tafel slope is 91.9 mV/dec, and the exchange current density is 75.9 μA/cm^2 in 0.5 M H_2SO_4 electrolyte. After cyclic voltammetry from +0.2 V to -0.3 V vs. RHE for 1,000 cycles, FIST c-MoS_2 on ce-MoS_2, c-MoS_2 on ce-MoS_2, and ce-MoS_2, all on carbon cloth, show similar overpotential at 10 mA/cm^2, and similar Tafel slope. MoS_2 catalysts from this work exhibit among the lowest overpotentials at 10 mA/cm^2 of MoS_2 based catalysts. Capacitance data derived from EIS plots reveal that cyclic voltammetry leads to an increased surface area of all the MoS_2 catalysts. The increased surface area promotes low overpotential at 10 mA/cm^2, and high exchange current density.

Statement of Originality and Collaboration

All experiments presented in this dissertation are original works of the author, with the exception of experiments contributed by Dr. V. Tung (see pages 22, 45, and 46) and experiments contributed by X. Wei (see page 47) while working in collaboration with me.

Table of Contents

Chapter 1: Review of MoS_2 as Hydrogen Evolution Reaction (HER) Catalyst 1

1.1 Hydrogen Evolution Reaction (HER) 1

1.2 Challenges of c-MoS_2 22

1.3 Hypothesis 22

1.4 Preliminary work 22

1.4.1 Raman Spectra 22

1.4.2 Scanning electron microscopy (SEM) images 23

Chapter 2: Methods 24

2.1 Chemically exfoliated Molybdenum disulfide (ce-MoS_2) synthesis 24

2.1.1 Lithiation 24

2.1.2 Exfoliation 24

2.1.3 Purification 24

2.2 Substrate preparation 24

2.2.1 ce-MoS_2 on carbon cloth substrate 24

2.2.2 Stainless steel substrate 25

2.2.3 Si substrate 25

2.2.4 Purpose of different substrates 25

2.3 Crumpled Molybdenum disulfide (c-MoS_2) preparation 26

2.4 Friction induced structural transformation of c-MoS_2 (FIST c-MoS_2) 27

2.5 Vertical force from a cylindrical steel mass 27

2.6 Electrohydrodynamic (EHD) 28

2.7 Scanning electron microscopy (SEM), X-ray Energy-dispersive spectroscopy (EDS) 29
2.8 Atomic force microscopy (AFM) 30
2.9 Linear Sweep Voltammetry (LSV) 31
2.10 Cyclic Voltammetry (CV) 34
2.11 Electrochemical Impedance Spectroscopy (EIS) 35
2.11.1 Capacitance calculation 39
2.12 Raman spectroscopy 40
2.13 X-ray diffraction (XRD) 41
2.14 Ultraviolet and visible light spectroscopy (UV-VIS) 42

Chapter 3: Results and Discussions 43
3.1 SEM of bulk MoS_2 powder and ce-MoS_2 sheets 43
3.2 AFM of ce-MoS_2 sheets 43
3.3 SEM of c-MoS_2 and FIST c-MoS_2 45
3.4 EDS of FIST c-MoS_2 45
3.5 Raman Spectra of c-MoS_2 and FIST c-MoS_2 46
3.6 XRD spectra of ce-MoS_2, c-MoS_2 and FIST c-MoS_2 47
3.7 Effect of sonication on filter paper mass 48
3.8 HER activity of c-MoS_2 and FIST c-MoS_2 on stainless steel 49
3.9 HER activity and evidence for degradation of the electrode with LSV and EIS 54
3.10 HER activity after CV 61
3.11 Effect of the number of ce-MoS_2 dip coat steps on HER activity 80

3.12 Effect of the ce-MoS_2 coat drying temperature on HER activity 86

3.13 Materials selection charts 89

Chapter 4: Conclusions 95

Chapter 5: Outlook 96

5.1. Mass loading 96

5.2 Wettability 96

5.3 Pretreatment of the electrode 96

5.4 Effect of the temperature on HER activity 96

5.5 Conducting support 96

5.6 Cobalt-modified MoS_2 96

5.7 Preventing hydrogen bubbles from accumulating at the electrode surface 97

5.8 Substrate, geometric surface area and mass loading 97

5.9 Surface characterization 97

5.10 Charge transfer resistance of the electrode before and after CV 1,000 cycles 97

5.11 Possibility of scalable HER catalyst preparation 97

References 98

CHAPTER 1: Review of MoS_2 as Hydrogen Evolution Reaction (HER) Catalyst

1.1 Hydrogen Evolution Reaction

Hydrogen is a source of renewable energy. The different methods for producing hydrogen include natural gas reforming (Li et al., 2010), coal gasification (Badwal et al., 2014), and water electrolysis (Li et al., 2010). The latter can produce hydrogen without carbon dioxide as a byproduct (Li et al., 2010). Catalysts are important for hydrogen evolution reaction (HER) because they increase the selectivity, efficiency and rate of the reaction. Platinum is the benchmark for HER catalyst because of its low overpotential at 10 mA/cm^2 and low Tafel slope (Kong et al., 2014; Conway et al., 2002; Norskov et al., 2005).

HER consists of hydrogen adsorption and desorption steps on electrode surface in acid electrolyte (Li et al., 2011):

The hydrogen adsorption step

$H_3O^+ + e^- \rightarrow H_{ads} + H_2O$ (Volmer reaction)

The hydrogen desorption step

$H_3O^+ + H_{ads} + e^- \rightarrow H_2 + H_2O$ (Heyrovsky reaction)

or

$H_{ads} + H_{ads} \rightarrow H_2$. (Tafel reaction)

where H_{ads} is a hydrogen atom adsorbed at the electrode surface.

The hydrogen desorption step can be identified with the Tafel slope value discussed in Chapter 2. A Gibbs free energy of hydrogen adsorption, ΔG_H close to 0 eV is required so that the hydrogen atoms are not adsorbed on the surface too strongly or loosely. If the adsorption is too strong, the desorption step becomes more rate limiting for HER. If the adsorption is too weak, the adsorption step becomes more rate limiting. Figure 1.1 shows the volcano plot of the exchange current density as a function of ΔG_H for nanoparticulate MoS_2 and several metals (Jaramillo et al., 2007). The ΔG_H on Pt surface is close to 0 eV (Norskov et al., 2005). However, platinum is expensive ($292 per gram, powder, 99.995% trace metals basis, Sigma Aldrich, November 2018) and scarce. MoS_2 on the other hand has the catalytic efficiency close to platinum (Jaramillo et al., 2007; Bonde et al., 2008), and is inexpensive ($0.60 per gram, powder, < 2 μm, 99%, Sigma Aldrich, November 2018) and abundant. Jaramillo et al. reported that the exchange current density of MoS_2 grown on Au(111) substrate correlates linearly with MoS_2 edge length (Jaramillo et al., 2007).

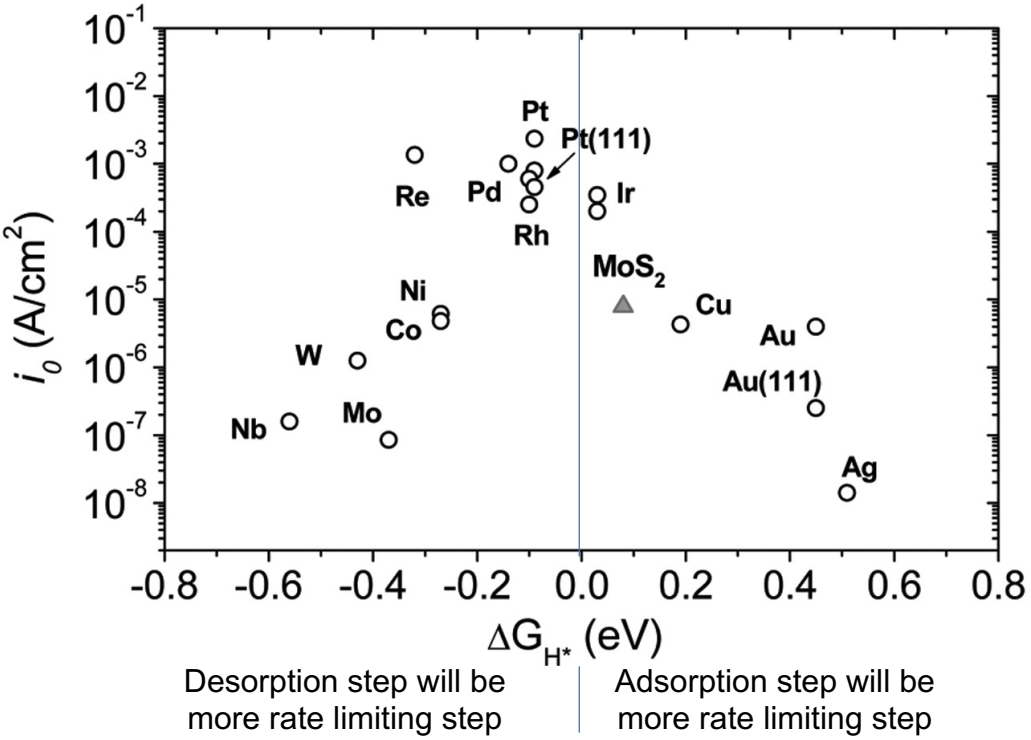

Figure 1.1. Volcano plot of the exchange current density as a function of ΔG_H for nanoparticulate MoS_2 and several metals (after Jaramillo et al., 2007).

The polymorph of MoS_2 commonly found in nature is 2H, which has trigonal prismatic molecular geometry of the S–Mo–S unit; H stands for hexagonal crystal system. The digit indicates the number of S–Mo–S units in the unit cell (Chhowalla et al., 2013). 2H-MoS_2 has a ΔG_H of 0.06 eV at the edges (catalytically active), contrasting with 1.92 eV at the inactive basal plane (Tsai et al., 2014a, b). Kong, D., et al. synthesized vertically aligned 2H-MoS_2 to maximize edge sites (Kong et al., 2013). The catalytic performance of the vertically aligned 2H-MoS_2 catalyst is summarized in Table starting on page 8. Figure 1.2 shows the structure of edge-terminated 2H-MoS_2.

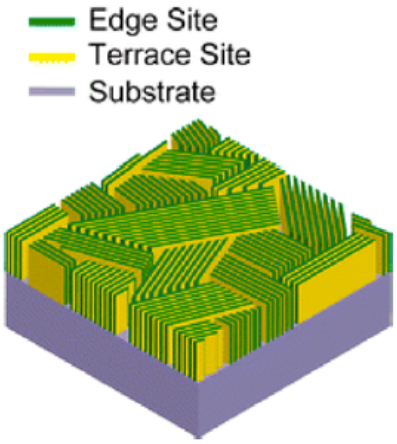

Figure 1.2. Illustration of edge-terminated 2H-MoS_2 (Kong et al., 2013). The Terrace sites are parallel to the basal plane.

MoS_2 is a lamellar solid which can be exfoliated into sheets by mechanical exfoliation (Ottaviano et al., 2017; Novoselov et al., 2005) or chemical exfoliation (Chou et al., 2015).

Lithium intercalation and exfoliation (an example of chemical exfoliation) of 2H-MoS_2 leads to a change in the molecular geometry from trigonal prismatic (2H-MoS_2) to octahedral (1T-MoS_2). T stands for trigonal crystal system. Chou et al. used Density Functional Theory (DFT) to predict the possible polymorphs of 2H-MoS_2 after lithium intercalation and exfoliation (Chou et al., 2015). Figure 1.3 shows the polymorphs. The 2H and 1T consist of 1 by 1 unit cells. 1T' consists of a 2 by 1 supercell. 1T" consists of a 2 by 2 supercell.

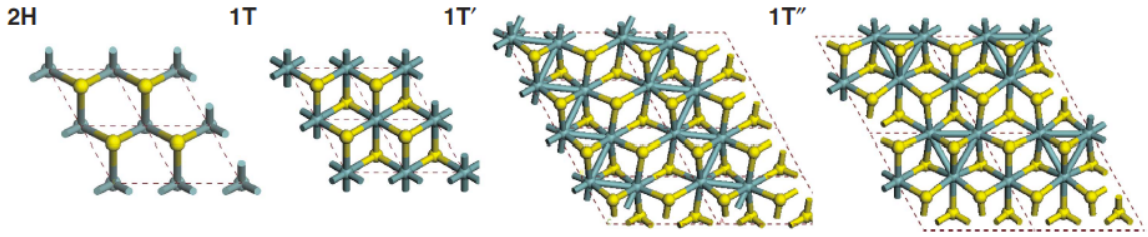

Figure 1.3. The polymorphs of MoS_2. Mo atoms are in teal color. S atoms are in gold color (Chou et al., 2015).

Chou et al. reported that 1T phase relaxes into 1T" which is second in the stability then 1T" relaxes into 1T' (Chou et al., 2015). The ΔG_H on the basal plane of 2H-MoS_2 is 1.6 eV. The ΔG_H on the basal plane of 1T'-MoS_2 is 0.18 eV (Chou et al., 2015).

Yin et al. reported that 1T'-MoS_2 single-layer or few-layer nanosheet samples have higher catalytic performance than 2H-MoS_2 nanosheet samples (Yin et al., 2016). The catalytic

performance of the 1T'-MoS_2 nanosheets and 2H-MoS_2 nanosheets are summarized in Table starting on page 8. Figure 1.4 shows the structure of 1T'-MoS_2 nanosheets.

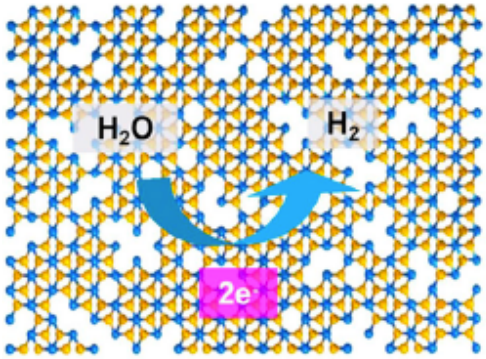

Figure 1.4. Illustration of 1T'-MoS_2 nanosheet (Yin et al., 2016). Mo atoms are in blue color. S atoms are in orange color.

Xiang et al. reported that Li-MoS_2 nanosheets on carbon cloth have higher catalytic performance than 2H-MoS_2 nanosheet samples (Xiang et al., 2016). The catalytic performance of the Li-MoS_2 nanosheets and 2H-MoS_2 nanosheets is summarized in Table starting on page 8.

Li et al. reported that the sulfur (S) vacancies are catalytic sites in the basal plane of 2H-MoS_2 (Li et al., 2016). Figure 1.5 shows the structure of 2H-MoS_2 with strained S-vacancies on the basal plane.

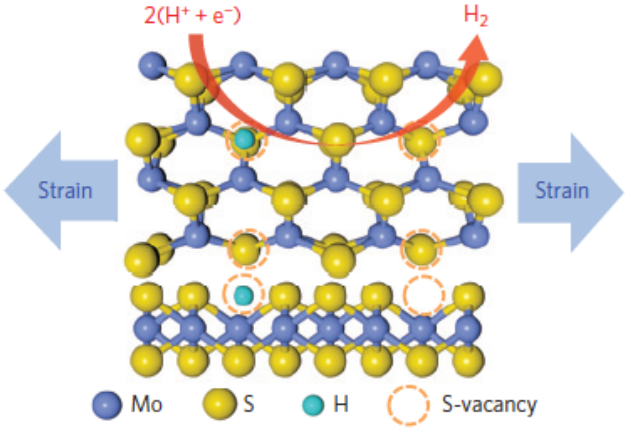

Figure 1.5. Schematic of 2H-MoS_2 with strained S-vacancies on the basal plane (Li et al., 2016).

Density functional theory (DFT) calculations indicate that S-vacancies introduce gap states, promoting hydrogen adsorption. Increasing the number of S-vacancy sites strengthens hydrogen adsorption thus reducing free energy for hydrogen adsorption

(Li et al., 2016). Figure 1.6 shows the free energy diagram of hydrogen evolution reaction for S-vacancy concentrations ranging from 0.00% to 25.00%.

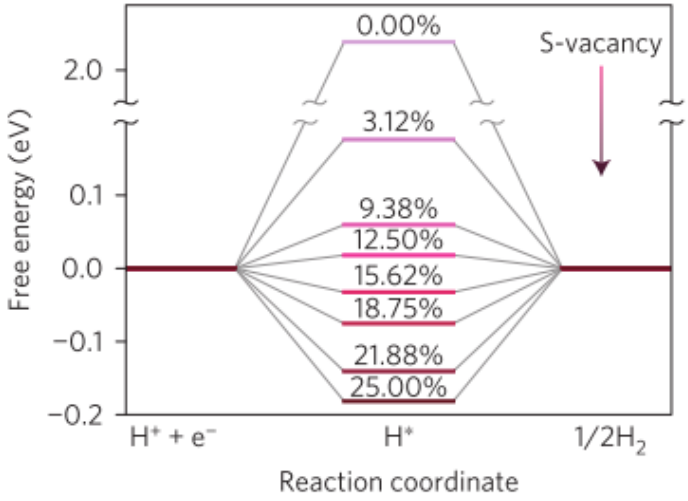

Figure 1.6. Free energy diagram of hydrogen evolution reaction (Li et al., 2016).

The free energy for hydrogen adsorption can be further adjusted by straining S-vacancy sites (Li et al., 2016). Figure 1.7 shows ΔG_H vs. %x-strain for S-vacancy concentrations ranging from 0.00% to 18.75%, calculated using density functional theory (DFT). The quantity "x-strain" is the uniaxial tensile strain along the x-axis. The increase in the strain leads to the lower overpotential at 10 mA/cm^2 and lower Tafel slope.

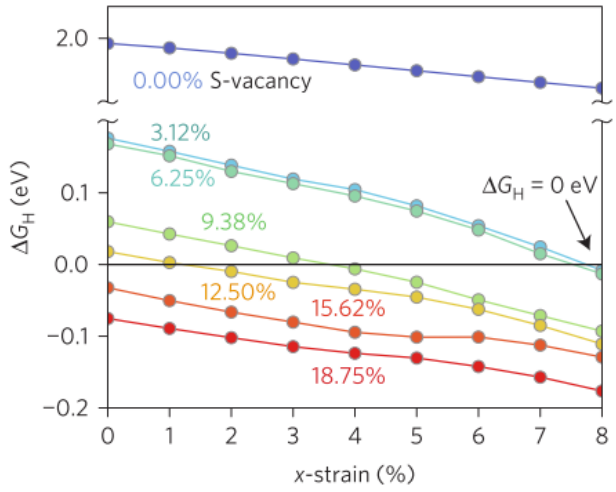

Figure 1.7. The plot of ΔG_H vs. %x-strain for S-vacancy concentrations ranging from 0.00% to 18.75% (Li et al., 2016).

The catalytic performance of the 2H-MoS_2 with strained S-vacancies catalyst is summarized in Table starting on page 8.

Chen et al. reported an electrohydrodynamically-induced dimensional transition of 2H-MoS_2 to crumpled MoS_2 (c-MoS_2) (Chen et al., 2017). c-MoS_2 has the average S-vacancy 9.3 ± 1.7% and 3.7% strain. Figure 1.8 shows schematic illustration of c-MoS_2.

Figure 1.8. Schematic of crumpled MoS_2 (c-MoS_2) (Chen, Y.-C. et al., 2017).

The catalytic performance of the 2H c-MoS_2 and 2H planar MoS_2 catalysts are summarized in Table starting on page 8.

Gao et al. reported a quasi-amorphous MoS_2 and $CoSe_2$ hybrid catalyst (Gao et al., 2015). Co can couple with S-edges to lower their ΔG_H from 0.18 eV to 0.10 eV (Bonde et al., 2008). The catalytic performance of the quasi-amorphous MoS_2 and $CoSe_2$ hybrid catalyst is summarized in Table starting on page 8.

Li et al. reported electrochemically polarizing 2H-MoS_2 at negative potentials (vs. RHE) in acid media is a proton intercalation process (p-doped). They observed lower overpotential at 10 mA/cm^2 after 1,000 cycles of cyclic voltammetry from 0 V to -0.5 V vs. RHE on glassy carbon substrate. X-ray diffraction (XRD) measurement shows that the interlayer spacing increases by 0.01 nm on average after the proton intercalation process (Li et al., 2017). Photoluminescence (PL) measurement shows the displacement of the PL spectra to shorter wavelength (blueshift) after the proton intercalation process. The proton intercalation may neutralize the free electrons in MoS_2 to promote the emission of neutral excitons over trions (negatively charged excitons). The emission of neutral excitons shows the shorter emission PL wavelengths than the emission of trions (Li et al., 2017). X-ray photoelectron spectroscopy (XPS) measurement shows the displacement of the XPS spectra to lower binding energy after the proton intercalation process. The lowering in binding energy indicates a shift in the Fermi level toward the valence band; an equivalent shift occurs when MoS_2 is p-doped (Nipane et al., 2016). Raman spectra before vs. after the cycling show negligible shift indicating that there is no change from 2H to 1T' in the MoS_2 (Li et al., 2017). The catalytic performance of the 2H-MoS_2 flake and reduced 2H-MoS_2 flake catalysts is summarized in Table starting on page 8.

Tsai et al. reported lower overpotential at 10 mA/cm^2 of monolayer 2H-MoS_2 after applying -1.0 V vs. RHE for 10 minutes, compared to as-synthesized 2H-MoS_2. XPS measurement shows that the sample after applied negative potential has weaker S 2p peaks than the as-synthesized sample. The XPS measurement confirms that the sulfur atoms are electrochemically reduced after applied negative potential. Raman spectra before vs. after applied negative potential show negligible shift indicating that there is no change from 2H to 1T' in the MoS_2 (Tsai et al., 2017).

Voiry et al. synthesized partially oxidized 2H-MoS_2 sheets by saturating MoS_2 solution with oxygen for a few days. They observed that the overpotential at 10 mA/cm^2 of partially oxidized 2H-MoS_2 sheets on glassy carbon substrate is higher than without partially oxidized MoS_2 sheets (Voiry et al., 2013). The catalytic performance of the 2H-MoS_2 and partially oxidized 2H-MoS_2 catalysts is summarized in Table starting on page 8.

Chia et al. reported lower overpotential at 10 mA/cm^2 of 2H-MoS_2 on glassy carbon substrate after applying -1.2 V vs. Ag/AgCl for 600 seconds (Chia et al., 2014) or -1.3 V vs. Ag/AgCl for 300 seconds (Chia et al., 2015), compared to as-synthesized 2H-MoS_2. DFT calculations confirmed that the phase transition from 2H to 1T' by applying electrochemical potentials is possible (Chia et al., 2014). Raman spectra before vs. after applied negative potential show 2 cm^{-1} shift of A_{1g} peak toward lower wavenumber after applied negative potential (Chia et al., 2015) attributes to electron doping (Chakraborty et al., 2012). The catalytic performance of the 2H-MoS_2 and reduced 2H-MoS_2 catalysts are summarized in Table starting on page 8.

Table 1.1. Catalytic performance of MoS_2 based catalysts for HER. Articles arranged in chronological order.

No.	Catalyst	Overpotential at 10mA/cm^2 (mV vs. RHE)	Tafel slope (mV per dec)	Exchange current density (μA/cm^2)	Potential for EIS (V vs. RHE)	Charge-transfer resistance (Ω)	Capacitance (mF/cm^2)	Mass loading (μg/cm^2)	Active sites (sites /cm^2)	Turnover frequency (1/s)	Cycles	Ref.
1	FIST c-MoS_2	-526	95.5	0.0320	0 V vs. OCP	>784	9.42	195, 185	N/A	N/A	10	This work
1a	FIST on ce-MoS_2 5x	-735	135	0.0359	N/A	N/A	N/A	N/A	N/A	N/A	1	This work
1b	FIST on ce-MoS_2 1x	-624	99.7	0.00560	N/A	N/A	N/A	N/A	N/A	N/A	1	This work
2	Reduced FIST c-MoS_2	-196	91.9	75.9	0 V vs. OCP	>383	12.5	N/A	N/A	N/A	1000	This work
3	c-MoS_2	-737	104	0.000762	N/A	N/A	N/A	154	N/A	N/A	10	This work
3a	c-MoS2 on ce-MoS_2 5x	-745	134	0.0276	N/A	N/A	N/A	N/A	N/A	N/A	1	This work
3b	ce-MoS_2 1x	-631	127	0.104	N/A	N/A	N/A	N/A	N/A	N/A	1	This work
4	Reduced c-MoS_2	-264	109	34.6	N/A	N/A	N/A	N/A	N/A	N/A	1000	This work
5	ce-MoS_2	-548	96.5	0.0216	0 V vs. OCP	>858	7.85	169, 181	N/A	N/A	10	This work
5a	ce-MoS_2 5x	-761	148	0.0687	N/A	N/A	N/A	N/A	N/A	N/A	1	This work
5b	ce-MoS_2 1x	-666	114	0.0149	N/A	N/A	N/A	N/A	N/A	N/A	1	This work
6	Reduced ce-MoS_2	-194	109	168	0 V vs. OCP	>560	9.01	N/A	N/A	N/A	1000	This work

Table 1.1. (continued)

No.	Catalyst	Overpotential at 10mA/cm^2 (mV vs. RHE)	Tafel slope (mV per dec)	Exchange current density (μA/cm^2)	Potential for EIS (V vs. RHE)	Charge-transfer resistance (Ω)	Capacitance (mF/cm^2)	Mass loading (μg/cm^2)	Active sites (sites/cm^2)	Turnover frequency (1/s)	Cycles	Ref.
7	2H-MoS_2 flake	-400	95	0.13	N/A	N/A	N/A	N/A	N/A	N/A	1	Li et al., 2017
8	Reduced 2H-MoS_2 flake	-370	82	4.4	N/A	N/A	N/A	N/A	N/A	N/A	1000	Li et al., 2017
9	2H c-MoS_2 (250˚C)	-191	64	10.4	0.25	13	11.4	13	$5.8 * 10^{17}$	0.130 (-200 mV)	5000	Chen et al., 2017
10	2H Planar MoS_2	-364	108	0.7	0.25	275	0.091	15	$1 * 10^{14}$	0.016 (-200 mV)	<1000	Chen et al., 2017
11	Li-MoS_2 CC	-97	38	N/A	0.15	5	21	4000	N/A	N/A	1000	Xiang et al., 2016
12	P-2H-MoS_2 nanosheets	-218	62	10.5	0.25	280	8.2	140	$2.3 * 10^{14}$	N/A	1000	Yin et al., 2016

Table 1.1. (continued)

No.	Catalyst	Overpotential at 10mA/cm^2 (mV vs. RHE)	Tafel slope (mV per dec)	Exchange current density (μA/cm^2)	Potential for EIS (V vs. RHE)	Charge-transfer resistance (**Ω**)	Capacitance (mF/cm^2)	Mass loading (μg/cm^2)	Active sites (sites/cm^2)	Turnover frequency (1/s)	Cycles	Ref.
13	P-1T'-MoS_2 nanosheets	-153	43	15.8	0.25	16	63.1	140	$5.8 * 10^{16}$	0.5 (-153 mV)	1000	Yin et al., 2016
14	Strained 2H-MoS_2	-170	60	50-60	N/A	N/A	N/A	N/A	$3.1 * 10^{14}$	0.31 (0 mV)	N/A	Li et al., 2016
15	MoS_2/$CoSe_2$	-68	36	73	OCP	>200	N/A	280, 1000	N/A	N/A	N/A	Gao et al., 2015
16	Reduced 2H-MoS_2	-400	72	N/A	N/A	N/A	N/A	4	N/A	N/A	N/A	Chia et al., 2014
17	2H-MoS_2	-430	81	N/A	N/A	N/A	N/A	4	N/A	N/A	N/A	Chia et al., 2014
18	Partially oxidized 2H -MoS_2	-550	186	N/A	0.25	>1500	N/A	50	N/A	N/A	40	Voiry et al., 2013

Table 1.1. (continued)

No.	Catalyst	Overpotential at 10mA/cm^2 (mV vs. RHE)	Tafel slope (mV per dec)	Exchange current density (μA/cm^2)	Potential for EIS (V vs. RHE)	Charge-transfer resistance (**Ω**)	Capacitance (mF/cm^2)	Mass loading (μg/cm^2)	Active sites (sites/cm^2)	Turnover frequency (1/s)	Cycles	Ref.
19	2H - MoS_2	-380	75-85	N/A	0.25	>400	N/A	50	N/A	N/A	40	Voiry et al., 2013
20	Vertically aligned 2H-MoS_2	-400	105-120	2.2	0	>20	N/A	8.5	$5.4 * 10^{14}$	0.013 (0 mV)	1000	Kong et al., 2013
21	Li-MoS_2 CFP	-110	62	167	N/A	N/A	345	3880	N/A	N/A	1000	Wang et al., 2013
22	MoS_2 /RGO	-150	41	N/A	0.12	250	N/A	1000, 280	N/A	N/A	1000	Li et al., 2011

OCP stands for open circuit potential. N/A stands for not applicable.
Blue numbers are the data use in LSV. Red numbers are the data use in EIS at 0 V vs. OCP. Green numbers are the data use in Tafel slope.
Overpotential at 10 mA/cm^2, exchange current density and Tafel slope are total electrode properties. Active sites number and turnover frequency (TOF) are intrinsic properties. TOF describes how many H_2 molecules are catalytically generated per site per second (Ding et al., 2016).
Row number 7, 8, 16 and 17 are selected to present in the table because authors reported lower overpotential at 10 mA/cm^2 (see chapter 2 for significance of this number) after negative potential was previously applied to the electrode for a set period of time. Row number 18 and 19 are selected because authors observed higher overpotential at 10 mA/cm^2 after the electrode was partially oxidized. Row number 9 and 10 are selected because authors utilized the benefits of 3D nanostructure and strained S-vacancies. Row number 11,12,13, 17 and 21 are selected because authors utilized the benefits of 1T'-MoS_2. Row number 14 is selected because it explains the benefits of strained S-vacancies. Row number 15 and 22 are selected because they utilized the benefits of hybrid catalysts. Row number 20 is selected because it addresses the benefits of edges exposure. Row number 11 and 21 describe mass loading more than 1,000 μg/cm^2.

Figure 1.9 to figure 1.14 show the catalytic performance of MoS_2 based HER catalysts, which are essentially materials selection charts. The pairs of significant properties (overpotential at 10 mA/cm^2, Tafel slope, exchange current density and capacitance) are plotted in an effort to (i) summarize existing knowledge and (ii) identify trends and opportunities for improvement / optimization. The numbers associated with points in the Figures correspond to row numbers in Table 1.1.

Overpotential, η is the voltage that is sacrificed to overcome the activation energy associated with the electrochemical reaction (O'Hayre et al., 2009). In order to make hydrogen from water, catalysts are required to minimize the overpotential.

Tafel slope provides information on the additional voltage required to increase the catalytic current at the cathode by one order of magnitude (Benck et al., 2014; Chhowalla et al., 2013).

Exchange current density, j_0 is the current in the absence of net electrolysis and at zero overpotential. The exchange current density is a parameter that correlates to the electron-transfer rate of the catalyst under reversible conditions.

Capacitance reflects the charge separation between electrons and ions at the interface (O'Hayre et al., 2009).

Substrate and **mass loading** are important parameters when comparing the exchange current density of the electrodes. The substrate from row number 1 to 6, and 9 to 11 is carbon cloth. The substrate from row number 7, 8, 12, 13, and 15 to 20 is glassy carbon. The substrate from row number 21 is carbon fiber paper. The substrates from row number 22 are glassy carbon for Tafel plot and carbon fiber paper for linear sweep voltammetry (LSV) plot. The mass loading varies in the literature.

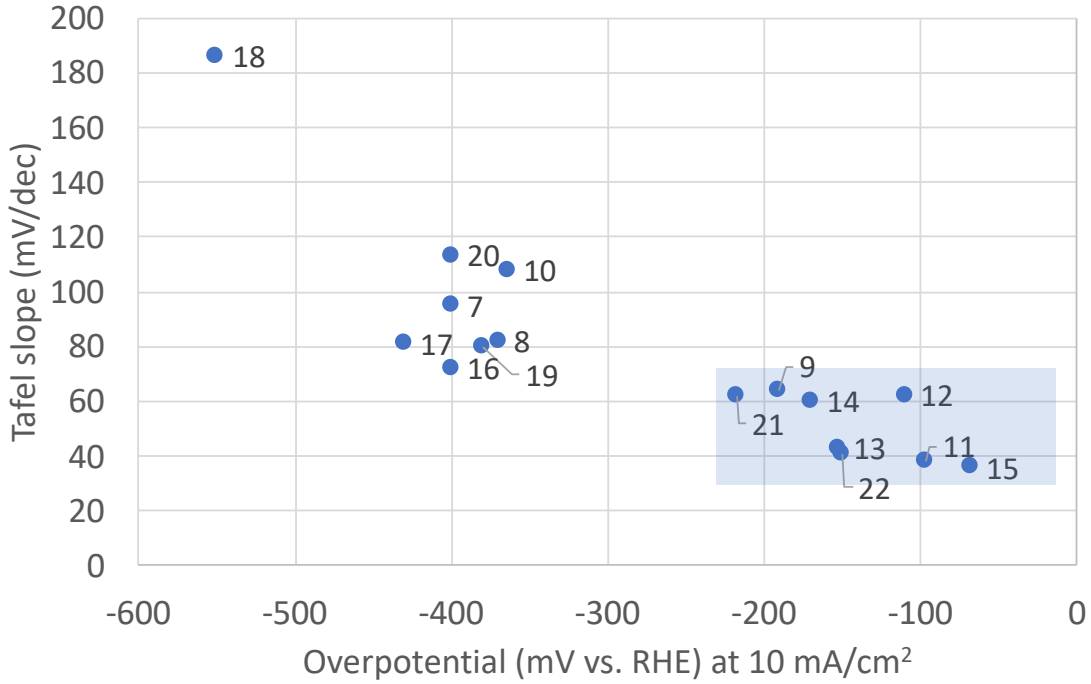

Figure 1.9. Overpotential at 10 mA/cm^2 and Tafel slope of MoS_2 based HER catalysts. A small Tafel slope indicates that the current density can increase rapidly with overpotential change (Suen et al., 2017). The shaded area denotes the promising HER catalyst because small overpotential (absolute value) and Tafel slope are desired for HER catalyst. Within this shaded area, (i) the minimum of the overpotential is the overpotential at 10 mA/cm^2 of Pt wire (Chhetri et al., 2017); (ii) the maximum of the overpotential is the overpotential at 10 mA/cm^2 of most MoS_2 based catalysts; (iii) the minimum of Tafel slope is the Tafel slope of Pt wire (Kong et al., 2014); (iv) the maximum of Tafel slope is the Tafel slope of most MoS_2 based catalysts.

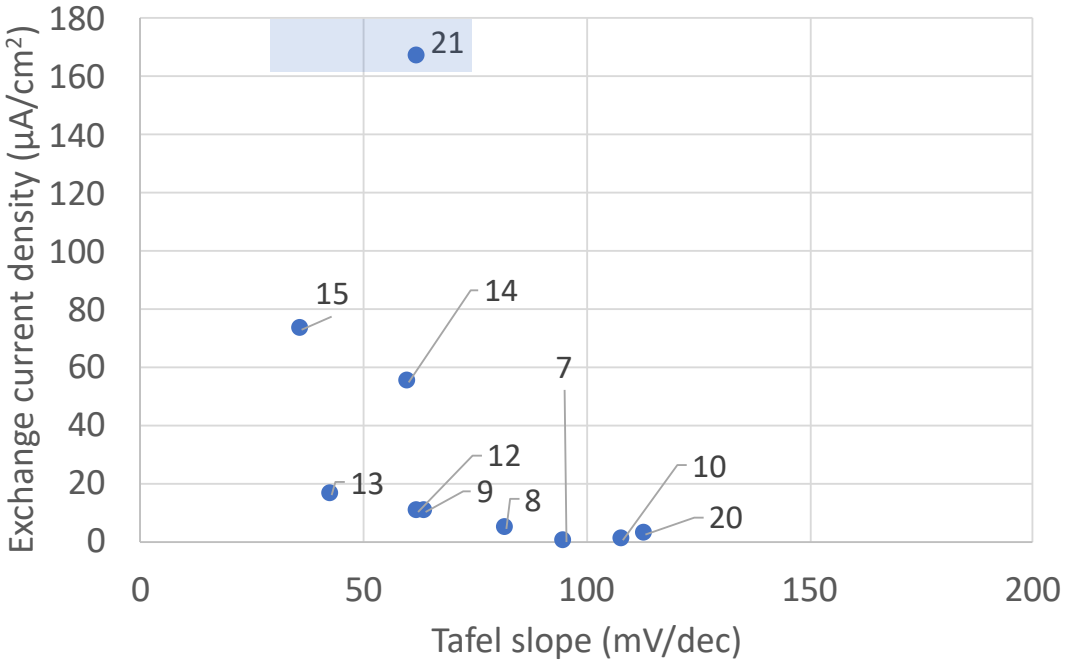

Figure 1.10. Exchange current density and Tafel slope of MoS_2 based HER catalysts. A large exchange current density reflects faster kinetics toward the redox reaction (Ding et al., 2016). The shaded area denotes the promising HER catalyst because small Tafel slope and large exchange current density are desired for HER catalyst. Within this shaded area, (i) the minimum of exchange current density is the exchange current density of Li-MoS_2 on carbon fiber paper (Wang et al. 2013); (ii) the maximum of exchange current density is the exchange current density of 10 wt% Pt/C (Hsu et al., 2012). The shade area of Tafel slope is the same as figure 1.9.

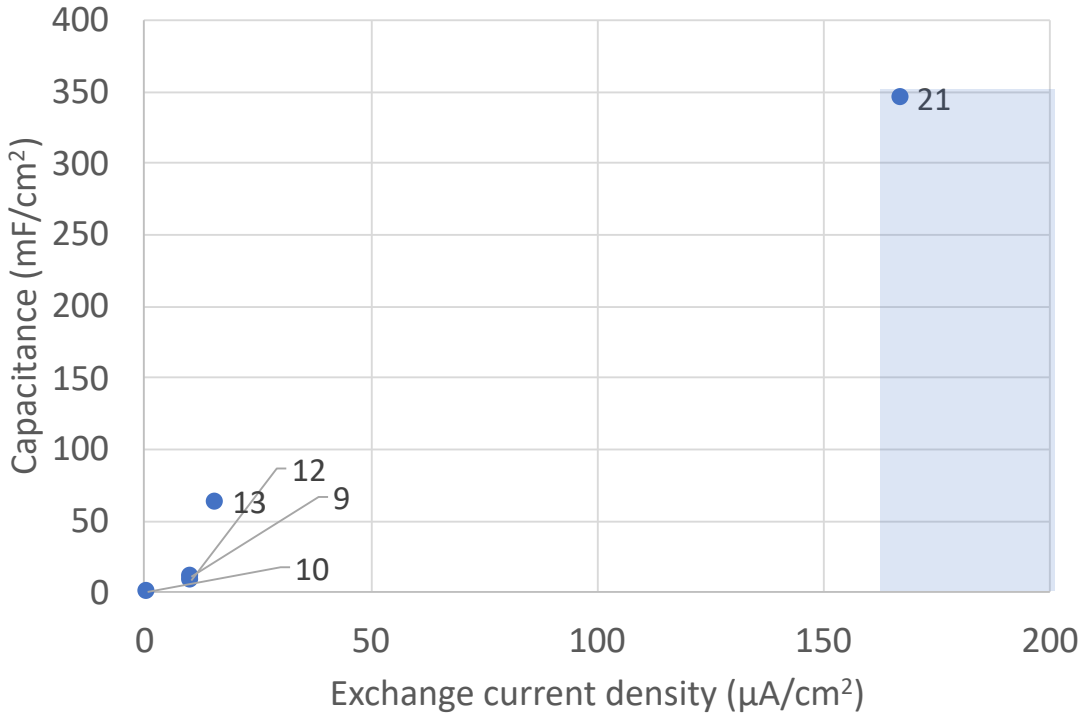

Figure 1.11. Capacitance and exchange current density of MoS_2 based HER catalysts. The shaded area denotes the promising HER catalyst because large capacitance and exchange current density are desired for HER catalyst. Within this shaded area, (i) the minimum of capacitance is the capacitance of most MoS_2 based catalysts; (ii) the maximum of capacitance is the capacitance of Li-MoS_2 on carbon fiber paper (Wang et al. 2013). The shaded area of exchange current density is the same as figure 1.10.

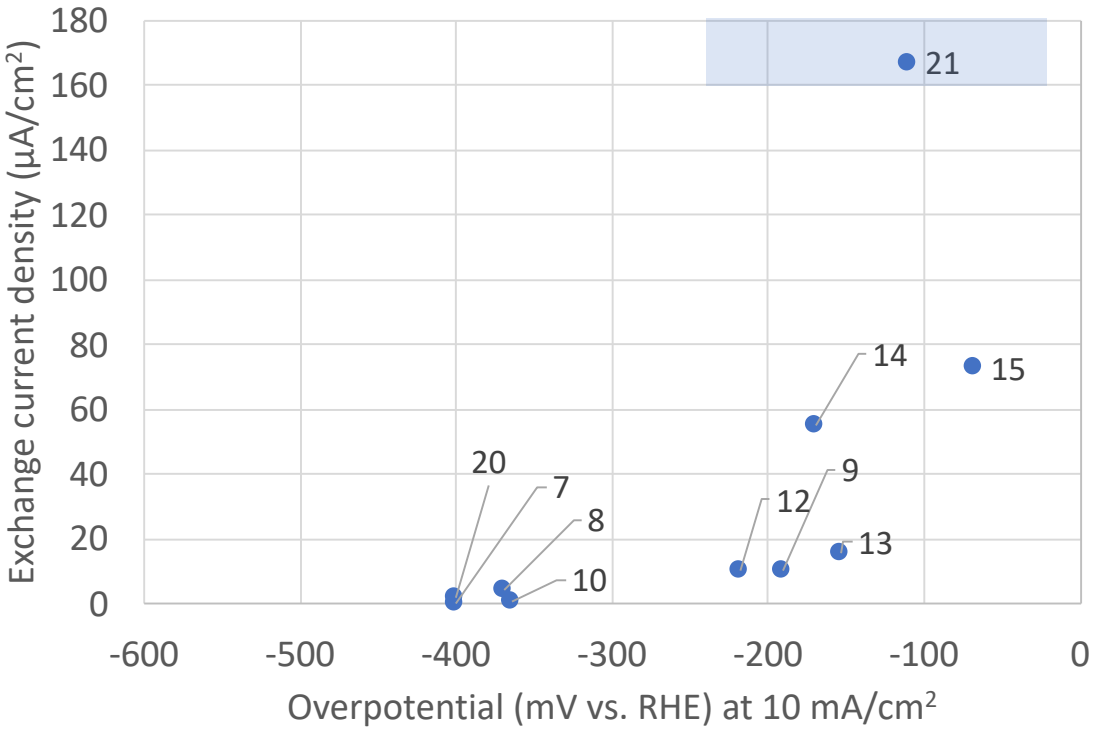

Figure 1.12. Exchange current density and overpotential of MoS_2 based HER catalysts. The shaded area denotes the promising HER catalyst because small overpotential and large exchange current density are desired for HER catalyst. The shaded area of overpotential and exchange current density are the same as figure 1.9 and 1.10, respectively.

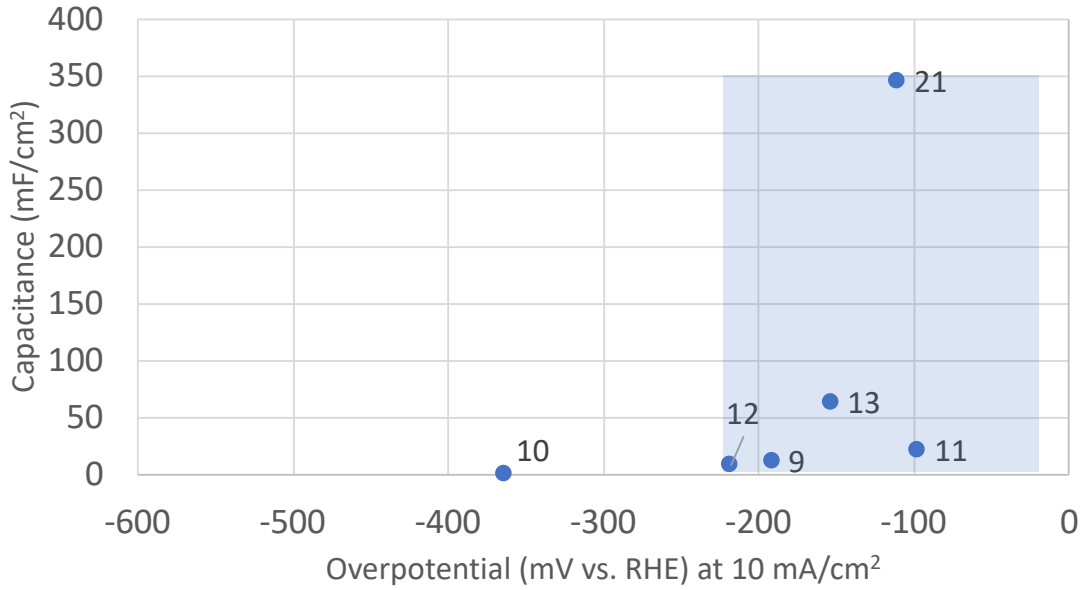

Figure 1.13. Capacitance and overpotential of MoS_2 based HER catalysts. The shaded area denotes the promising HER catalyst because small overpotential and large capacitance are desired for HER catalyst. The shaded area of overpotential and capacitance are the same as figure 1.9 and 1.11, respectively.

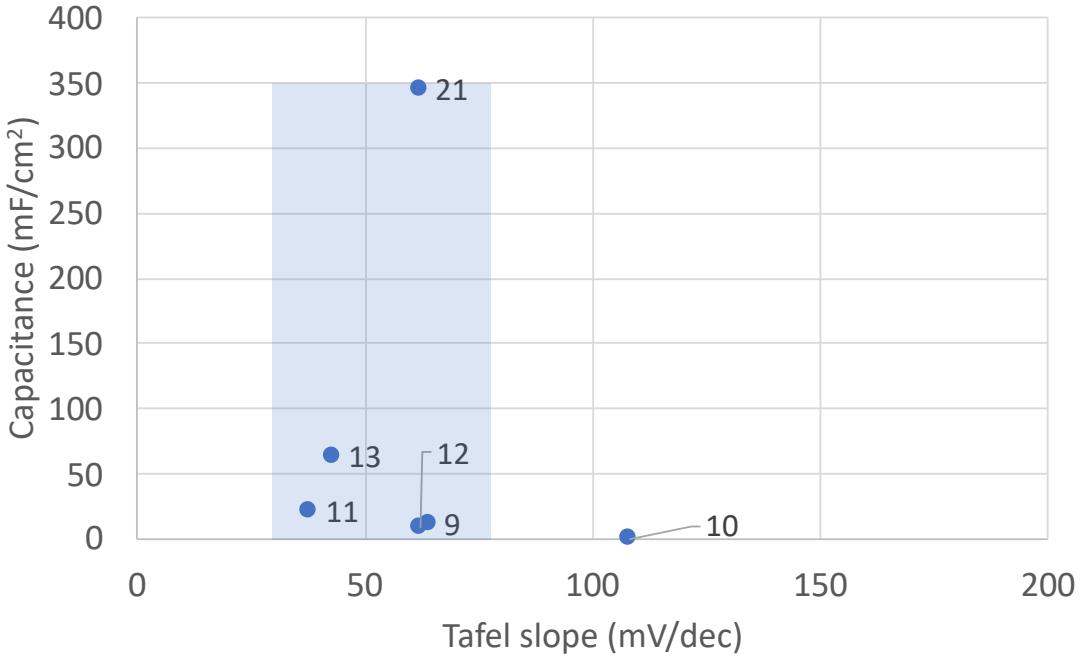

Figure 1.14. Capacitance and Tafel slope of MoS_2 based HER catalysts. The shaded area denotes the promising HER catalyst because small Tafel slope and large capacitance are desired for HER catalyst. The shaded area of Tafel slope and capacitance are the same as figure 1.9 and 1.11, respectively.

Figure 1.15 to figure 1.18 show chronological trends in catalytic performance of MoS_2 based HER catalysts.

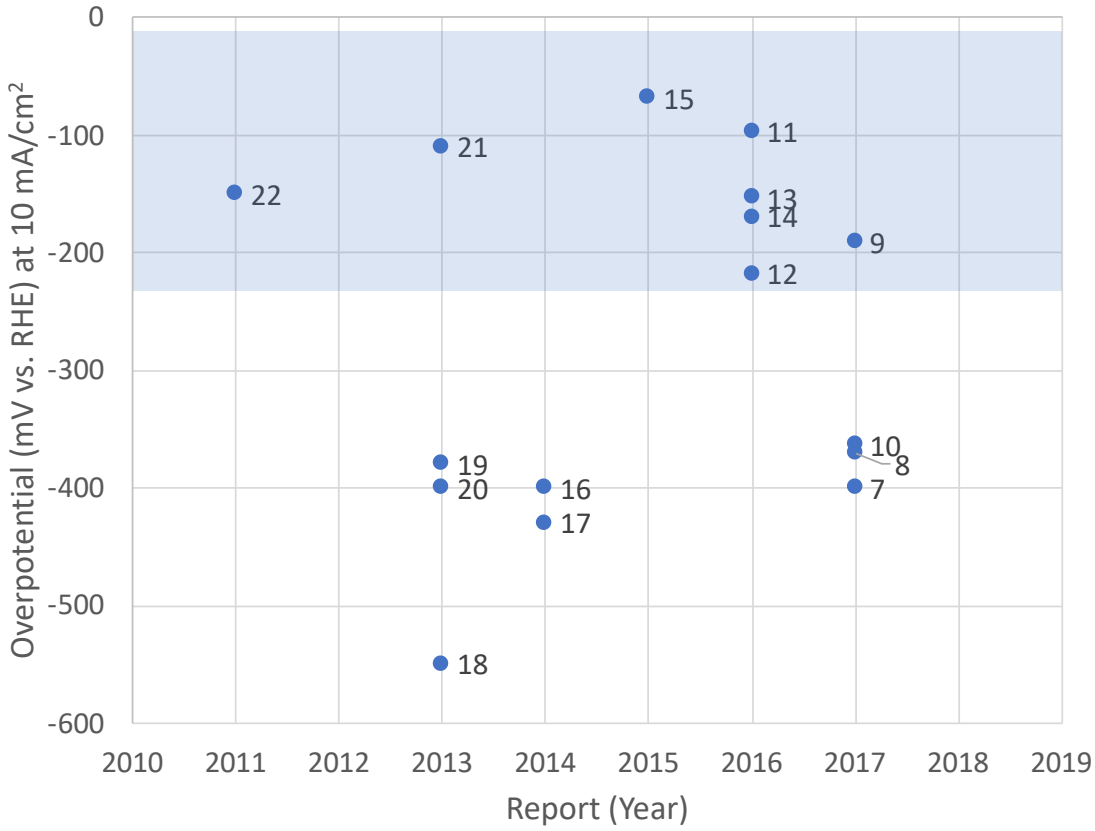

Figure 1.15. Chronological trends in overpotential of MoS_2 based HER catalysts. The shaded area denotes the promising HER catalyst because small overpotential (absolute value) is desired for HER catalyst. Within this shaded area, (i) the minimum of the overpotential is the overpotential at 10 mA/cm^2 of Pt wire (Chhetri et al., 2017); (ii) the maximum of the overpotential is the overpotential at 10 mA/cm^2 of most MoS_2 based catalysts.

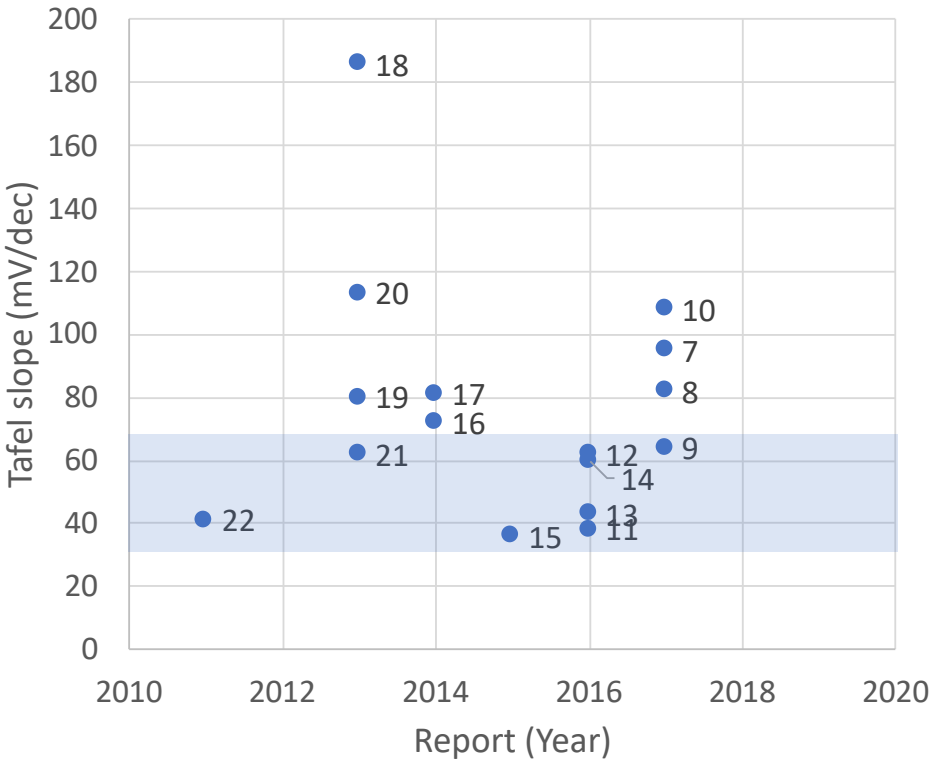

Figure 1.16. Chronological trends in Tafel slope of MoS_2 based HER catalysts. The shaded area denotes the promising HER catalyst because small Tafel slope is desired for HER catalyst. Within this shaded area, (i) the minimum of Tafel slope is the Tafel slope of Pt wire (Kong et al., 2014); (ii) the maximum of Tafel slope is the Tafel slope of most MoS_2 based catalysts.

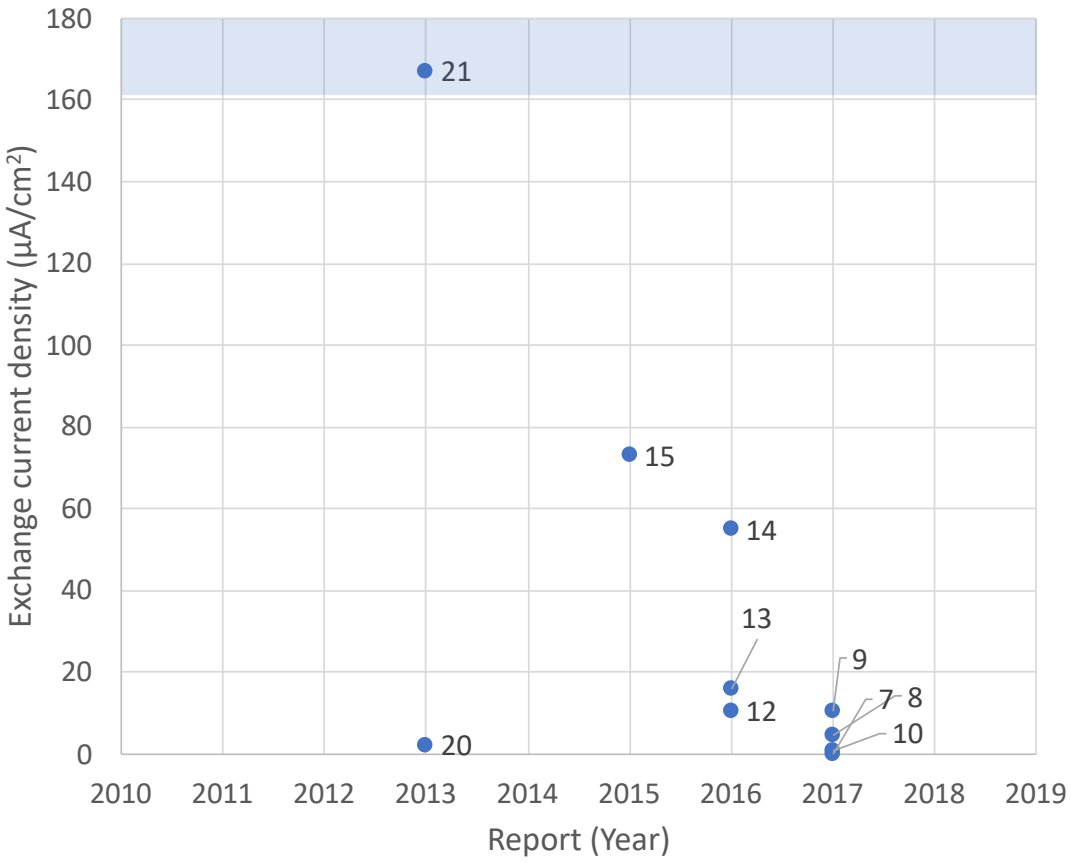

Figure 1.17. Chronological trends in exchange current density of MoS_2 based HER catalysts. The shaded area denotes the promising HER catalyst because large exchange current density is desired for HER catalyst. Within this shaded area, (i) the minimum of exchange current density is the exchange current density of Li-MoS_2 on carbon fiber paper (Wang et al. 2013); (ii) the maximum of exchange current density is the exchange current density of 10 wt% Pt/C (Hsu et al., 2012).

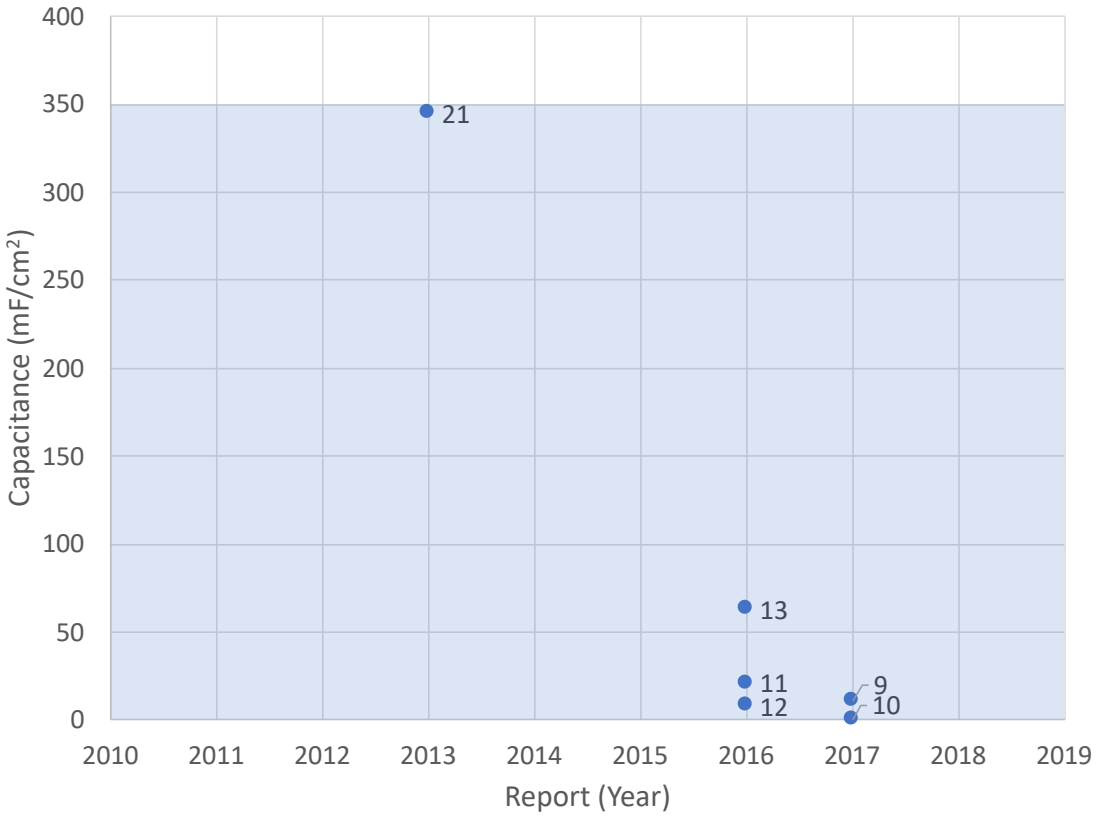

Figure 1.18. Chronological trends in capacitance of MoS_2 based HER catalysts. The shaded area denotes the promising HER catalyst because large capacitance is desired for HER catalyst. Within this shaded area, (i) the minimum of capacitance is the capacitance of most MoS_2 based catalysts; (ii) the maximum of capacitance is the capacitance of Li-MoS_2 on carbon fiber paper (Wang et al. 2013).

1.2 Challenges of c-MoS_2

c-MoS_2 can improve both the total electrode properties and intrinsic properties by using the merits of 3D nanostructures, and strained S-vacancies. However, the crumpled sheets are loosely packed together, thus affecting the overpotential, Tafel slope, current density and charge transfer resistance of the catalyst. Therefore, in the present work, mechanical force is used to make the crumpled sheets pack closer together, in an effort to improve electron transfer. The work builds on an initial observation by Y.-C. Chen (private communication from Dr. V. Tung) that scratching with tweezers can induce change in the packing morphology of c-MoS_2 deposited on Si. The term "Bulk Nanostructure Materials" (BNM) will be used in connection with the packing morphology, consistent with the definition that BNM are nanometer-sized features that have a considerable influence on the properties of the materials (Valiev et al., 2014).

1.3 Hypothesis

High surface area and mass loading associated with friction induced structural transformation of crumpled MoS_2 (FIST c-MoS_2) could improve catalytic performance of the electrode for HER compared to c-MoS_2 and ce-MoS_2 by lowering the overpotential and Tafel slope.

1.4 Preliminary work

1.4.1 Raman Spectra

Figure 1.19 shows the Raman spectra of FIST c-MoS_2 and c-MoS_2. The E_{2g} and A_{1g} vibration modes of FIST c-MoS_2 locate at 379 cm^{-1} and 406 cm^{-1}, respectively, while the E_{2g} and A_{1g} vibration modes of c-MoS_2 locate at 383 cm^{-1} and 406 cm^{-1}, respectively. For MoS_2, a shift of -1.7 cm^{-1} for the E_{2g} vibration mode corresponds to 1 % strain (Rice et al., 2013; Castellanos-Gomez et al., 2013). The 4 cm^{-1} shift of the E_{2g} vibration mode therefore indicates that the surface strain in FIST c-MoS_2 is 2.35% higher than in c-MoS_2.

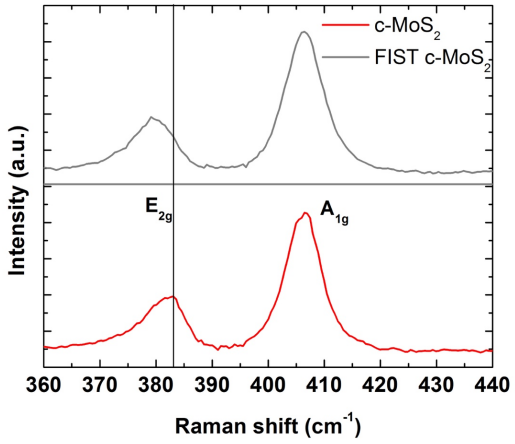

Figure 1.19. Raman spectra of FIST c-MoS_2 and c-MoS_2. Raman data provided by Dr. V. Tung.

1.4.2 Scanning electron microscopy (SEM) images

Figure 1.20 and 1.21 show the morphology of c-MoS_2 and FIST c-MoS_2.

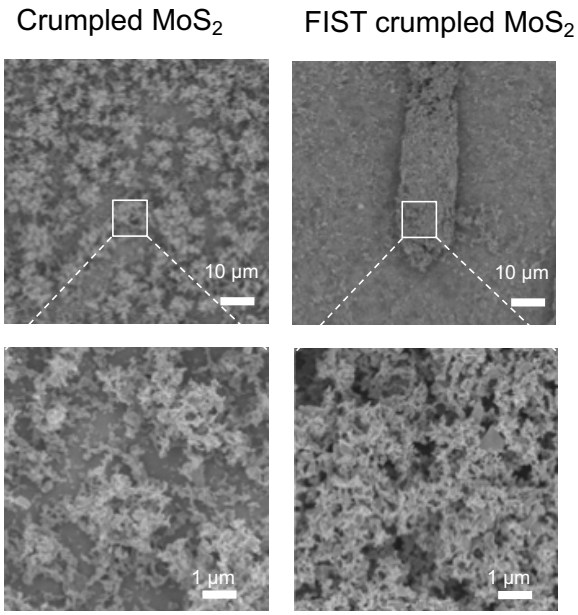

Figure 1.20. SEM images of c-MoS_2 and FIST c-MoS_2 on Si substrates.

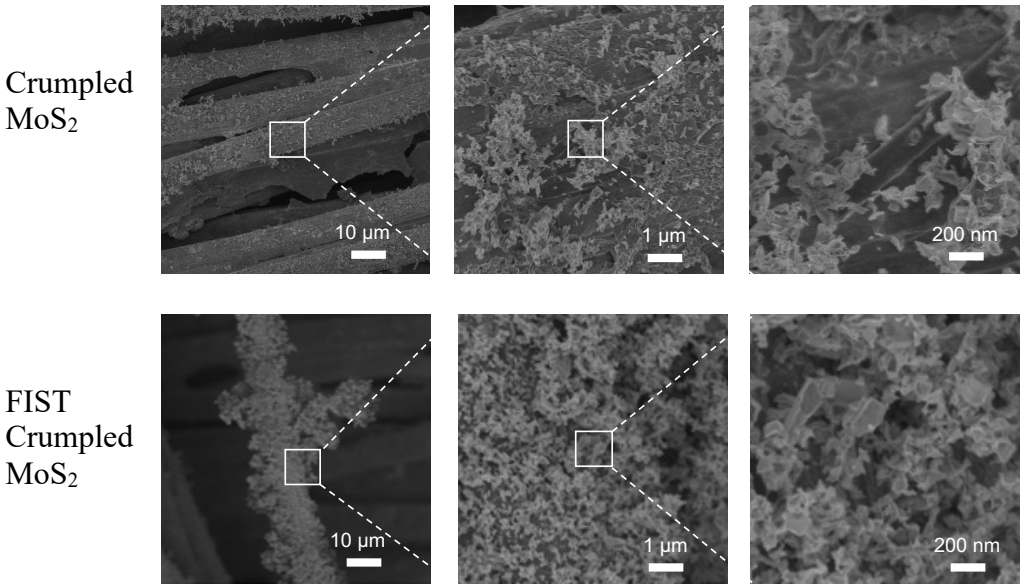

Figure 1.21. SEM images of c-MoS_2 and FIST c-MoS_2 on carbon cloth substrates.

Collectively, these preliminary results demonstrate two potential benefits of FIST c-MoS_2: (i) FIST c-MoS_2 does achieve a change in packing morphology at room temperature, and (ii) FIST c-MoS_2 achieves a higher % strain compared to c-MoS_2.

CHAPTER 2: Methods

2.1 Chemically exfoliated Molybdenum disulfide (ce-MoS_2) synthesis:

2.1.1 Lithiation

During lithiation, 1 g of MoS_2 (particle size < 2μm, Sigma Aldrich) is added into a 20 mL glass vial. In a nitrogen-filled glovebox, 15 mL of 1.6 M n-butyl lithium is added into the same glass vial. The solution is stirred with a magnetic stir bar at 700 rpm in the glove box for 96 h. After 96 h, the solution is filtered and washed with hexane (100 mL, 3 times) over 3 layers of Whatman filter paper (#41, 55 mm diameter) in the glovebox. MoS_2 cake and filter papers are transferred into a covered Petri dish and removed from the glovebox. In the fume hood, MoS_2 cake and the topmost filter paper are placed into a 500 mL glass bottle. The glass bottle is washed with detergent (VWR Labtone) dissolved in deionized water, rinsed three times with deionized water, and dried in an oven before use. In the glass bottle, 150 mL deionized (DI) water is added.

2.1.2 Exfoliation

During exfoliation, the solution is sonicated (VWR 97043-972) for 3 minutes. After 3 minutes, the filter paper inside the solution is removed. The solution is then sonicated for 90 minutes (Chou et al., 2015; Chen et al., 2017). After 90 minutes, the solution is filtered over a GNWP Millipore membrane filter (specifically, 0.2 μm pore size, nylon net filter, hydrophilic, 47 mm diameter). 100 mL DI water is added to the filter, 3 times. After the solution is filtered through, MoS_2 cake is collected before drying out, because drying would restack MoS_2 sheets. MoS_2 cake and the Millipore filter are placed into the same type of glass bottle as used for sonication. In the glass bottle, 200 mL DI water is added. The solution is sonicated for 3 minutes. After 3 min, the Millipore filter is removed. The solution is sonicated for 90 min.

2.1.3 Purification

The solution is allowed to sit overnight. The top 80 percent is collected.
The concentration of ce-MoS_2 is determined by comparing ultraviolet and visible light spectroscopy (UV-VIS) absorbance of the solution with a known concentration (i.e., reference) solution. The concentration of the reference solution is determined by inductively coupled plasma mass spectroscopy (ICP-MS).

2.2 Substrate preparation

2.2.1 ce-MoS_2 on carbon cloth substrate

The carbon cloth (Untreated carbon cloth, thickness 15 mils, Fuel Cell Earth) is used as purchased. The carbon cloth is cut into rectangular pieces, 1.3 cm by 1.0 cm. The carbon cloth is dipped into chemical exfoliated MoS_2 sheets dispersed in deionized water and isopropanol (v/v, 1:3) at a concentration of 175 μg/mL. The carbon cloth is dried at 25˚C. The dipping and drying processes are repeated a total of 5 times.

2.2.2 Stainless steel substrate

The stainless steel is cut into rectangular pieces, 2.0 cm by 1.0 cm. The stainless steel is blown with air from an air gun to remove the particles on the surface.

2.2.3 Si substrate

The Si is cut into square pieces, 1.5 cm by 1.5 cm. The Si is placed on a Teflon holder. The holder and Si are placed into a 1000 mL beaker containing acetone and sonicated for 5 minutes. The holder and Si are then removed from the beaker. The acetone is decanted to waste and is replaced by isopropanol. After sonication in the isopropanol for 5 minutes, the Si is removed and dried by blowing with air from an air gun.

2.2.4 Purpose of different substrates

The purpose of the different types of substrates is shown in the flow chart below. Carbon cloth is chosen as a substrate for electrochemical testing because it has high porosity (providing good electrolyte access to the supported catalyst) and good electrical conductivity, and nanostructures can be deposited directly on this substrate. The electrochemical testing is performed to compare the HER activity of the catalysts. Stainless steel also has good electrical conductivity and can also accept direct deposition of nanostructures; it provides an alternative platform for characterizing HER activity. Si is chosen as a substrate for x-ray diffraction (XRD) and Raman spectroscopy because the signal corresponding to the Si does not interfere with the MoS_2 signal (Ali et al., 2012; Joensen et al., 1987; Chen et al., 2017). XRD is performed to compare the layer stacking of the catalysts. Raman spectroscopy is performed to compare the percent strain of the catalysts.

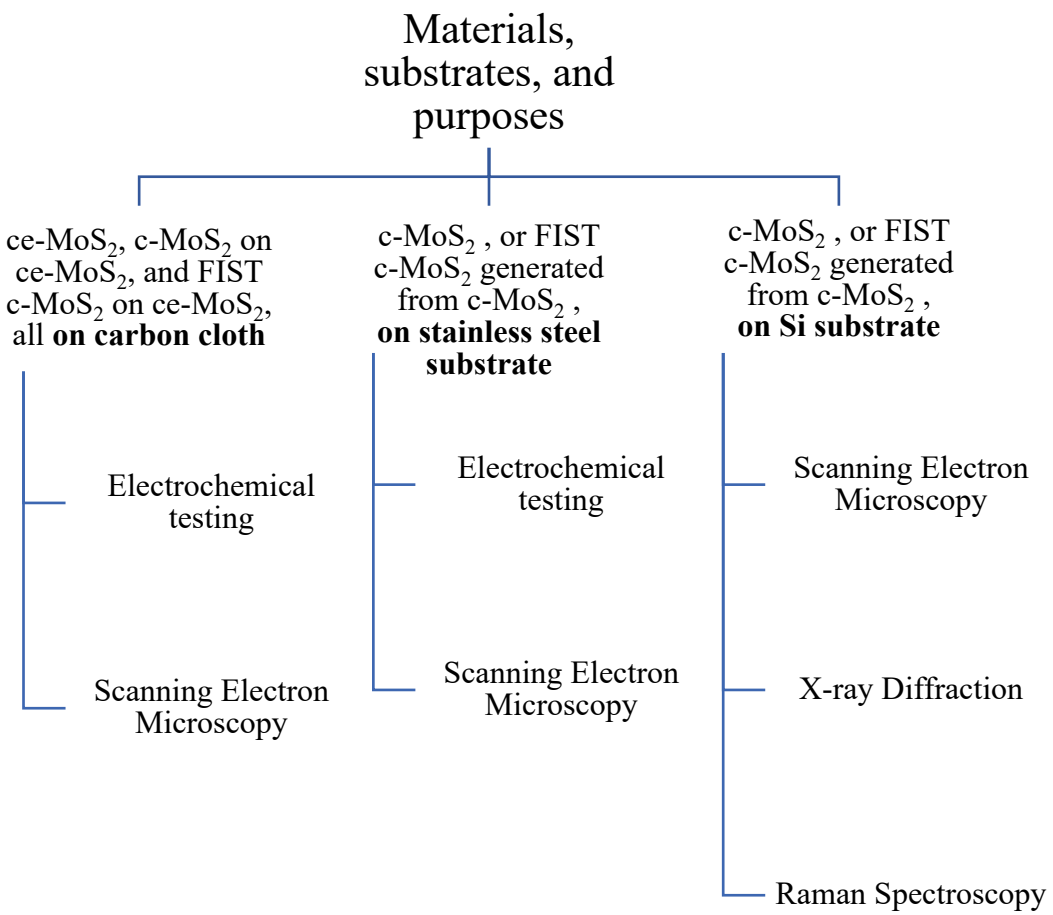

2.3 Crumpled Molybdenum disulfide (c-MoS_2) preparation

Electrospray setup comprises of a high-power supply (ES 40P-20 W/DAM, Gamma high voltage research), a syringe pump (Genie touch, Kent Scientific Corporation), a 5 mL syringe (Luer-lok tip, BD), a tube (SE-200, TYGON), two single barb insert fittings and a needle (gauge 23, thin wall needle, 1.5 inches length, 304 stainless steel, Lab express management co.). ce-MoS_2 dispersions in a mixture of DI water and isopropanol (v/v, 1:3) with a concentration of 175 µg/mL are fed to the needle by a syringe pump. Electric fields are generated through a high-power supply (Chen et al., 2017). An applied electric field of 1.35 kV/cm is applied to the needle. A flow rate of 5 µL/min is used for c-MoS_2 preparation. The c-MoS_2 are directly deposited onto ce-MoS_2 on carbon cloth or Si substrate (P type, B doped, <100>, #783, Universitywafer) or stainless steel substrate (Coil Shim Stock, 316, 0.002 inches, Maudlin products). Computerized multipass deposition is achieved through the integration of an x-y translational stage (LTS 200, Thorlabs) at a linear stage speed of 2.5 mm/s.

2.4 Friction induced structural transformation of c-MoS_2 (FIST c-MoS_2): A cylindrical steel mass is placed on c-MoS_2 on ce-MoS_2 on carbon cloth or c-MoS_2 on stainless steel or c-MoS_2 on Si substrate. ce-MoS_2 between the c-MoS_2 and the carbon cloth serve as a more uniform foundation between carbon cloth fibers. The substrate is moved forward relative to the mass, while tweezers are used to prevent the mass itself from moving. Figure 2.1 shows the friction induced structural transformation (FIST) process and morphology of c-MoS_2 and FIST c-MoS_2 on Si substrates.

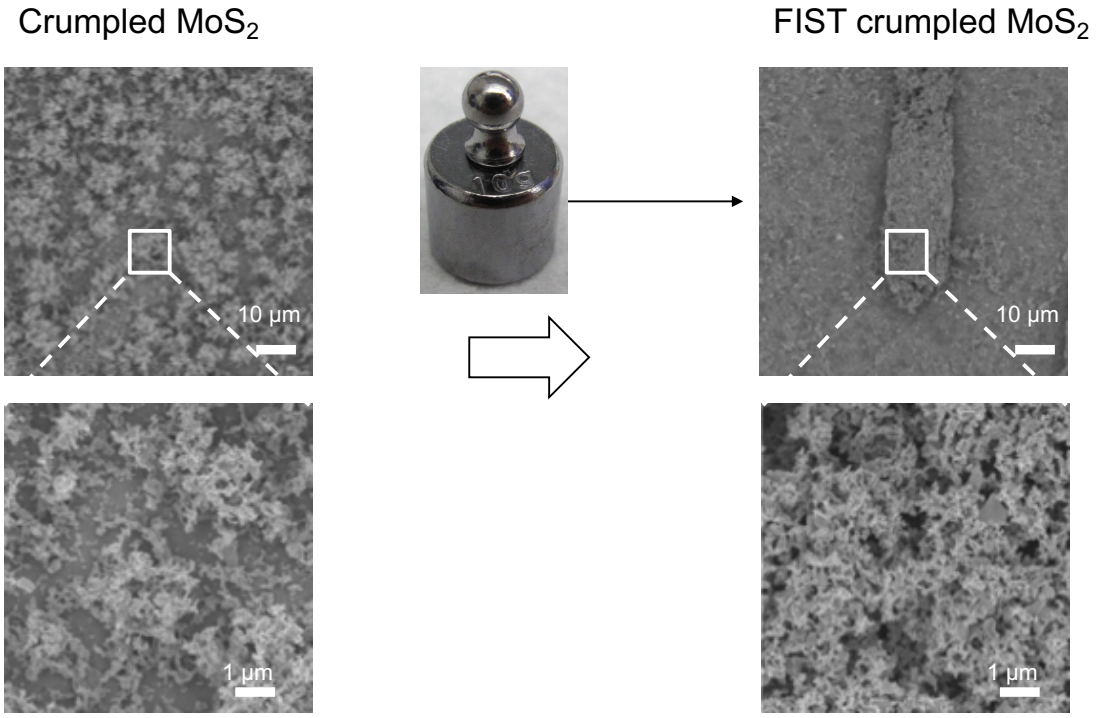

Figure 2.1. Schematic illustration of friction induced structural transformation (FIST) process. Morphology of crumpled MoS_2 and FIST crumpled MoS_2 on Si substrates are observed.

ce-MoS_2, c-MoS_2 on ce-MoS_2, and FIST c-MoS_2 on ce-MoS_2, all on carbon cloth are used for testing catalytic performance.

2.5 Vertical force from a cylindrical steel mass

For FIST process, the cylindrical steel mass is placed on top of c-MoS_2 on the substrate. The vertical force, F, and the pressure, P, can be calculated from the mass (m=0.005 kg) and radius (r=0.0045 m), using

$$F = mg$$

and

$$P = \frac{F}{\pi r^2}$$

where g is the acceleration due to gravity (9.81 m/s^2). F and P are calculated to be 0.0491 N and 772 Pa, respectively.

2.6 Electrohydrodynamic (EHD) spraying

EHD spraying is a method of liquid atomization by using electrostatic and capillary forces (Jaworek et al., 2008). ce-MoS_2 colloidal solution was used as a precursor to prepare c-MoS_2 by solvent droplet template method through the EHD spraying. The electrical force makes the ce-MoS_2 colloidal solution disperse into fine droplets. At the Rayleigh point, where the evaporated droplet surface tension can no longer sustain the charge, fission of the droplet that contains ce-MoS_2 occurs. This process helps reduction of the number of ce-MoS_2 contained in each droplet. The Rayleigh limit can be described (Jaworek 2007) by

$$Q_R = 2\pi(16\sigma_l \varepsilon_0 r^3)^{1/2}$$

where Q_R is the Rayleigh limit (magnitude of charge on a droplet), σ_l is the liquid surface tension, ε_0 is the electric permittivity of free space, and r is the droplet radius.

With constant liquid surface tension and electric permittivity of the free space, the magnitude of charge on a droplet is an increasing function of the droplet radius. While the solvent of each droplet that acts as a nanoreactor evaporates, mono-to-few layered ce-MoS_2 will minimize the contact area with solvent and maximize the overall contact area of ce-MoS_2, due to strong intermolecular forces on its basal plane. Figure 2.2 shows a schematic of the EHD spraying equipment.

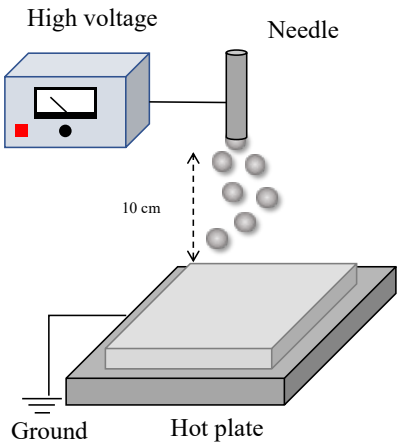

Figure 2.2. Electrohydrodynamic (EHD) spraying equipment.

Ishihara et al. used EHD spraying method to prepare crumpled graphene nanostructures which helps improve the electron transport in TiO_2 photoanode (Ishihara et al., 2016).

2.7 Scanning electron microscopy (SEM); X-ray Energy-dispersive spectroscopy (EDS)

The primary electrons from the electron gun are accelerated onto a material, where they interact with the atoms in the sample. Elastic collision occurs when the primary electrons are attracted to the atom nuclei in the sample, resulting in a change in the direction of the primary electrons without significant change in their energy. The electrons that deflect out of the sample are called backscattered electrons. Inelastic collision occurs when the primary electrons interact with the electrons in the sample, resulting in a transfer of energy from the former to the latter. The atoms then expel electrons which are called secondary electrons. If the electron vacancy formed during the expulsion process is filled by an electron from a higher-level orbital, an x-ray characteristic is produced. SEM images are made by recording the secondary and/or backscattered electrons from different areas on a sample (Temenoff et al., 2009). Backscattered electrons have higher maximum escape depths compared to secondary electrons, because of their higher energy. Using an energy-sensitive x-ray detector, a map of corresponding x-rays from chosen elements can be generated (Lindsay 2010).

The spatial resolution is defined as the minimum distance that can be distinguished by an optical apparatus. Parameters that affect the resolution in SEM are accelerating voltage, aperture size, working distance (WD) and astigmatism.

Accelerating voltage affects charge on a sample, beam penetration, probe current and lens aberrations. High accelerating voltage will increase charge on a sample and beam penetration, which could damage the sample and reduce surface detail of the sample. High accelerating voltage will increase probe current. In order to obtain an image with optimal contrast, a minimum probe current and high signal to noise ratio are required. High accelerating voltage will decrease lens aberrations that distort the shape of the electron beam (Hafner, B., 2007).

Aperture size affects the convergence angle of the beam, which will affect the depth of field, F. Depth of field is the distance along the microscope axis where the sample can be moved without blurring the image (Bowen et al., 1975). Figure 2.3 shows the depth of field, where d is the resolution required, and α is the semi-angular aperture.

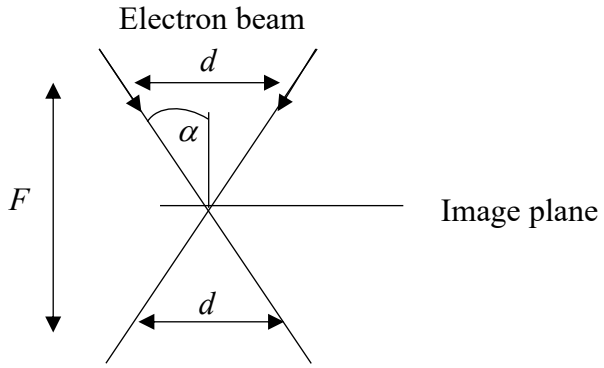

Figure 2.3. The depth of field, *F* for a given resolution, *d* depends inversely on the semi-angular aperture, α as shown in the image (Bowen et al., 1975).

A small aperture will provide higher depth of field and reduce lens aberrations. A very small aperture will display diffraction effects and reduce beam current (Hafner 2007).

Working distance (WD) is the distance between the objective lens and the sample. WD is used for adjusting coarse focus of the sample. The objective lens is used to adjust convergence of the electron beam and focus the electron beam on the sample surface. The convergence of the electron beam is changed by changing the current in the objective lens (Hafner 2007).

Astigmatism occurs when the fields produced by the lenses are not perfectly symmetric, which results in a converged beam that has an oblong cross-section. Astigmatism can be compensated by applying current to a ring of stigmator coils around the objective lens. The converged beam will then be more symmetric (Hafner 2007).

The resolution limit of SEM precludes the use of this technique to measure sample (nanosheet) thickness near or below 1 nm. Atomic force microscopy (AFM) is better suited for that purpose.

2.8 Atomic force microscopy (AFM)

AFM can be used to visualize surface topography of materials. AFM is operated based on the interaction between a probe and the atomic constituents of the sample surface. Van der Waals and electrostatic interactions between atoms in the probe and those on the material surface create a characteristic potential energy profile (Temenoff et al., 2009). The potential energy profile is also known as a Lennard-Jones plot, having been proposed by John Lennard-Jones in 1931 (Lennard-Jones 1931). Figure 2.4 schematically shows the force profile, where x-axis is the tip-sample distance (not interatomic separation). The force, F is defined (Lindsay 2010) as:

$$F(D) = -\frac{\mathrm{d}W(D)}{\mathrm{d}D}$$

where D is the tip-sample distance and W is the potential energy.

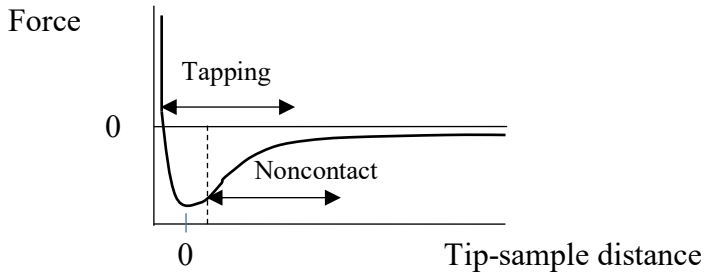

Figure 2.4. The schematic force profile of a spherical probe above a plane (Lindsay 2010). Contact occurs when tip-sample distance is zero.

For contact mode, the probe is brought down to the surface until the desired contact force is measured (Lindsay 2010). The probe is moved across the sample surface. The reflection of a laser off the probe is monitored to measure the probe deflection (Temenoff et al., 2009).

For dynamic force microscopy mode, the probe is vibrated close to its resonance frequency above the surface. The electronics are set up to monitor the amplitude of the oscillating deflection signal. The amplitude of the oscillating is maintained constant by adjustment of the probe height. The dynamic force microscopy mode can be operated in a regime in which the free amplitude is reduced as the probe hits the surface on its downward swing which is called intermittent contact "tapping" mode. Tapping mode is suitable for "soft" samples (Lindsay 2010).

The dynamic force microscopy mode can also be operated in a noncontact mode. Since the spatial resolution is depended on the interactions between atoms in the probe and those on the material surface, the noncontact mode results in lower resolution. Noncontact mode is suitable for "extremely soft" samples (Lindsay 2010).

2.9 Linear Sweep Voltammetry (LSV)

Linear Sweep Voltammetry (LSV) is a technique in which a voltage is applied to electrochemical cells and the current response is measured. Figure 2.5 shows a schematic LSV plot of the hydrogen evolution reaction (HER).

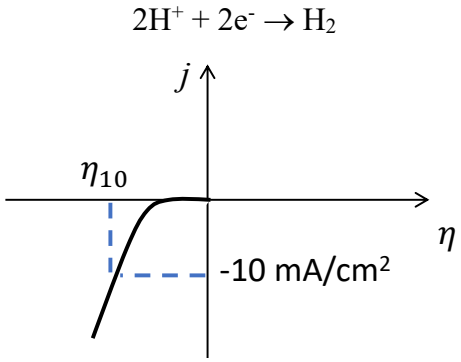

Figure 2.5. LSV plot of hydrogen evolution reaction (HER). x axis is the overpotential, η. y axis is the current density, j.

LSV provides information on the overpotential, Tafel slope, and exchange current density.

Overpotential, η is the voltage that is sacrificed to overcome the activation energy associated with the electrochemical reaction (O'Hayre et al., 2009). In other words, the overpotential is the potential difference between the thermodynamically determined potential and the experimental potential (Ding et al., 2016). The overpotential at 10 mA/cm^2, η_{10} is reported for comparing the HER catalytic ability because it is the current density, j (units of mA/cm^2) expected for 12.3% efficient solar to hydrogen

device. 12.3% is the efficiency that would be required for cost competitive photoelectrochemical water splitting (Benck et al., 2014). In order to make hydrogen from water, catalysts are required to minimize the overpotential.

Tafel slope provides information on the additional voltage required to increase the catalytic current at the cathode by one order of magnitude (Benck et al., 2014; Chhowalla et al., 2013). A small Tafel slope indicates that the current density can increase rapidly with overpotential change (Suen et al., 2017). The Tafel slope can be obtained from the Tafel equation, which in turn can be obtained from the Butler-Volmer equation (Suen et al., 2017):

$$j = j_0 \left[\exp\left(\frac{\alpha_a n\mathrm{F}\eta}{RT}\right) + \exp\left(\frac{\alpha_c n\mathrm{F}\eta}{RT}\right)\right]$$

where j_0 is the exchange current density, α_a and α_c are the transfer coefficient at the anodic and cathodic half reactions, n is the number of transferred electrons in the reaction, F is Faraday's constant, η is the overpotential, R is the ideal gas constant and T is the absolute temperature.

For high cathodic overpotential conditions (HER), the overall current comes from the cathodic current while the anodic current is negligible. The Butler-Volmer equation can then be simplified to the following equation, which is known as the Tafel equation (Suen et al., 2017; O'Hayre et al., 2009),

$$j = j_0 \exp\left(\frac{\alpha_c n\mathrm{F}\eta}{RT}\right)$$

The Tafel equation can be translated into a logarithmic form:

$$\ln\frac{j}{j_0} = \ln\exp\left(\frac{\alpha_c n\mathrm{F}\eta}{RT}\right)$$

$$\ln\frac{j}{j_0} = \frac{\alpha_c n\mathrm{F}\eta}{RT}$$

$$\eta = \frac{RT}{\alpha_c n\mathrm{F}}\ln\frac{j}{j_0}$$

The relationship between ln vs. log is

$$\ln x = \log_e x = (\log_{10} x) / (\log_{10} e) = 2.303 \log_{10} x$$

so,

$$\eta = \frac{2.303RT}{\alpha_c n\mathrm{F}}\log\frac{j}{j_0}$$

$$\eta = \frac{2.303RT}{\alpha_c n\mathrm{F}} \log j - \frac{2.303RT}{\alpha_c n\mathrm{F}} \log j_0$$

The Tafel slope is defined as

$$b = \frac{2.303RT}{\alpha_c n\mathrm{F}}$$

The Tafel slope can be determined from the slope of a linear fit on the Tafel plot, where the x axis is the log scale of the absolute value of current density, and the y axis is the absolute value of the overpotential. Figure 2.6 shows Tafel plot.

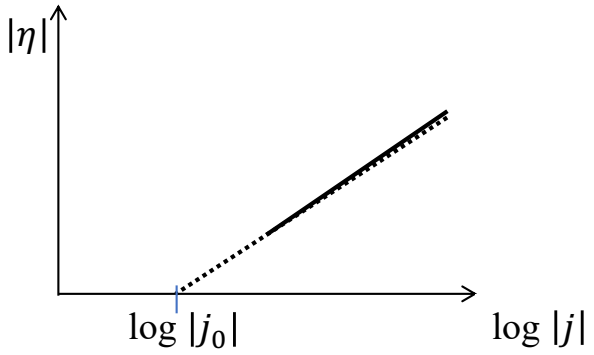

Figure 2.6. Tafel plot.

The Tafel slope can be used to identify the reaction mechanism and identify when the overpotential at 10 mA/cm^2 is the same for two samples (Benck et al., 2014; Conway et al., 2002).

If the Tafel slope is around 120 mV per decade (Li et al., 2011), the limiting step is an adsorption step (Volmer reaction)

$H_3O^+ + e^- \rightarrow H_{ads} + H_2O$

If the Tafel slope is around 40 mV per decade, the limiting step is an electrochemical desorption step (Heyrovsky reaction)

$H_3O^+ + H_{ads} + e^- \rightarrow H_2 + H_2O$

If the Tafel slope is around 30 mV per decade, the limiting step is a desorption step (Tafel reaction)

$H_{ads} + H_{ads} \rightarrow H_2$

where H_{ads} denotes the hydrogen atoms adsorbed at the electrode surface.

The exchange current density is the current in the absence of net electrolysis and at zero overpotential. Exchange current density provides information on the intrinsic catalytic activity of the electrode material under equilibrium condition (Ding et al., 2016). The exchange current density can be determined from the intercept ($\eta = 0$) on the Tafel plot.

It is worth noting that, although the Tafel equation is derived from the Butler-Volmer equation under a particular set of limiting conditions, it predates the Butler-Volmer equation in the history of electrochemistry.

2.10 Cyclic Voltammetry (CV)

Cyclic Voltammetry (CV) is a technique in which a voltage is applied to electrochemical cells and swept linearly with time across a voltage window of interest. The current response is plotted as a function of voltage (O'Hayre et al., 2009). Figure 2.7 shows a schematic CV plot.

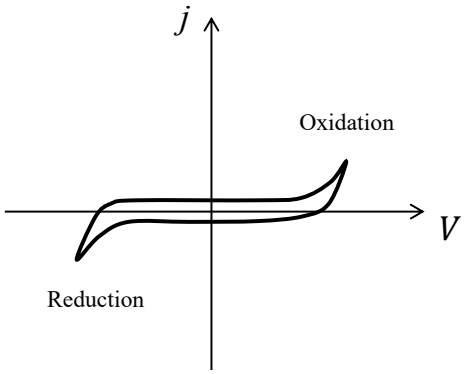

Figure 2.7. CV plot with IUPAC convention where the low potentials are on the left.

For aqueous electrolytes, the reduction reaction is the hydrogen evolution reaction (HER) and the oxidation reaction is the oxygen evolution reaction (OER). For HER, the voltage window of interest is in the reduction reaction region.

CV plots can be used to evaluate the electrochemical stability of the catalyst. Instability can be recognized if the plots after numerous (e.g. 1000) cycles change as shown in figure 2.8. Instability is then confirmed by performing LSV before and after the CV cycling, to report the overpotential at 10 mA/cm^2, Tafel slope, and exchange current density (Chen et al., 2011).

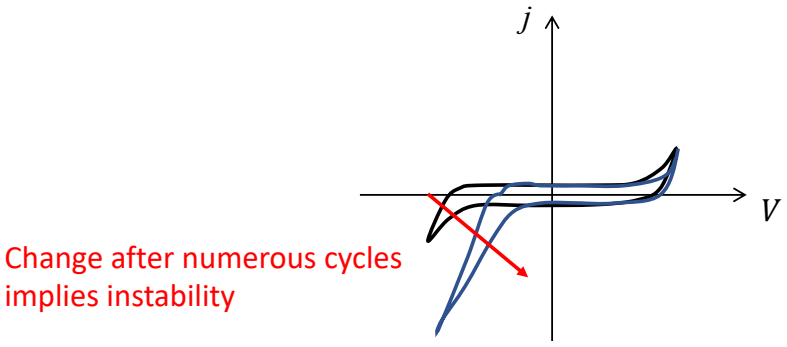

Figure 2.8. A schematic CV plot that implies instability.

A decrease in the overpotential at 10 mA/cm^2 of MoS_2 catalyst after cyclic voltammetry at negative potential (vs. reversible hydrogen electrode, RHE) in acidic electrolyte has been reported (Li et al., 2017). Li et al. reported that cycling results in proton intercalation (p-doped) for MoS_2 on the glassy carbon substrate. Glassy carbon has been used in rotating disk electrode to prevent hydrogen bubbles accumulate at the electrode surface and block HER active area (Benck et al., 2014). The evidence for proton intercalation in MoS_2 is (i) the displacement of the photoluminescence (PL) to shorter wavelength (blueshift), and (ii) the displacement of x-ray photoelectron spectroscopy (XPS) signal to lower binding energy after cyclic voltammetry at negative potential (vs. RHE) in acidic electrolyte (Li et al., 2017; Nipane et al., 2016).

2.11 Electrochemical Impedance Spectroscopy (EIS)

Electrochemical impedance spectroscopy (EIS) is a technique in which a voltage perturbation is applied to electrochemical cells. The resulting current response amplitude and phase shift are measured. Impedance, Z is a measure of the ability of a system to prevent the flow of electrical current. Impedance is the ratio between a time-dependent voltage and a time-dependent current (O'Hayre et al., 2009).

$$Z = \frac{V(t)}{I(t)}$$

For sinusoidal input voltage, the voltage as a function of time will be

$$V(t) = V_0 \sin(\omega t)$$

where $V(t)$ is the voltage at time t, V_0 is the amplitude of the voltage, ω is the angular frequency and t is time.

The relationship between angular frequency ω and frequency f is

$$\omega = 2\pi f$$

For a capacitor, the current leads the voltage by $\frac{\pi}{2}$.

For mathematical explanation, current and voltage as a function of time can be derived from

$$Q = CV$$

where Q is the charge on the capacitor's plates, C is the capacitance and V is the voltage across the capacitor. From Faraday's law,

$$I(t) = \frac{\mathrm{d}Q(t)}{\mathrm{d}t}$$

where $I(t)$ is the current at time t and $Q(t)$ is the charge at time t.

$$I(t) = \frac{\mathrm{d}Q(t)}{\mathrm{d}t} = C\frac{\mathrm{d}V(t)}{\mathrm{d}t}$$

$$= C\frac{\mathrm{d}(V_0 \sin(\omega t)}{\mathrm{d}t}$$

$$= \omega V_0 C \cos(\omega t) = \omega V_0 C \sin(\omega t + \frac{\pi}{2})$$

Therefore, Z for the capacitor can be written as

$$Z = \frac{V_0 \sin(\omega t)}{\omega V_0 C \cos(\omega t)} = \frac{\sin(\omega t)}{\omega C \sin(\omega t + \frac{\pi}{2})}$$

Since, in general, the current leads the voltage by a phase angle φ ($\frac{\pi}{2}$ in the case of a capacitor), the derivation of the above equation can be generalized to:

$$Z = \frac{V(t)}{I(t)} = \frac{V_0 \sin(\omega t)}{\mathrm{I}_0 \sin(\omega t + \varphi)} = Z_0 \frac{\sin(\omega t)}{\sin(\omega t + \varphi)}$$

Figure 2.9 displays a sinusoidal input voltage and a current response.

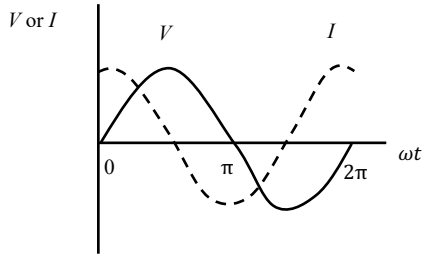

Figure 2.9. A sinusoidal input voltage and the current response.

To simplify algebra, it is convenient to use complex number notation to write the sinusoidal voltage, resultant current, and impedance of a system (Bard et al., 1980; O'Hayre et al., 2009):

$$V(t) = V_0 \exp(\mathrm{j}\omega t)$$

$$I(t) = I_0 \exp \mathrm{j}(\omega t - \varphi)$$

$$Z = \frac{V(t)}{I(t)} = \frac{V_0 \exp(\mathrm{j}\omega t)}{I_0 \exp \mathrm{j}(\omega t - \varphi)} = Z_0 \exp(\mathrm{j}\varphi) = Z_0 \cos\varphi + \mathrm{j}\, Z_0 \sin\varphi$$

where I_0 is the amplitude of the current, Z_0 is the impedance magnitude, and $\mathrm{j} = \sqrt{-1}$.

Figure 2.10 shows a vector of the impedance with angle φ on imaginary and real axes.

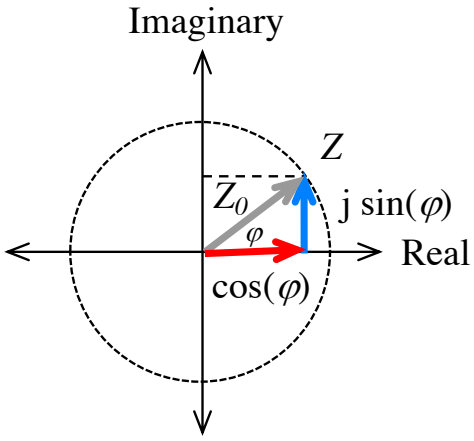

Figure 2.10. A vector of impedance on real and imaginary axes.

A Nyquist plot displays impedance data in terms of the real and imaginary components at different frequencies (O'Hayre et al., 2009). Nyquist plots are named after Harry Nyquist, acknowledging his contribution to defining stable conditions in negative feedback systems (Abbott et al., 1996; Nyquist 1932). The limitation of Nyquist plots is the absence of information on the corresponding frequency of each point on the plot. Figure 2.11 shows a schematic example of a Nyquist plot.

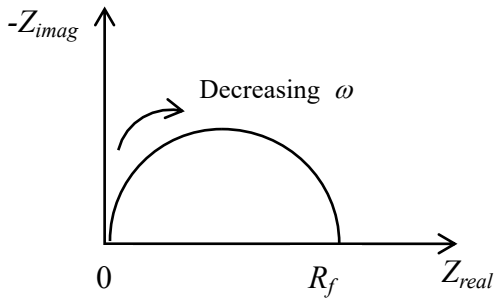

Figure 2.11. Schematic Nyquist plot. The high-frequency intercept is zero, while the low-frequency intercept is the Faradaic resistance, R_f. The latter describes the kinetics of the electrochemical reaction. A small R_f indicates fast reaction kinetics while a large R_f indicates slow reaction kinetics (O'Hayre et al., 2009).

A Bode phase plot shows impedance data in terms of phase (in degrees) at different frequencies. Bode phase plots were conceived by Hendrik Wade Bode in the 1930s. Figure 2.12 shows a schematic example of a Bode phase plot.

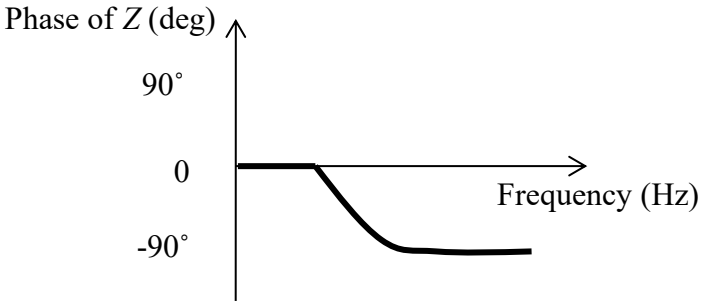

Figure 2.12. Schematic Bode phase plot. The phase of Z is plotted vs. log frequency.

The processes that occur during electrochemistry can be modeled using circuit elements. The circuit elements that represent the processes are called equivalent circuit models. The equivalent circuit of ohmic conduction is a resistor. For a resistor, φ is zero (O'Hayre et al., 2009). Z_Ω is ohmic impedance. R_Ω is ohmic resistance.

$$Z_\Omega = R_\Omega$$

The equivalent circuit of electrochemical reaction interface can be modeled as a parallel combination of a resistor and a capacitor (R_f and C_{dl}). R_f is the Faradaic resistance which describes the kinetics of the electrochemical reaction. C_{dl} is the double-layer capacitance which reflects the charge separation between electrons and ions at the interface (O'Hayre et al., 2009).

Impedance caused by a diffusion process is called a Warburg impedance. The impedance depends on the frequency of voltage perturbation. The relationship between infinite Warburg impedance, Z_w (i.e., the Warburg impedance for an infinitely thick diffusion layer) and Warburg coefficient for species i, σ_i is (O'Hayre et al., 2009):

$$Z_w = \frac{\sigma_i}{\sqrt{\omega}}(1\text{-j})$$

σ_i is defined (O'Hayre et al., 2009) as

$$\sigma_i = \frac{RT}{(n_i F)^2 A\sqrt{2}}\left(\frac{1}{c_i^0\sqrt{D_i}}\right)$$

where R is the ideal gas constant, T is absolute temperature, n_i is the number of electrons transferred in the reaction of species i, F is Faraday's constant, A is the electrode surface area, c_i^0 is the bulk concentration of species i, and D_i is the diffusion coefficient of species i. σ_i provides information on the effectiveness of transporting species i to or away from a reaction surface. If c_i^0 is small and D_i is low, then σ_i will be large and Z_w will be significant. On a Nyquist plot, the infinite Warburg impedance increases linearly with decreasing angular frequency. The infinite Warburg impedance is valid when the diffusion layer is infinitely thick. However, the diffusion layer is limited to the thickness of the catalyst. In this case, the impedance at lower frequencies does not obey the infinite Warburg impedance equation. The relationship between finite Warburg impedance, Z_o, diffusion layer thickness, δ and Warburg coefficient for species i, σ_i is (O'Hayre et al., 2009):

$$Zo = \frac{\sigma_i}{\sqrt{\omega}}(1\text{-j}) \tanh\left(\delta\sqrt{\frac{j\omega}{D_i}}\right)$$

At high angular frequencies or infinitely thick diffusion layer, $\tanh\left(\delta\sqrt{\frac{j\omega}{D_i}}\right)$ will be around 1. Z_o will be Z_w. At low angular frequencies or small diffusion layer thickness, the finite Warburg impedance moves back toward the real axis (O'Hayre et al., 2009).

2.11.1 Capacitance calculation

The impedance response of a capacitor is purely imaginary. The relationship between voltage and current for a capacitor is:

$$I(t) = \frac{\mathrm{d}Q(t)}{\mathrm{d}t} = C\frac{\mathrm{d}V(t)}{\mathrm{d}t}$$

where $I(t)$ is the current at time t, $Q(t)$ is the charge at time t, C is the capacitance and $V(t)$ is the voltage at time t.

For sinusoidal input voltage described in complex number notation,

$$I(t) = C\frac{\mathrm{d}(V_0 \exp(\mathrm{j}\omega t))}{\mathrm{d}t} = C(\mathrm{j}\omega)\, V_0 \exp(\mathrm{j}\omega t)$$

which gives an impedance of

$$Z = \frac{V(t)}{I(t)} = \frac{V_0 \exp(\mathrm{j}\omega t)}{C(\mathrm{j}\omega)\, V_0 \exp(\mathrm{j}\omega t)} = \frac{1}{\mathrm{j}\omega C}$$

Z_{im} is the imaginary component of impedance at the frequency, f.

$$Z_{im} = \mathrm{Im}\left(\frac{1}{\mathrm{j}\omega C}\right) = \mathrm{Im}\left(\frac{\mathrm{j}}{\mathrm{j}}\frac{1}{\mathrm{j}\omega C}\right) = \mathrm{Im}\left(-\frac{\mathrm{j}}{\omega C}\right) = \mathrm{Im}\left(0 - \frac{\mathrm{j}}{\omega C}\right) = -\frac{1}{\omega C} = -\frac{1}{2\pi f C}$$

The capacitance of samples in this work was therefore calculated from:

$$C = -\frac{1}{2\pi f Z_{im}}$$

where C is the capacitance, f is the frequency that gave the maximum value of phase of Z on the corresponding Bode phase plot, and Z_{im} is the imaginary component of impedance at the frequency, f on the corresponding Nyquist data (collected simultaneously with the Bode phase data).

2.12 Raman spectroscopy

C.V. Raman's group discovered the Raman effect in 1928 (Bohning et al., 1998). Raman light scattering happens when the scattered light has a different wavelength than the incident light. The energy of incident light is not conserved after vs. before the collision, which is called inelastic collision. Rayleigh scattered light happens when the scattered light has the same wavelength as the incident light. In this case, the energy of incident light is conserved after vs. before the collision, which is called elastic collision (Bohning et al., 1998). The difference between the frequencies of the incident light and scattered light corresponds to a characteristic frequency of the molecule (Raman et al., 1928). The Raman shift is defined as the frequency difference between the measured incident light and the Raman scattered light. A Raman spectrum is the plot of the intensity of the Raman scattered light vs. the Raman shift measured as wavenumber (cm^{-1}).

Raman spectroscopy can be used to compare percent strain difference between strained and unstrained samples (Rice et al., 2013; Castellanos-Gomez et al., 2013).
For MoS_2, the Raman peak corresponding to the E_{2g} Raman mode is preferentially excited in the basal plane due to polarization dependence. The Raman peak corresponding to the A_{1g} Raman mode is preferentially excited along the c-axis (Verble et al., 1970). Figure 2.13 shows the atomic vibration directions of the E_{2g} and A_{1g} Raman modes of MoS_2 (Wang et al., 2013).

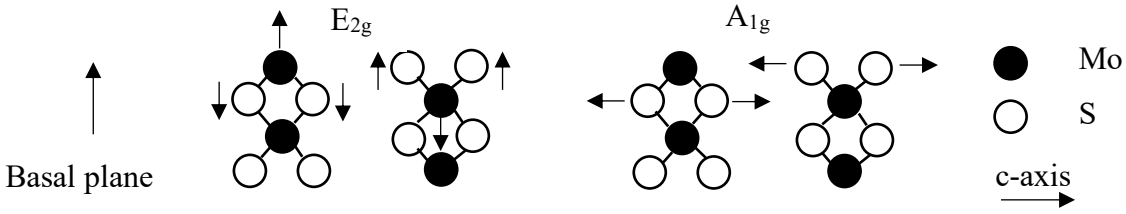

Figure 2.13. Illustrations of atomic vibration direction of E_{2g} Raman mode and A_{1g} Raman mode (Wang et al., 2013).

For MoS_2, the Raman shift -1.7 cm^{-1} of the E_{2g} Raman mode corresponds to 1 % strain (Rice et al., 2013; Castellanos-Gomez et al., 2013).

The intensity ratio between the A_{1g} and E_{2g} Raman modes can provide information on the texture of the sample. Vertically aligned MoS_2 has higher intensity ratio between A_{1g} and E_{2g} Raman modes, compared to MoS_2 film (Kong et al., 2013).

2.13 X-ray diffraction (XRD)

X-ray diffraction provides information about atomic and molecular arrangements in solids. Diffraction happens when radiation interacts with electron concentrations that can scatter the wave, and that are spaced at distances comparable in magnitude to the wavelength (Callister et al., 2014).

The phase relationship between the scattered waves can be classified into constructive interference and destructive interference. Constructive interference happens when the scattered waves remain in phase and thus mutually reinforce one another, giving rise to a diffracted beam. Destructive interference happens when the scattered waves become out of phase and thus cancel one another (Callister et al., 2014).

The wavelengths of x-rays are on the order of the atomic spacing of solids. The relationship between x-ray wavelengths, λ, interatomic spacing, d and angle of diffraction for constructive interference, θ is (Callister et al., 2014):

$$n\lambda = 2d_{hkl}\sin\theta$$

where n is the order of reflection (diffraction) and d_{hkl} is the distance between planes of atoms with Miller indices (h k l).

The above equation is known as Bragg's law. The interplanar spacing is a function of the Miller indices (h k l) and the unit cell dimensions. For example, in the case of crystals that have cubic symmetry and lattice parameter, a, the interplanar spacing is (Callister et al., 2014):

$$d_{hkl} = \frac{a}{\sqrt{h^2 + k^2 + l^2}}$$

2.14 Ultraviolet and visible light spectroscopy (UV-VIS)

UV-VIS can be used to determine the concentration of a solution by comparing the absorbance at wavelength, λ with the absorbance of a similar solution having a known solution concentration. The absorbance of UV-VIS radiation by a molecule may promote one or more of its valence electrons to higher energy state. Since different amounts of energy are required for different transitions, absorption occurs at different wavelengths,

depending on the chemical structure of the molecule. After the excitation, the molecule returns to its ground state and converts the excitation energy to another form, such as thermal energy (Temenoff et al., 2009).

CHAPTER 3: Results and Discussion

3.1 SEM of bulk MoS_2 powder and ce-MoS_2 sheets

Figure 3.1 shows scanning electron microscopy (SEM) images of MoS_2 powder as purchased and ce-MoS_2 on Si substrates. The SEM images illustrate that the particle size of ce-MoS_2 is smaller than that of MoS_2 powder. The longest diagonal of ce-MoS_2 is ~500 nm, which is consistent with results obtained for ce-MoS_2 by Chou et al., 2015.

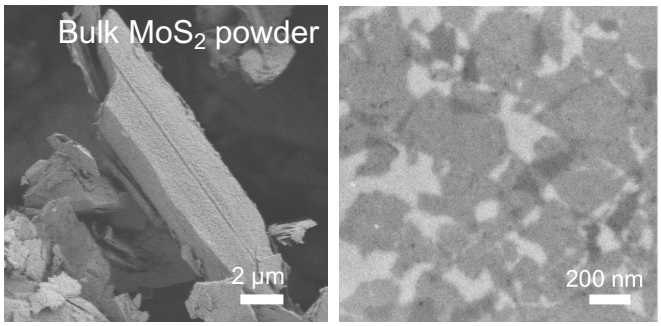

Figure 3.1. SEM images showing morphology of MoS_2 powder (left) and ce-MoS_2 (right).

3.2 AFM of ce-MoS_2 sheets

Figure 3.2 shows an atomic force microscopy (AFM) image of ce-MoS_2 on Si substrate. The sample was prepared by spin coating MoS_2 solution onto Si substrate, followed by drying at room temperature. The AFM image illustrates that the typical thickness of the ce-MoS_2 particles prepared by this method is ~1.8 nm. MoS_2 synthesized by Chou et al. and Late et al. are between 0.7 to 1.5 nm (Chou et al., 2014; Late et al., 2012). The spin-coat-deposited ce-MoS_2 in the present work could therefore consist of 2-3 layers. The steps lower than 0.7 nm could be because of the substrate (Si; diamond structure; lattice constant 0.543 nm; Lauhon et al., 2002).

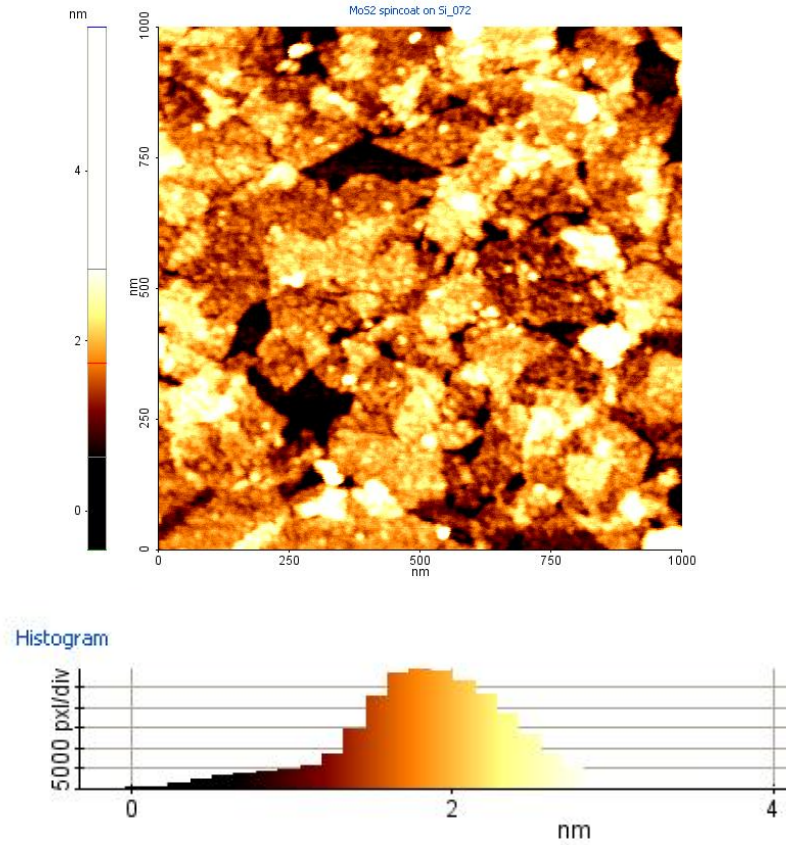

Figure 3.2. AFM image with histogram shows morphology of MoS_2 powder and ce-MoS_2. AFM was operated in tapping mode.

3.3 SEM of c-MoS_2 and FIST c-MoS_2

Figure 3.3 shows SEM images of c-MoS_2 and FIST c-MoS_2 on Si substrates. SEM images illustrate that FIST c-MoS_2 is more densely packed than c-MoS_2.

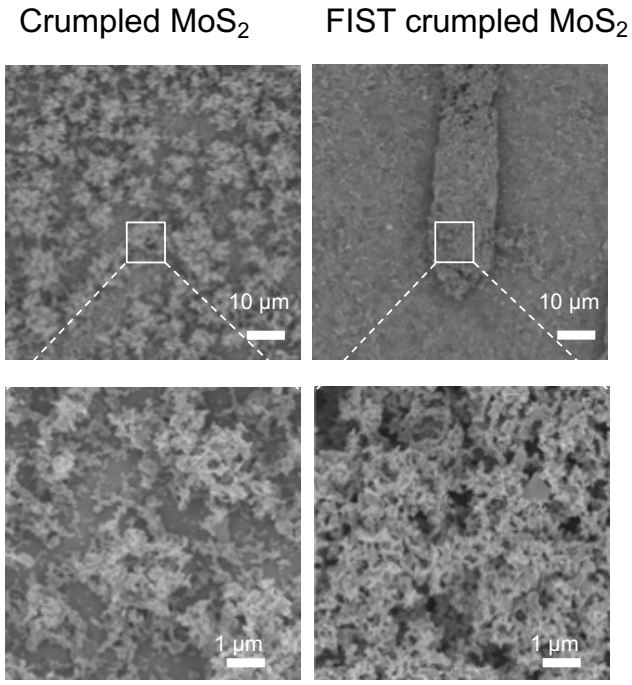

Figure 3.3. SEM images show morphology of c-MoS_2 and FIST c-MoS_2 on Si substrates.

3.4 EDS of FIST c-MoS_2

Figure 3.4 shows X-ray Energy-dispersive spectroscopy (EDS) images of FIST c-MoS_2 on Si substrate. EDS images confirm the presence of Mo and S elements in the area where the FIST c-MoS_2 is presumed to be.

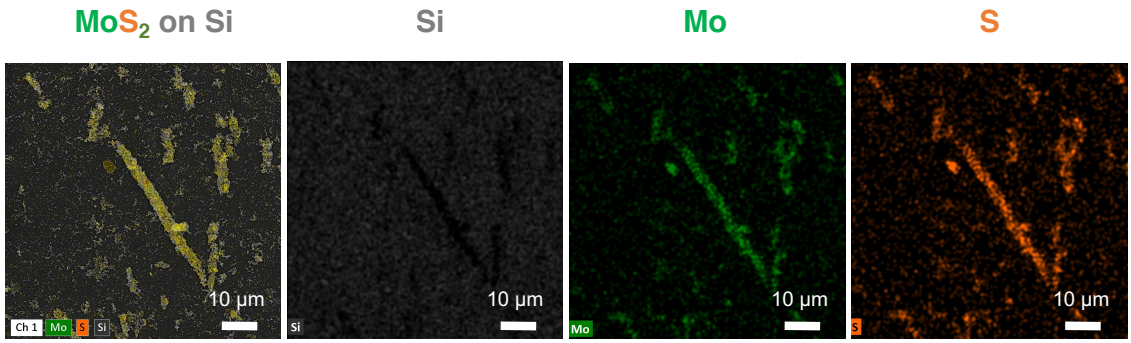

Figure 3.4. X-ray Energy-dispersive spectroscopy (EDS) images show elemental mapping of FIST c-MoS_2 on Si substrate. EDS was performed by Dr. V. Tung.

3.5 Raman Spectra of c-MoS_2 and FIST c-MoS_2

Figure 3.5 shows the Raman spectra of FIST c-MoS_2 and c-MoS_2. The E_{2g} and A_{1g} vibration modes of FIST c-MoS_2 locate at 379 cm^{-1} and 406 cm^{-1}, respectively. The E_{2g} and A_{1g} vibration modes of c-MoS_2 locate at 383 cm^{-1} and 406 cm^{-1}, respectively. For MoS_2, the Raman shift -1.7 cm^{-1} of E_{2g} Raman mode corresponds to 1 % strain (Rice et al., 2013; Castellanos-Gomezet al., 2013). The shift of the E_{2g} vibration mode indicates that the surface strain of FIST c-MoS_2 is 2.35% higher than c-MoS_2.

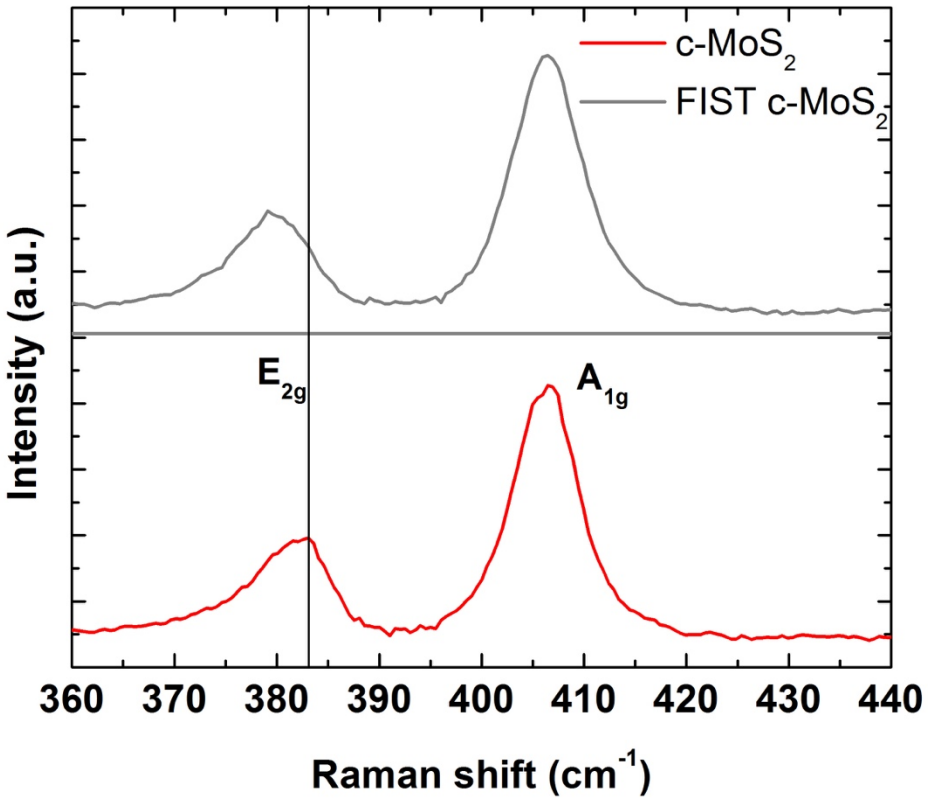

Figure 3.5 (repeated from figure 1.19). Raman spectroscopy of c-MoS_2 vs. FIST c-MoS_2. Raman spectra indicate that % strain of FIST c-MoS_2 is 2.35% higher than that of c-MoS_2. Raman data obtained from Dr. V. Tung.

Raman spectra were recorded using a confocal Raman microscope (Horiba Jobin Yvon, LabRam HR) with a 532 nm laser source. The excitation laser power at the sample surface was adjusted to be in the 1–2 mW range, and the spectral positions were calibrated by the characteristic Si phonon peak at 520.7 cm^{-1}.

3.6 XRD spectra of ce-MoS_2, c-MoS_2 and FIST c-MoS_2

Figure 3.6 shows the x-ray diffraction (XRD) spectra of ce-MoS_2, c-MoS_2 and FIST c-MoS_2 on Si substrate. XRD spectra illustrate that the degree (extent and/or perfection) of restacking in ce-MoS_2 is greater than that in c-MoS_2 and FIST c-MoS_2. The peak at 16˚ corresponds to (001) (Joensen et al., 1987). The XRD spectrum of FIST c-MoS_2 shows a peak at 16˚ which indicates a slightly higher degree of restacking in FIST c-MoS_2 compared to c-MoS_2. The XRD spectra of ce-MoS_2 illustrate that the sample has two phases of drying sequence (i) the presence of water between the MoS_2 layers (ii) the dry restacked MoS_2 (Joensen et al., 1987).

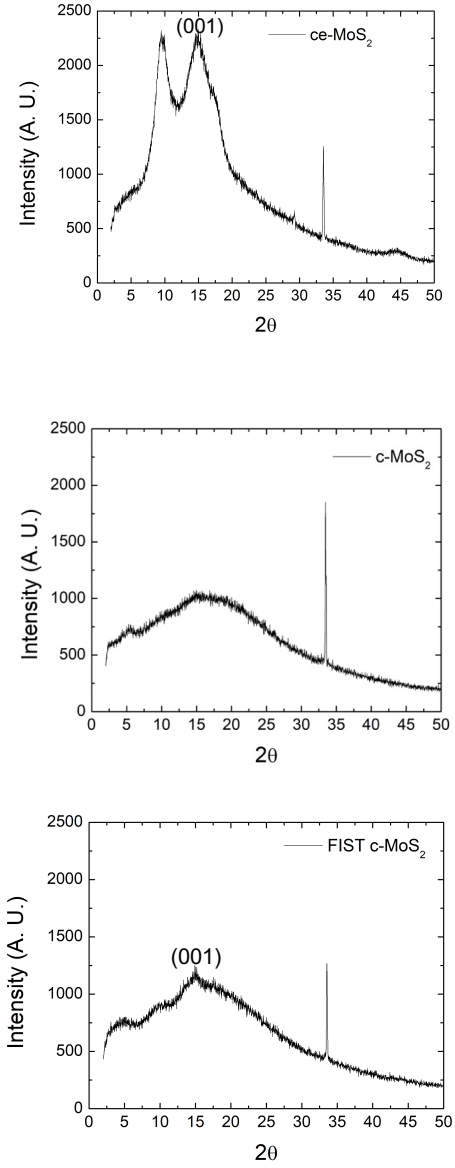

Figure 3.6. XRD spectra of ce-MoS_2, c-MoS_2 and FIST c-MoS_2. XRD was performed by X. Wei. The samples were prepared by the author.

The XRD data were collected using a Bruker AXS D8 Discover GADDS X-ray diffractometer (Cu Kα radiation, λ = 1.5418 Å).The interplanar spacing, *d* of ce-MoS_2 is calculated from the relationship between x-ray wavelength, λ, interplanar spacing, *d* and angle of diffraction for constructive interference, θ as noted in chapter 2. The interplanar spacings of ce-MoS_2 are summarized in Table 3.1.

Table 3.1. Interplanar spacing, d of ce-MoS_2.

	$2\boldsymbol{\theta} = 10^{\circ}$	16°
Interplanar spacing, *d* (Å)	8.85	5.54

3.7 Effect of sonication on filter paper mass

During the synthesis of ce-MoS_2, the filter paper is sonicated with MoS_2 cake and DI water for 3 minutes. An attempt was therefore made to test whether the materials from the filter paper contribute to the final ce-MoS_2 suspension. The filter paper is weighed and placed into a 250 mL glass bottle. 50 mL of DI water is added into the same glass bottle. The glass bottle with filter paper and DI water is sonicated for 3 minutes or 60 minutes. Then, the filter paper is dried on a Petri dish in a desiccator for 24 hours. After 24 hours, the filter paper is removed from the desiccator. The filter paper is weighed 24 hours, 48 hours, and 72 hours after being removed from the desiccator). The filter paper mass is changed due to humidity which causes high background noise. There is a limit of humidity control in the lab. After 72 hours, the mass of filter paper is 0.3 mg to 0.9 mg higher than the mass as received (~200 mg). The data are summarized in Table 3.2. These data are inconclusive with respect to determining whether the filter paper contributes material to the ce-MoS_2 suspension.

Table 3.2. Experimental conditions and mass difference.

	Sonication time (min)	Mass difference after removed from desiccator (mg)	Mass difference after 24 hours not in desiccator (mg)	Mass difference after 48 hours not in desiccator (mg)	Mass difference after 72 hours not in desiccator (mg)
Filter paper #1	3	-1.62	-0.93	+0.07	+0.65
Filter paper #2	3	-2	-1.17	-0.17	+0.46
Filter paper #3	3	-1.6	-0.91	+0.05	+0.6
Filter paper #4	60	-1.36	+0.08	+0.63	+0.28
Filter paper #5	60	-0.78	+0.58	+1.2	+0.9
Filter paper #6	60	-0.89	+0.41	+0.93	+0.62

3.8 HER activity of c-MoS_2 and FIST c-MoS_2 on stainless steel.

The electrochemical measurements are performed with a PRSTAT 2273 at room temperature. Pt mesh and Ag/AgCl (in saturated KCl) electrodes are used as the counter and reference electrodes, respectively. The HER activity is studied by linear sweep voltammetry (LSV) at sweep rates of 5 mV/s in 0.5 M H_2SO_4 electrolyte solution. The electrolyte solution is purged with high purity Ar for 30 minutes prior to the measurements. Electrochemical impedance spectroscopy (EIS) is performed at a potential of **0 V vs. Ag/AgCl**. The amplitude of the ac signal is 10 mV. Impedance is measured in the range of 10^4 to 0.01 Hz with 10 points/decade. The potentials vs. Ag/AgCl ($E_{Ag/AgCl}$) were converted to the reversible hydrogen electrode potential (E_{RHE}) scale according to the relationship (Wang et al., 2012):

$$E_{RHE} = E_{Ag/AgCl} + 0.059\text{pH} + E^0_{Ag/AgCl}$$

where $E^0_{Ag/AgCl}$ is 0.1976 V at 25˚C, and the pH of 0.5 M H_2SO_4 is 0.23. The pH was measured with Hannah Instruments Extended Range Portable pH Meter, HI 991001N.

Figure 3.7 shows LSV plot and EIS plot of c-MoS_2 and FIST c-MoS_2 on stainless steel. Each plot shows data averaged from 3 samples. Overpotential at 10 mA/cm^2, Tafel slope and exchange current density of MoS_2 catalysts are similar. The data are summarized in Table 3.3. EIS of all samples show similar trend after LSV which indicates that the surface area of all samples is changed.

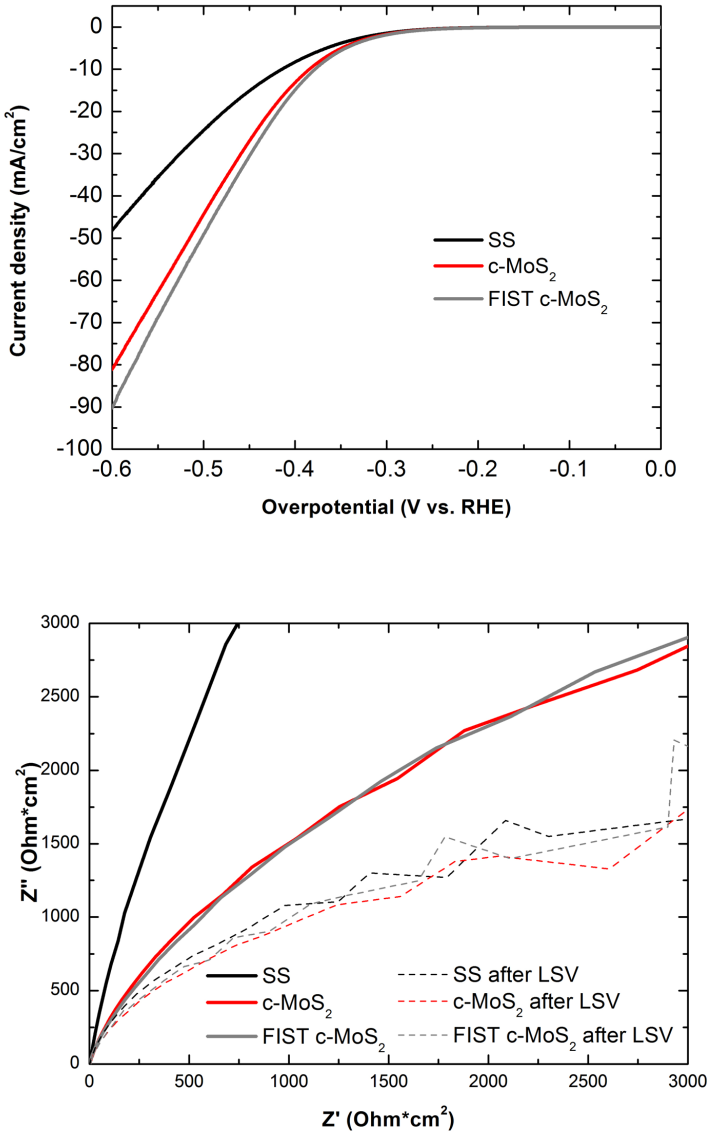

Figure 3.7. LSV plot and EIS plot of c-MoS_2 and FIST c-MoS_2 on stainless steel.

Table 3.3. Experimental conditions and HER activity (average data).

	Overpotential (mV)	Tafel slope (mV per dec)	Exchange current density ($\mu A/cm^2$)	Solution resistance (Ω)	Charge-transfer resistance (Ω)	Capacitance (mF/cm^2)	Capacitance after LSV (mF/cm^2)	Cycles	EHD Temperature (˚C)
SS	-415	114	3.02	2.25	N/A	0.107	0.109	1	N/A
c-MoS_2	-384	106	2.51	1.805	>3,000	0.115	0.170	1	25˚C
FIST c-MoS_2	-378	105	2.51	1.645	>3,000	0.112	0.234	1	25˚C

Figure 3.8 shows EIS plot of stainless steel before vs. after LSV at different potentials. EIS is performed at 0 V vs. Ag/AgCl. EIS reveals that surface area of stainless steel changes after LSV passed -0.4 V vs. RHE. The change in surface area could be due to the oxidation of stainless steel surface.

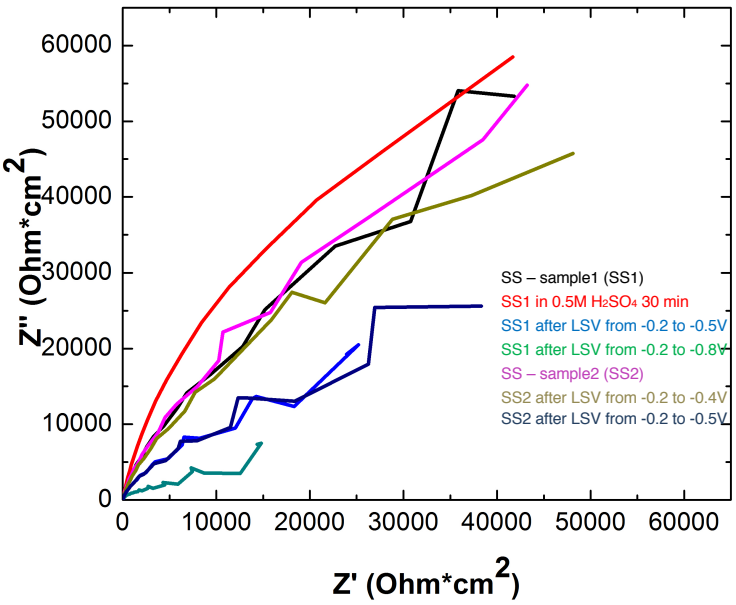

Figure 3.8. EIS plot of stainless steel before vs. after LSV at different potentials.

Figure 3.9 shows SEM images of FIST c-MoS_2 and c-MoS_2 on stainless steel before vs. after electrochemical testing. SEM images illustrate that FIST c-MoS_2 and c-MoS_2 remain on stainless steel after electrochemical testing. The coverage of FIST c-MoS_2 and c-MoS_2 on stainless steel is decreased by electrochemical testing.

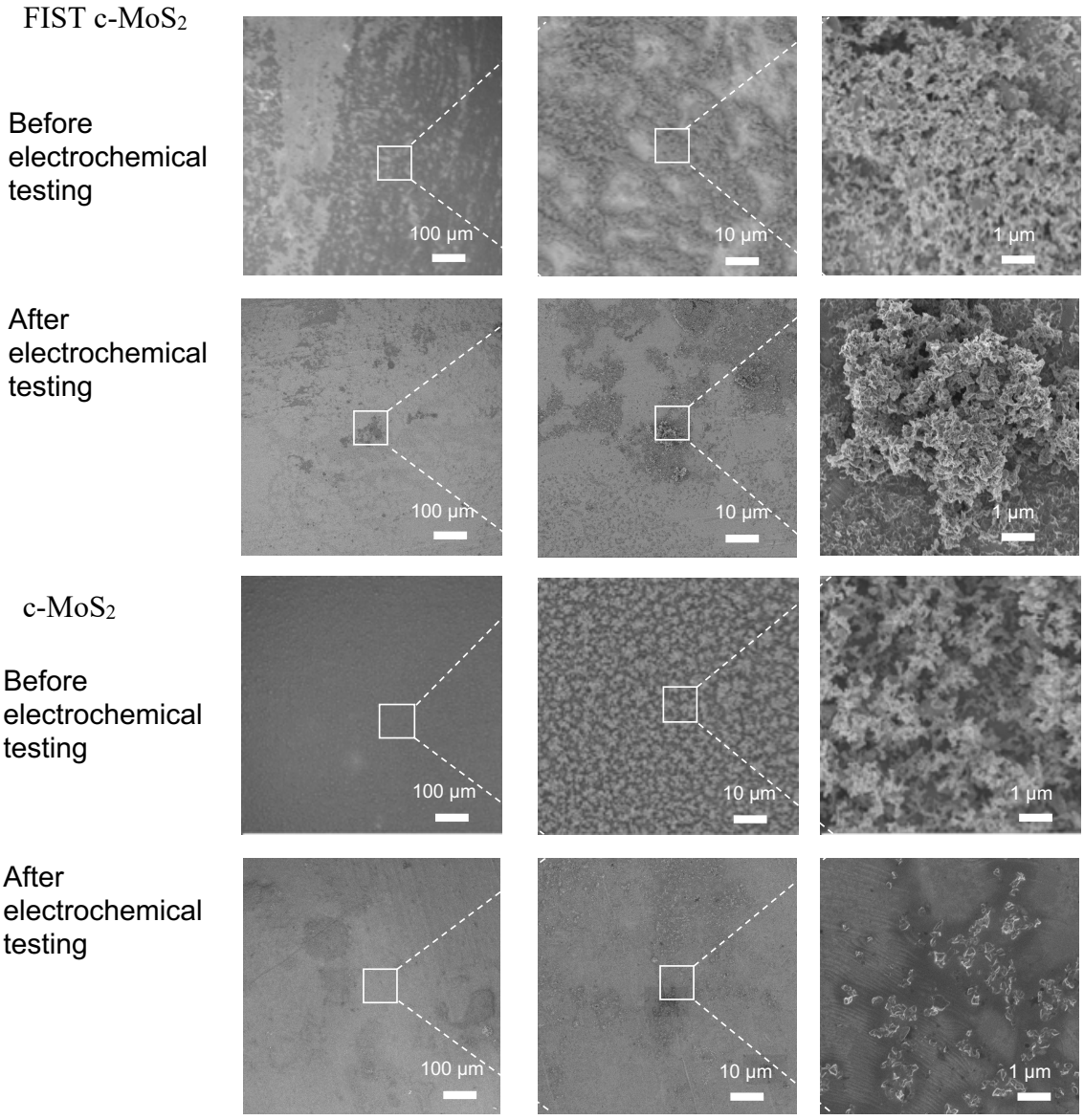

Figure 3.9. SEM images of FIST c-MoS_2 and c-MoS_2 on stainless steel before vs. after electrochemical testing.

This is the initial experiment which prompted the use carbon cloth substrate for the electrochemistry experiments in the present work.

3.9 HER activity and evidence for degradation of the electrode with LSV and EIS. For the electrochemistry experiments on carbon substrate, the samples are labeled as sample x.y where x is the experiment performed, and y is the number of the sample within the context of that experiment.

Electrochemical impedance spectroscopy (EIS) is performed at a potential of **-0.2 V vs. RHE**. The potential is chosen in the area where the current density increased significantly.

The experimental conditions and HER activity are summarized in Table 3.4 and 3.5. HER activity of all three MoS_2 catalysts is similar. The slightly lower overpotential at 10 mA/cm^2 of c-MoS_2 on ce-MoS_2, compared to (i) FIST c-MoS_2 on ce-MoS_2 and (ii) only ce-MoS_2, could be due to the slightly lower mass loading of ce-MoS_2. The slightly higher charge-transfer resistance of ce-MoS_2, compared to FIST c-MoS_2 on ce-MoS_2 and to c-MoS_2 on ce-MoS_2, could be due to the slightly higher mass loading of ce-MoS_2.

Table 3.4. Experimental 1, conditions and HER activity (data averaged from two samples in each MoS_2 catalyst).

	Overpotential (mV)	Tafel slope (mV per dec)	Exchange current density ($\mu A/cm^2$)	Solution resistance (Ω)	Charge-transfer resistance (Ω)	Capacitance (mF/cm^2)	Mass loading ($\mu g/cm^2$)	EHD Temperature (˚C)	Dip coat Temperature (˚C)
FIST c-MoS_2 on ce-MoS_2 5x	-709	113	0.00554	1.88	6.12	N/A	358	25˚C	25˚C
c-MoS_2 on ce-MoS_2 5x	-614	110	0.0278	1.65	6.12	N/A	350	25˚C	25˚C
ce-MoS_2 5x	-752	115	0.00304	1.73	7.13	N/A	392	N/A	25˚C
Carbon cloth	N/A	N/A	N/A	2.50	8941	0.01	N/A	N/A	N/A

Note: The mass loading of c-MoS_2 before FIST process is between 31 to 38 $\mu g/cm^2$.

Table 3.5. Experimental 1, conditions and HER activity (all samples).

	Overpotential (mV)	Tafel slope (mV per dec)	Exchange current density ($\mu A/cm^2$)	Solution resistance (Ω)	Charge-transfer resistance (Ω)	Capacitance (mF/cm^2)	Mass loading ($\mu g/cm^2$)	EHD Temperature (˚C)	Dip coat Temperature (˚C)
FIST c-MoS_2 on ce-MoS_2 5x 1.1	-706	113	0.00592	1.92	6.43	N/A	485	25˚C	25˚C
FIST c-MoS_2 on ce-MoS_2 5x 1.2	-712	113	0.00506	1.85	5.80	N/A	231	25˚C	25˚C
c-MoS_2 on ce-MoS_2 5x 1.1	-527	96.5	0.0350	1.56	5.39	N/A	338	25˚C	25˚C
c-MoS_2 on ce-MoS_2 5x 1.2	-712	105	0.00155	1.73	6.86	N/A	362	25˚C	25˚C
ce-MoS_2 5x 1.1	-756	122	0.00618	1.77	7.42	N/A	392	N/A	25˚C
ce-MoS_2 5x 1.2	-747	110	0.00153	1.69	6.83	N/A	N/A	N/A	25˚C
Carbon cloth	N/A	N/A	N/A	2.50	8941	0.01	N/A	N/A	N/A

Note: The mass loading of c-MoS_2 before FIST process is between 31 to 38 $\mu g/cm^2$.

Tafel slope of FIST c-MoS_2 on ce-MoS_2, c-MoS_2 on ce-MoS_2, and ce-MoS_2 on carbon cloth indicates that the samples have similar HER activity. The Tafel slope of MoS_2 catalysts close to 120 mV per dec indicates that the limiting step is a discharge step (Volmer reaction) (Li et al., 2011).

Figure 3.10 shows EIS plots of carbon cloth, FIST c-MoS_2 on ce-MoS_2 1.1, c-MoS_2 on ce-MoS_2 1.1, and ce-MoS_2 1.1, all on carbon cloth after LSV from 0 to -0.2 V vs. RHE and from 0 to -0.3 V vs. RHE on the same sample. EIS is performed at a potential of -0.2 V vs. RHE. Charge-transfer resistance of FIST c-MoS_2 on ce-MoS_2, c-MoS_2 on ce-MoS_2, and ce-MoS_2 on carbon cloth are higher after LSV from 0 V to -0.3 V vs. RHE compared to LSV from 0 V to -0.2 V vs. RHE, indicating that there is a degradation of the electrodes after LSV from 0 V to -0.3 V vs. RHE. The experimental conditions and electrochemical parameters are summarized in Table 3.6.

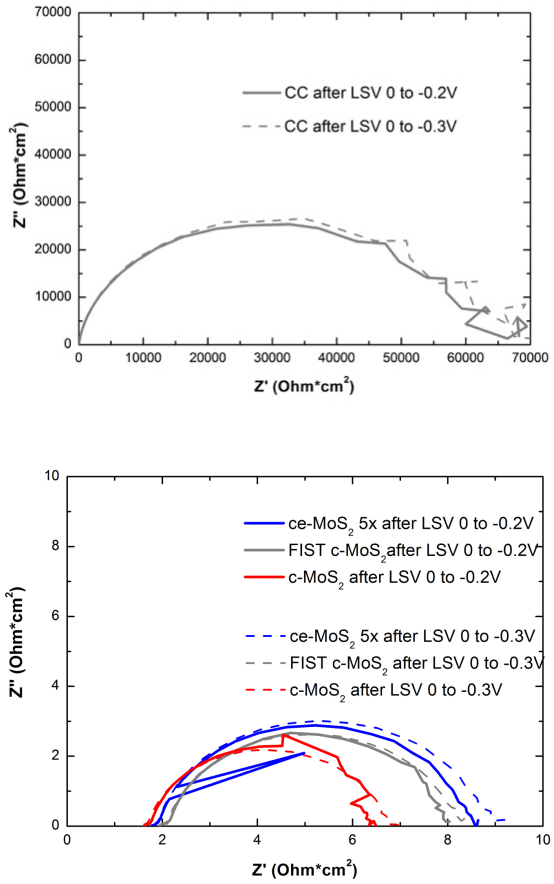

Figure 3.10. EIS plots of carbon cloth, FIST c-MoS_2 on ce-MoS_2 1.1, c-MoS_2 on ce-MoS_2 1.1, and ce-MoS_2 1.1, all on carbon cloth.

The sharp line of EIS data for ce-MoS_2 after LSV 0 to -0.2 V is due to a protruded fiber of carbon cloth. The sharp line does not affect the charge-transfer resistance value.

Table 3.6. Experimental 1, conditions for evidence of degradation and electrochemical parameters.

	EIS after LSV range (V vs. RHE)	Solution resistance (***Ω***)	Charge-transfer resistance (***Ω***)	Mass loading (μg/cm^2)	EHD Temperature (˚C)	Dip coat Temperature (˚C)
FIST c-MoS_2 on ce-MoS_2 5x 1.1	0 to -0.2	1.95	6.09	485	25˚C	25˚C
FIST c-MoS_2 on ce-MoS_2 5x 1.1	0 to -0.3	1.92	6.43	N/A	25˚C	25˚C
c-MoS_2 on ce-MoS_2 5x 1.1	0 to -0.2	1.622	4.87	338	25˚C	25˚C
c-MoS_2 on ce-MoS_2 5x 1.1	0 to -0.3	1.56	5.39	N/A	25˚C	25˚C
ce-MoS_2 5x 1.1	0 to -0.2	1.79	6.85	392	25˚C	25˚C
ce-MoS_2 5x 1.1	0 to -0.3	1.77	7.42	N/A	25˚C	25˚C
Carbon cloth	0 to -0.2	2.60	9616	N/A	N/A	N/A
Carbon cloth	0 to -0.3	2.50	8941	N/A	N/A	N/A

Note: The mass loading of c-MoS_2 before FIST process is between 31 to 38 μg/cm^2.

Figure 3.11 shows EIS plots of FIST c-MoS_2 on ce-MoS_2 1.2, c-MoS_2 on ce-MoS_2 1.2, and ce-MoS_2 1.2, all on carbon cloth after LSV from 0 to -0.2 V vs. RHE, from 0 to -0.3 V vs. RHE and from 0 to -0.45 V vs. RHE on the same sample. EIS is performed at a potential of -0.2 V vs. RHE. Charge-transfer resistance of MoS_2 catalysts are higher after LSV from 0V to -0.45 V vs. RHE compared to LSV from 0 V to -0.3 V vs. RHE and LSV from 0 V to -0.2 V vs. RHE, indicating that there is a degradation of the electrodes after LSV from 0 V to -0.3 V vs. RHE and LSV from 0 to -0.45 V vs. RHE. The experimental conditions and HER activity are summarized in Table 3.7.

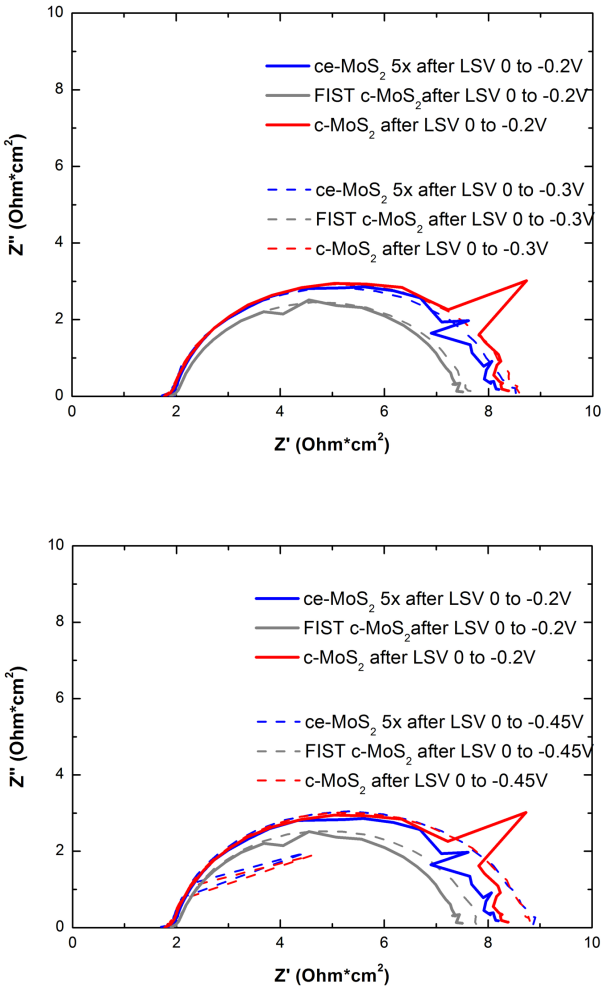

Figure 3.11. EIS plots of FIST c-MoS_2 on ce-MoS_2 1.2, c-MoS_2 on ce-MoS_2 1.2, and ce-MoS_2 1.2, all on carbon cloth.

The sharp line of EIS data for MoS_2 after LSV 0 to -0.2 V, c-MoS_2 after LSV 0 to -0.2 V, MoS_2 after LSV 0 to -0.45 V and c-MoS_2 after LSV 0 to -0. 45 V are due to a protruded fiber of carbon cloth. The sharp line does not affect the charge-transfer resistance value. The separate data is reported instead of the average data because of the sharp line.

Table 3.7. Experimental 1, conditions for evidence of degradation and electrochemical parameters.

	EIS after LSV range (V vs. RHE)	Solution resistance (***Ω***)	Charge-transfer resistance (***Ω***)	Mass loading (μg/cm^2)	EHD Temperature (˚C)	Dip coat Temperature (˚C)
FIST c-MoS_2 on ce-MoS_2 5x 1.2	0 to -0.2	1.90	5.60	231	25˚C	25˚C
FIST c-MoS_2 on ce-MoS_2 5x 1.2	0 to -0.3	1.85	5.80	N/A	25˚C	25˚C
FIST c-MoS_2 on ce-MoS_2 5x 1.2	0 to -0.45	1.83	5.94	N/A	25˚C	25˚C
c-MoS_2 on ce-MoS_2 5x 1.2	0 to -0.2	1.78	6.61	362	25˚C	25˚C
c-MoS_2 on ce-MoS_2 5x 1.2	0 to -0.3	1.73	6.86	N/A	25˚C	25˚C
c-MoS_2 on ce-MoS_2 5x 1.2	0 to -0.45	1.72	7.08	N/A	25˚C	25˚C
ce-MoS_2 5x 1.2	0 to -0.2	1.74	6.46	N/A	N/A	25˚C
ce-MoS_2 5x 1.2	0 to -0.3	1.69	6.83	N/A	N/A	25˚C
ce-MoS_2 5x 1.2	0 to -0.45	1.70	7.17	N/A	N/A	25˚C

Note: The mass loading of c-MoS_2 before FIST process is between 31 to 38 μg/cm^2.

3.10 HER activity after cyclic voltammetry.

The HER activity is studied by measuring LSV at sweep rates of 5 mV/s in 0.5 M H_2SO_4 electrolyte solution. The electrolyte solution is purged with high purity Ar for 30 minutes prior to the measurements. Cyclic voltammetry (CV) is performed at sweep rates of 50 mV/s.

Figure 3.12 shows LSV plot of FIST c-MoS_2 on ce-MoS_2 2.1 on carbon cloth before vs. after CV for 1,000 cycles. The experimental conditions and electrochemical parameters are summarized in Table 3.8 and 3.9. LSV reveals that the overpotential at 10 mA/cm^2 is lower (absolute value) after CV 1,000 cycles.

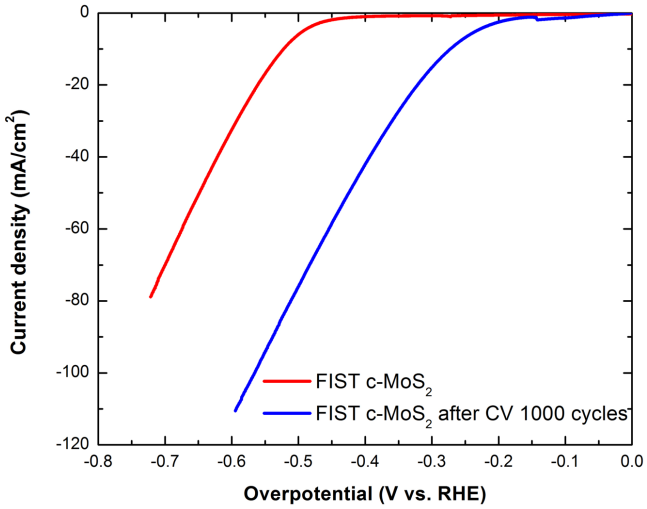

Figure 3.12. LSV of FIST c-MoS_2 on ce-MoS_2 2.1 on carbon cloth before vs. after cyclic voltammetry for 1,000 cycles.

Figure 3.13 shows CV of FIST c-MoS_2 on ce-MoS_2 2.1 on carbon cloth from cycle 1st to 1,000th with 100 cycles increment. CV reveals that the overpotential at 10 mA/cm^2 gradually decreases as the number of cycles increases.

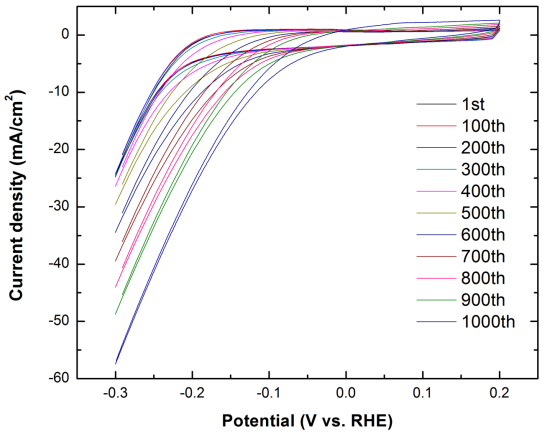

Figure 3.13. CV of FIST c-MoS_2 on ce-MoS_2 2.1 on carbon cloth from cycle 1st to 1,000th with 100 cycles increment.

Table 3.8. Experimental 2, conditions and HER activity (all samples).

	Overpotential (mV)	Tafel slope (mV per dec)	Exchange current density ($\mu A/cm^2$)	Potential for EIS (V vs. RHE)	Charge-transfer resistance (Ω)	Capacitance (mF/cm^2)	Mass loading ($\mu g/cm^2$)	Cycles
c-MoS_2 on ce-MoS_2 5x 2.1	-737	104	0.000762	-0.255	2.36	N/A	154	10
c-MoS_2 on ce-MoS_2 5x 2.1	-264	109	34.6	-0.119	4.31	N/A	N/A	1000
FIST c-MoS_2 on ce-MoS_2 5x 2.1	-523	94.8	0.0315	-0.251	2.45	N/A	177	10
FIST c-MoS_2 on ce-MoS_2 5x 2.1	-272	122	65.4	-0.128	5.24	N/A	N/A	1000
FIST c-MoS_2 on ce-MoS_2 5x 2.2	-532	95.5	0.0273	N/A	N/A	N/A	223	10
FIST c-MoS_2 on ce-MoS_2 5x 2.2	-165	88.4	143	N/A	N/A	N/A	N/A	1000
FIST c-MoS_2 on ce-MoS_2 5x 2.3	-523	96.3	0.0382	OCP	>784	9.42	185	10
FIST c-MoS_2 on ce-MoS_2 5x 2.3	-182	78.9	50.7	OCP	>383	12.5	N/A	1000
ce-MoS_2 5x 2.1	-559	101	0.0316	-0.263	2.80	N/A	146	10
ce-MoS_2 5x 2.1	-201	109	145	-0.097	3.69	N/A	N/A	1000
ce-MoS_2 5x 2.2	-538	92.6	0.0158	OCP	>1020	7.25	162	10
ce-MoS_2 5x 2.2	-155	94.7	240	OCP	>586	8.77	N/A	1000
ce-MoS_2 5x 2.3	-547	94.7	0.0172	OCP	>692	8.55	200	10
ce-MoS_2 5x 2.3	-236	112	80.2	OCP	>533	9.27	N/A	1000
CC	-715	382	137	-0.715	11.9	N/A	N/A	10
CC	-350	202	187	-0.350	5.79	N/A	N/A	1000

Note: The mass loading of c-MoS_2 before FIST process is 23 $\mu g/cm^2$. Dip coating ce-MoS_2 at 25˚C. OCP stands for open circuit potential.

Table 3.9. Experimental 2, conditions and HER activity (average LSV data for FIST c-MoS_2 and ce-MoS_2, 3 samples each).

	Overpotential (mV)	Tafel slope (mV per dec)	Exchange current density ($\mu A/cm^2$)	Potential for EIS (V vs. RHE)	Charge-transfer resistance (Ω)	Capacitance (mF/cm^2)	Mass loading ($\mu g/cm^2$)	Cycles
c-MoS_2 on ce-MoS_2 5x	-737	104	0.000762	N/A	N/A	N/A	154	10
c-MoS_2 on ce-MoS_2 5x	-264	109	34.6	N/A	N/A	N/A	N/A	1000
FIST c-MoS_2 on ce-MoS_2 5x	-526	95.5	0.0320	0 V vs. OCP	>784	9.42	195, 185	10
FIST c-MoS_2 on ce-MoS_2 5x	-196	91.9	75.9	0 V vs. OCP	>383	12.5	N/A	1000
ce-MoS_2 5x	-548	96.5	0.0216	0 V vs. OCP	>858	7.85	169, 181	10
ce-MoS_2 5x	-194	109	168	0 V vs. OCP	>560	9.01	N/A	1000
CC	-715	382	137	N/A	N/A	N/A	N/A	10
CC	-350	202	187	N/A	N/A	N/A	N/A	1000

Blue numbers are the data use in LSV. Red numbers are the data use in EIS at 0 V vs. OCP.

Overpotential at 10 mA/cm^2 of MoS_2 catalysts and carbon cloth are lower (absolute value) after CV 1,000 cycles. EIS is performed at 0 V vs. OCP to gain an understanding of the reason for lower overpotential at 10 mA/cm^2 of MoS_2 catalysts.

EIS at 0 V vs. OCP is used for capacitance calculation because the phase of *Z* (deg) is closer to 90˚ where the electrode behaves as a capacitor.

Figure 3.14 compares Bode phase data of FIST c-MoS_2 on ce-MoS_2 on carbon cloth at (i) the potential that gave 10 mA/cm^2 vs. RHE, and (ii) 0 V vs. OCP.

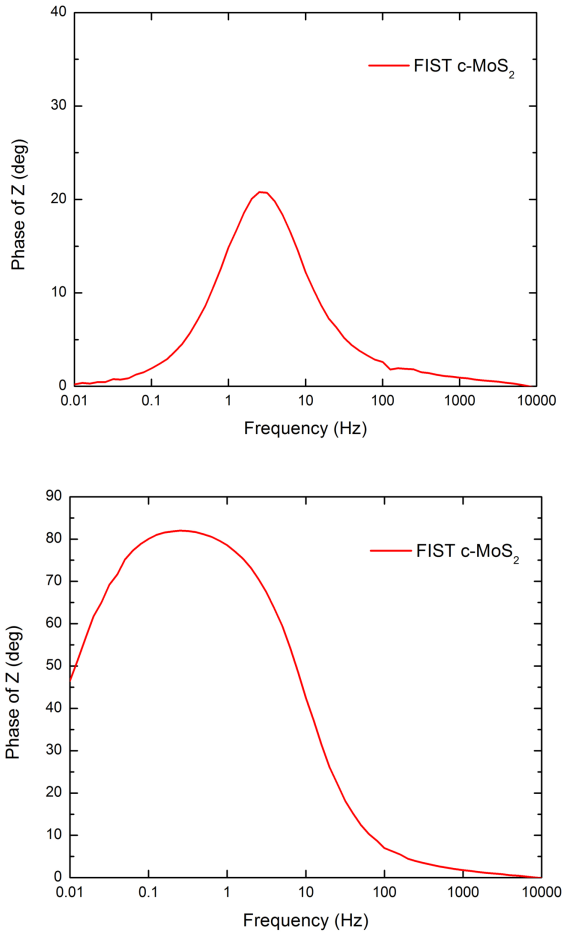

EIS at potential gave 10 mA/cm^2

EIS at 0 V vs. OCP

Figure 3.14. Bode phase data of FIST c-MoS_2 on ce-MoS_2 on carbon cloth at (i) the potential that gave 10 mA/cm^2 vs. RHE, and (ii) 0 V vs. OCP.

Figure 3.15 shows SEM images of ce-MoS_2 on carbon cloth before vs. after electrochemical testing. The images illustrate that ce-MoS_2 remain on carbon cloth after electrochemical testing.

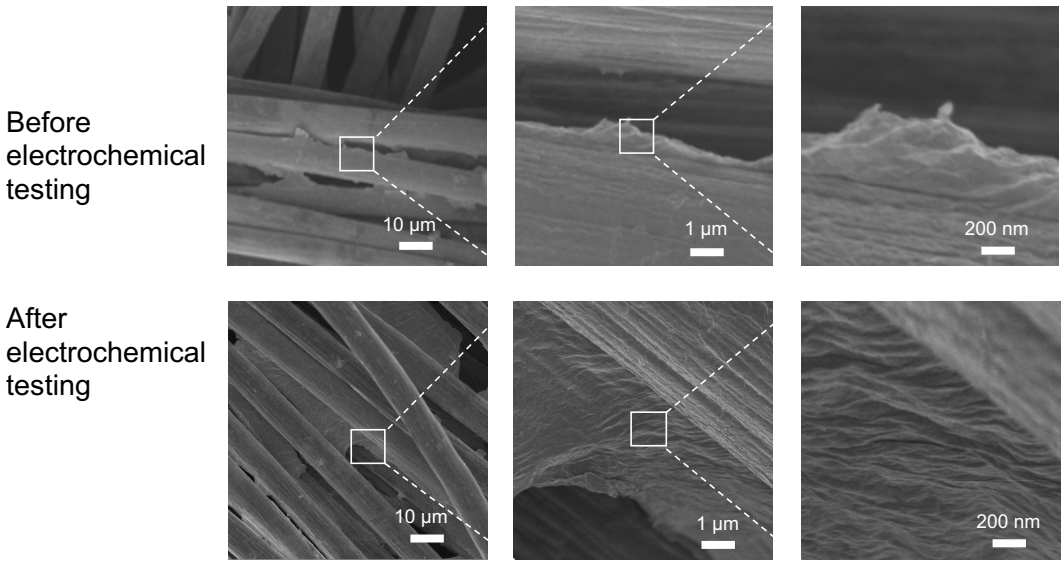

Figure 3.15. SEM images of ce-MoS_2 on carbon cloth before vs. after electrochemical testing.

Figure 3.16 shows SEM images of c-MoS_2 on ce-MoS_2 on carbon cloth before vs. after electrochemical testing. The images illustrate that c-MoS_2 and ce-MoS_2 remain on the carbon cloth after electrochemical testing.

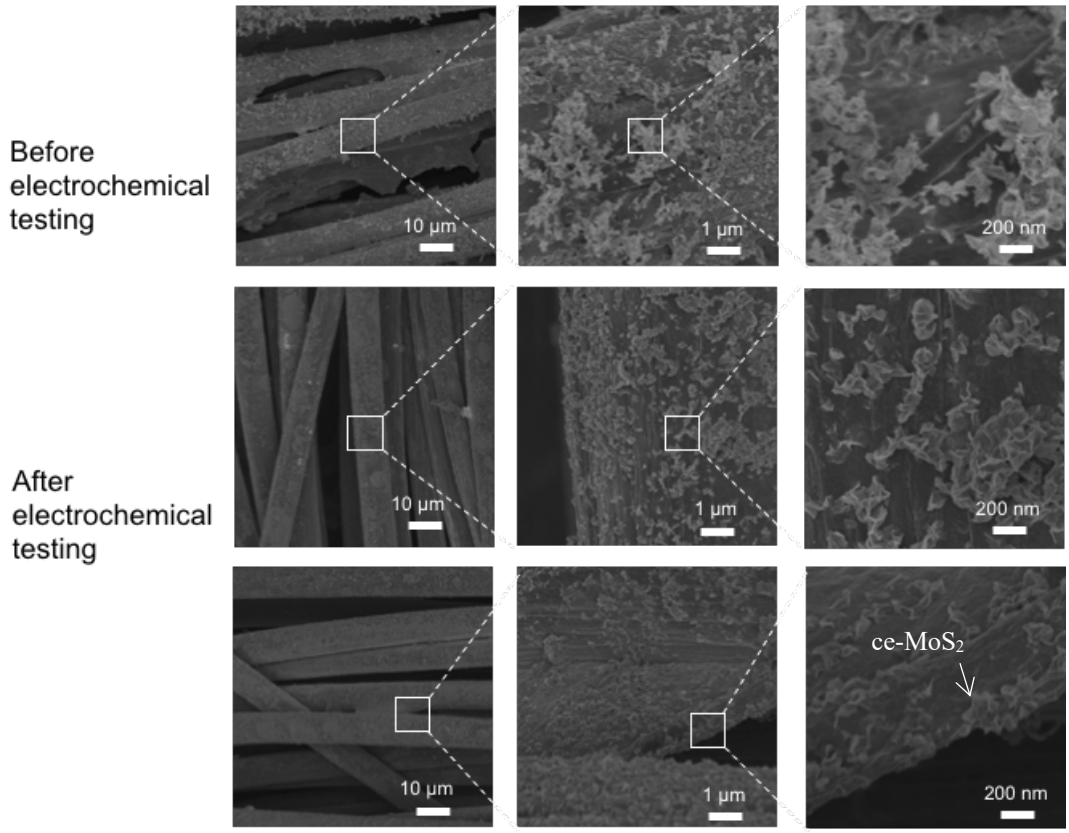

Figure 3.16. SEM images of c-MoS_2 on ce-MoS_2 on carbon cloth before vs. after electrochemical testing.

Figure 3.17 shows SEM images of FIST c-MoS_2 on ce-MoS_2 on carbon cloth before vs. after electrochemical testing. SEM images illustrate that FIST c-MoS_2 and ce-MoS_2 remain on the carbon cloth after electrochemical testing.

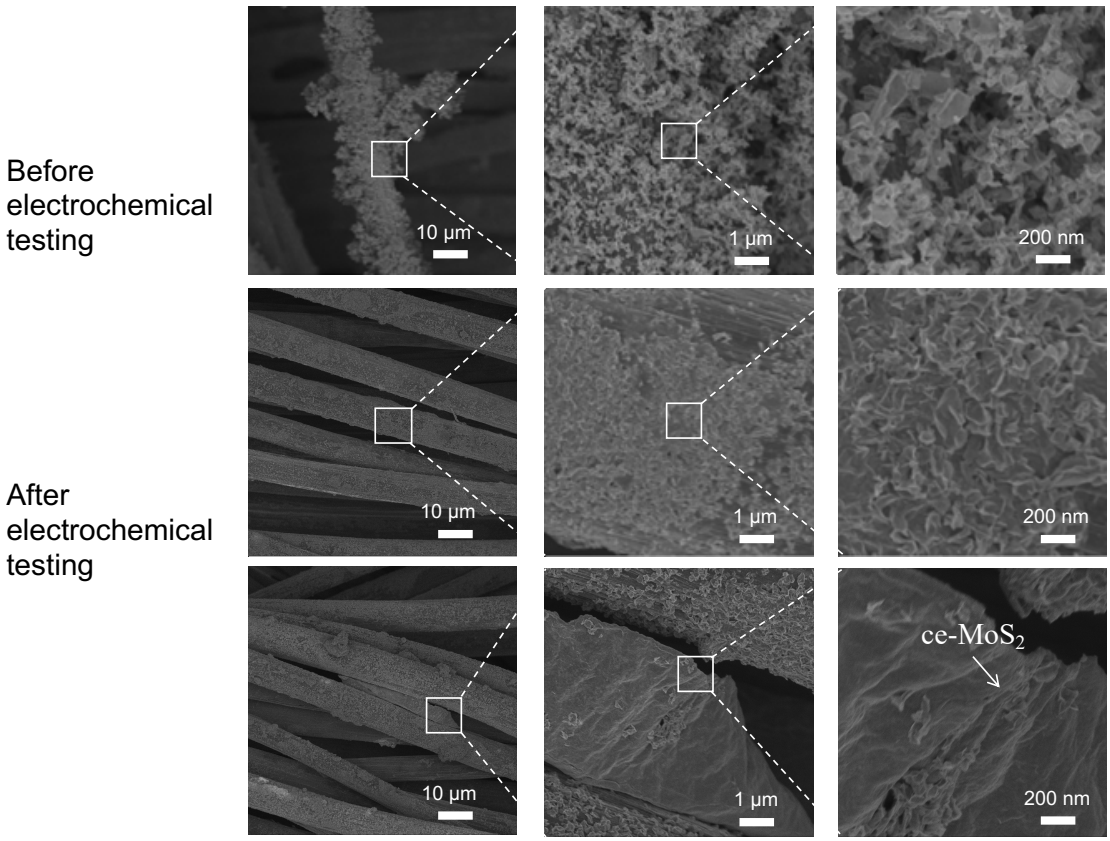

Figure 3.17. SEM images of FIST c-MoS_2 on ce-MoS_2 on carbon cloth before vs. after electrochemical testing.

Figure 3.18 shows LSV plot of c-MoS_2 on ce-MoS_2 2.1 on carbon cloth before vs. after cyclic voltammetry for 1,000 cycles. The experimental conditions and electrochemical parameters are summarized in Table 3.8 and 3.9. LSV reveals that the overpotential at 10 mA/cm^2 is lower after CV 1,000 cycles.

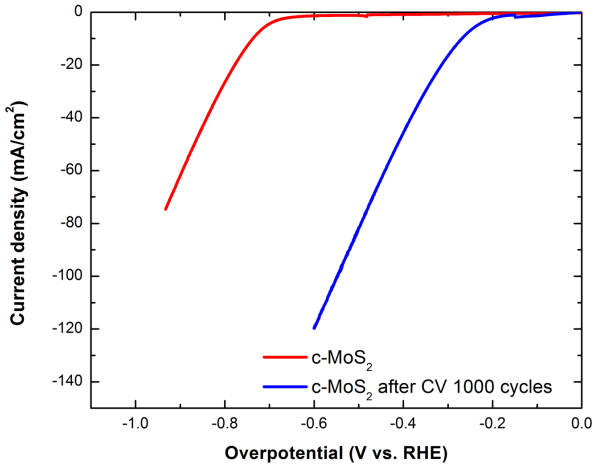

Figure 3.18. LSV of c-MoS_2 on ce-MoS_2 2.1 on carbon cloth before vs. after cyclic voltammetry for 1,000 cycles.

Figure 3.19 shows CV of c-MoS_2 on ce-MoS_2 on carbon cloth from cycle 1st to 1,000th with 100 cycles increment. CV reveals that the overpotential at 10 mA/cm^2 is gradually lower.

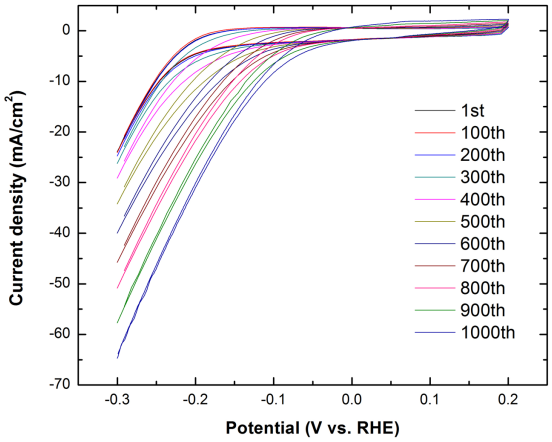

Figure 3.19. CV of c-MoS_2 on ce-MoS_2 on carbon cloth from cycle 1st to 1,000th with 100 cycles increment.

Figure 3.20 shows LSV plot of ce-MoS_2 2.1 on carbon cloth before vs. after cyclic voltammetry for 1,000 cycles. The experimental conditions and electrochemical parameters are summarized in Table 3.8 and 3.9. LSV reveals that the overpotential at 10 mA/cm^2 is lower after CV 1,000 cycles.

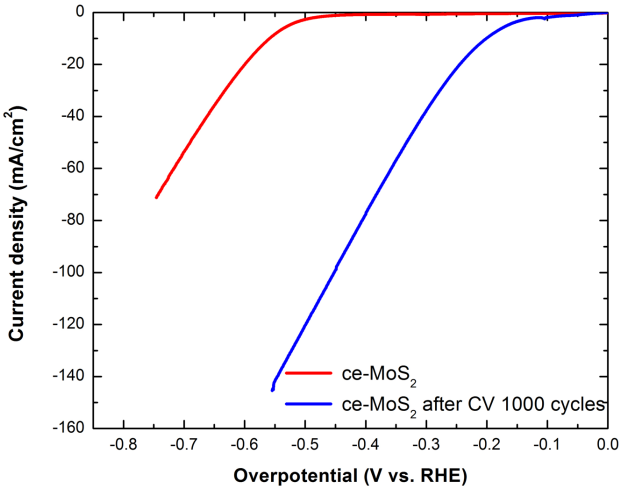

Figure 3.20. LSV of ce-MoS_2 2.1 on carbon cloth before vs. after cyclic voltammetry for 1,000 cycles.

Figure 3.21 shows CV of ce-MoS_2 2.1 on carbon cloth from cycle 1st to 1,000th with 100 cycles increment. CV reveals that the overpotential at 10 mA/cm^2 gradually decreases as the number of cycles increases.

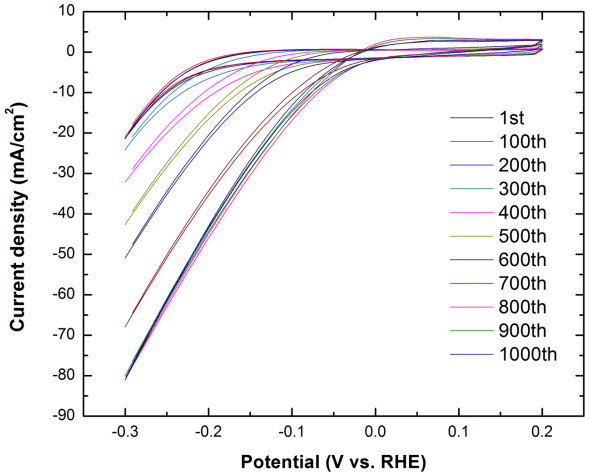

Figure 3.21. CV of ce-MoS_2 2.1 on carbon cloth from cycle 1st to 1,000th with 100 cycles increment. CV reveals that the overpotential at 10 mA/cm^2 gradually decreases as the number of cycles increases.

Figure 3.22 shows LSV plot of carbon cloth before vs. after cyclic voltammetry for 1,000 cycles. The experimental conditions and electrochemical parameters are summarized in Table 3.8 and 3.9. LSV reveals that the overpotential at 10 mA/cm^2 is lower after CV 1,000 cycles.

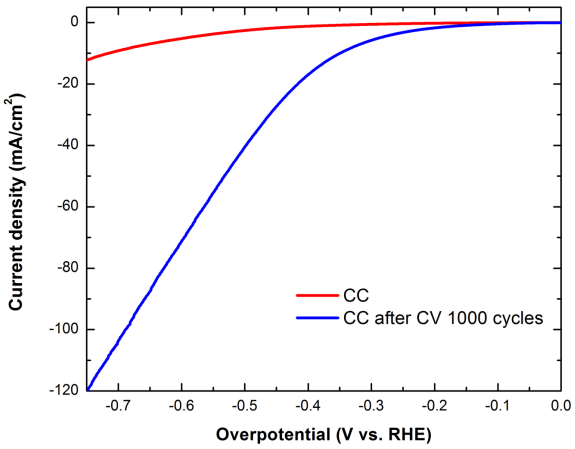

Figure 3.22. LSV of carbon cloth before vs. after cyclic voltammetry for 1,000 cycles.

Figure 3.23 shows CV of carbon cloth from cycle 1st to 1,000th with 100 cycles increment. CV reveals that the overpotential at 10 mA/cm^2 gradually decreases as the number of cycles increases.

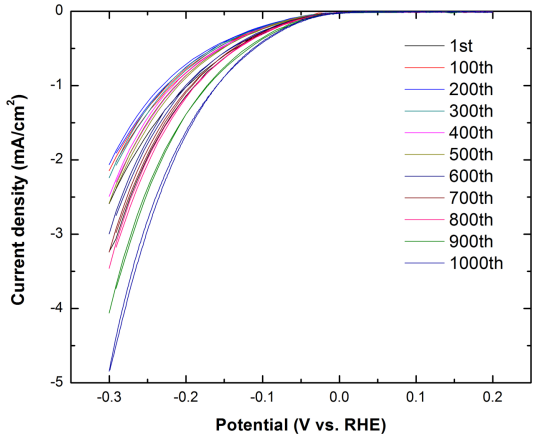

Figure 3.23. CV of carbon cloth from cycle 1st to 1,000th with 100 cycles increment.

Figure 3.24 shows carbon cloth in electrolyte before and after electrochemical testing. The images illustrate that after electrochemical testing, the wettability of the electrode is improved. Wettability could be one of the factors for the lower overpotential at 10 mA/cm^2 after CV 1,000 cycles.

Figure 3.24. Carbon cloth in electrolyte and after electrochemical testing.

Figure 3.25 shows LSV plot of FIST c-MoS_2 on ce-MoS_2 2.1, c-MoS_2 on ce-MoS_2 2.1, and ce-MoS_2 2.1, all on carbon cloth before vs. after cyclic voltammetry for 1,000 cycles.

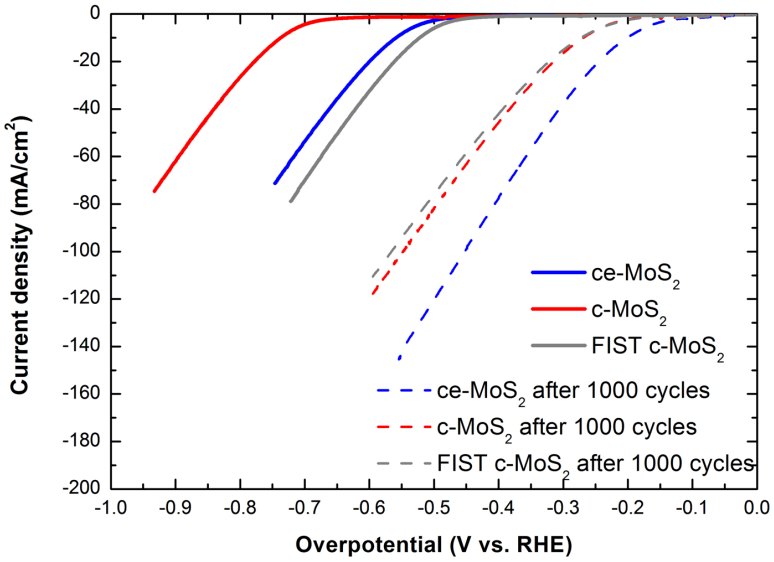

Figure 3.25. LSV of FIST c-MoS_2 on ce-MoS_2 2.1, c-MoS_2 on ce-MoS_2 2.1, and ce-MoS_2 2.1, all on carbon cloth before vs. after cyclic voltammetry for 1,000 cycles.

The Tafel slope before subjecting samples to CV 1,000 cycles is similar for all the MoS_2 catalysts. The difference in overpotential at 10 mA/cm^2 between the MoS_2 catalysts before and after CV 1,000 cycles could be due to the difference in mass loading of ce-MoS_2. Since the MoS_2 catalysts show similar Tafel slope before subjecting samples to CV 1,000 cycles, only one sample of c-MoS_2 on ce-MoS_2 was tested.

Figure 3.26 shows LSV plot and CV plot of FIST c-MoS_2 on ce-MoS_2 2.2. CV data are plotted from cycle 1st to 1,000th with 100 cycles increment. LSV reveals that the overpotential at 10 mA/cm^2 is lower after CV 1,000 cycles. CV reveals that the overpotential at 10 mA/cm^2 gradually decreases as the number of cycles increases.

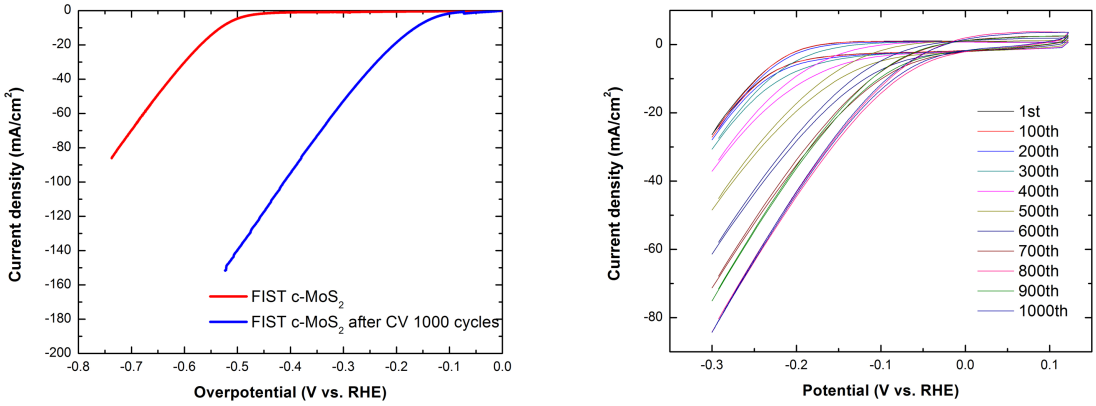

Figure 3.26. LSV and CV of FIST c-MoS_2 on ce-MoS_2 2.2 on carbon cloth. CV data are plotted from cycle 1st to 1,000th with 100 cycles increment.

Figure 3.27 shows the LSV plot and EIS plot of ce-MoS_2 2.2 before vs. after cyclic voltammetry for 1,000 cycles. **EIS is performed at a potential of 0 V vs. open circuit potential (OCP).** The increase in capacitance after CV 1,000 cycles indicates that the lower overpotential after CV 1,000 cycles could be due to the change in surface area of the electrode. The data are summarized in Table 3.8 and 3.9.

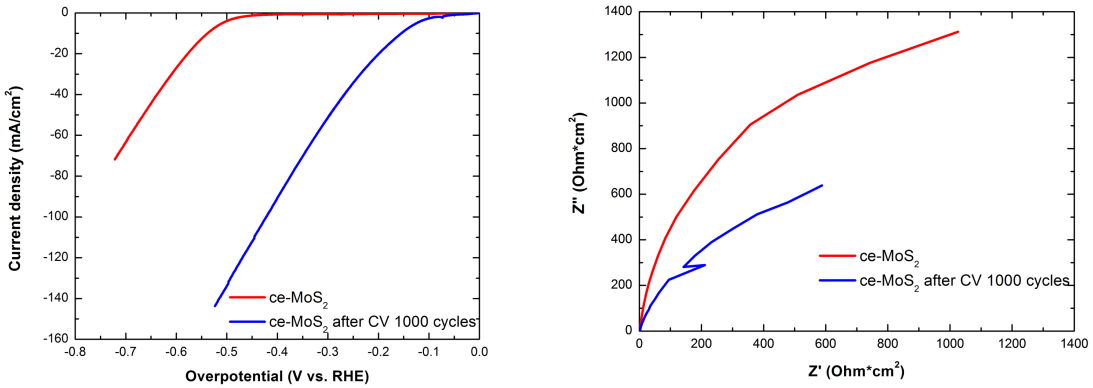

Figure 3.27. LSV and EIS of ce-MoS_2 2.2 on carbon cloth before vs. after cyclic voltammetry for 1,000 cycles.

The sharp line of EIS data for MoS_2 after CV 1,000 cycles is due to a protruded fiber of carbon cloth. The sharp line does not affect the capacitance calculation because the impedance and frequency at the maximum phase of *Z* (deg) are used, which occurs before the sharp line.

Figure 3.28 shows CV of ce-MoS_2 2.2 on carbon cloth from cycle 1st to 1,000th with 100 cycles increment. CV reveals that the overpotential at 10 mA/cm^2 gradually decreases as the number of cycles increases.

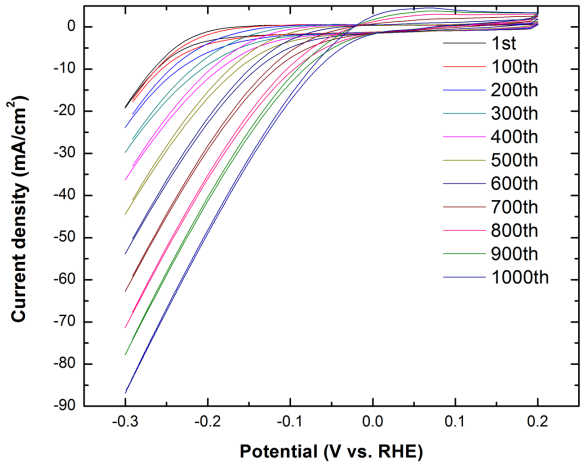

Figure 3.28. CV of ce-MoS_2 2.2 on carbon cloth from cycle 1st to 1,000th with 100 cycles increment.

Figure 3.29 shows LSV plot and EIS plot of ce-MoS_2 2.3 on carbon cloth before vs. after cyclic voltammetry for 1,000 cycles. EIS is performed at a potential of 0 V vs. open circuit potential (OCP). The data are summarized in Table 3.8 and 3.9. LSV reveals that the overpotential at 10 mA/cm^2 is lower after CV 1,000 cycles.

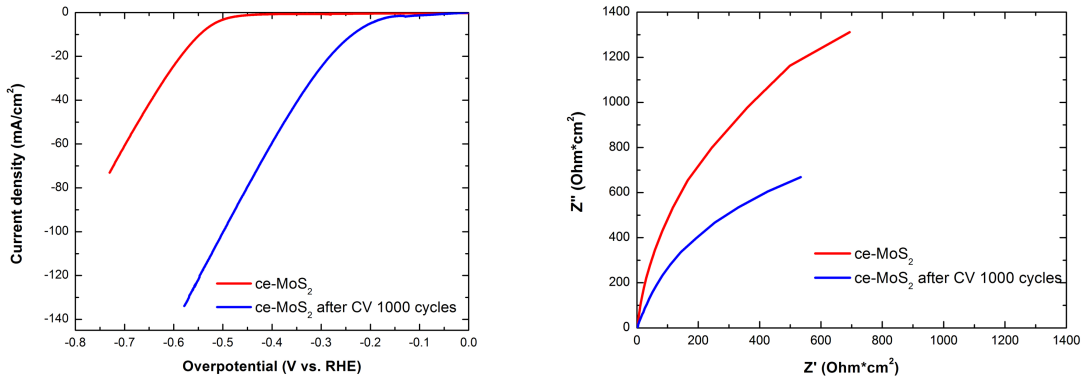

Figure 3.29. LSV and EIS of ce-MoS_2 2.3 on carbon cloth before vs. after cyclic voltammetry for 1,000 cycles.

Figure 3.30 shows CV of ce-MoS_2 2.3 on carbon cloth from cycle 1st to 1,000th with 100 cycles increment. CV reveals that the overpotential at 10 mA/cm^2 gradually decreases as the number of cycles increases.

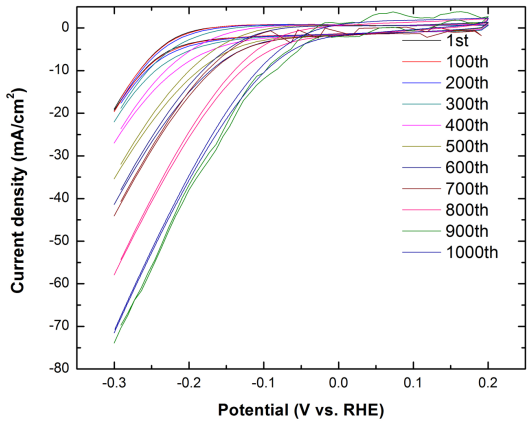

Figure 3.30. CV of ce-MoS_2 2.3 on carbon cloth from cycle 1st to 1,000th with 100 cycles increment.

Figure 3.31 shows LSV plot and EIS plot of FIST c-MoS_2 on ce-MoS_2 2.3 on carbon cloth before vs. after cyclic voltammetry for 1,000 cycles. EIS is performed at a potential of 0 V vs. open circuit potential (OCP). The data are summarized in Table 3.8 and 3.9. LSV reveals that the overpotential at 10 mA/cm^2 is lower after CV 1,000 cycles.

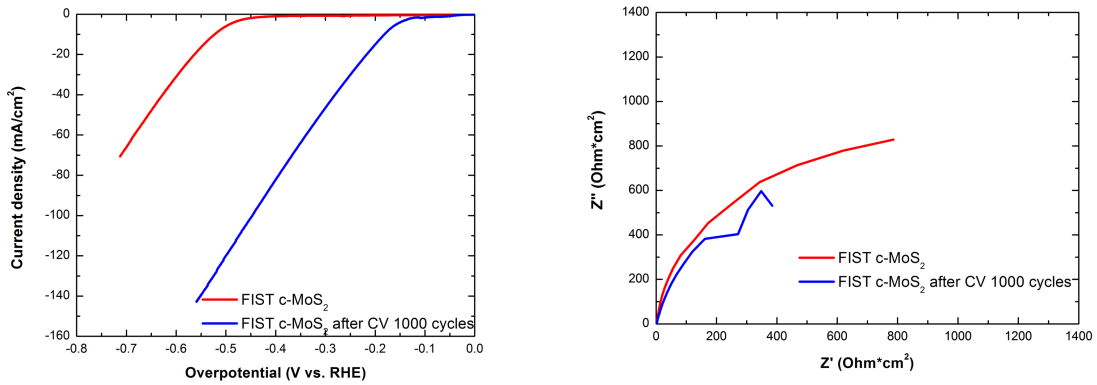

Figure 3.31. LSV and EIS of FIST c-MoS_2 on ce-MoS_2 2.3 on carbon cloth before vs. after cyclic voltammetry for 1,000 cycles.

The sharp line of EIS data for FIST c-MoS_2 #3 after CV 1,000 cycles is due to a protruded fiber of carbon cloth. The sharp line does not affect the capacitance calculation because the impedance and frequency at the maximum phase of *Z* (deg) are used, which occurs before the sharp line.

Figure 3.32 shows CV of FIST c-MoS_2 2.3 on ce-MoS_2 on carbon cloth from cycle 1st to 1,000th with 100 cycles increment. CV reveals that the overpotential at 10 mA/cm^2 gradually decreases as the number of cycles increases.

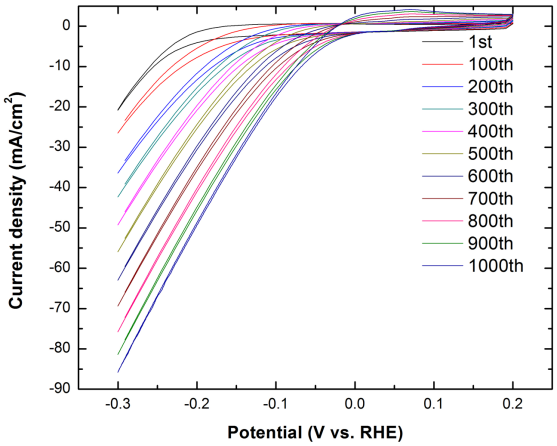

Figure 3.32. CV of FIST c-MoS_2 on ce-MoS_2 2.3 on carbon cloth from cycle 1st to 1,000th with 100 cycles increment.

Figure 3.33 shows ce-MoS_2 2.2 on carbon cloth in electrolyte before and after electrochemical testing. The images illustrate that after electrochemical testing, the wettability of the electrode is improved.

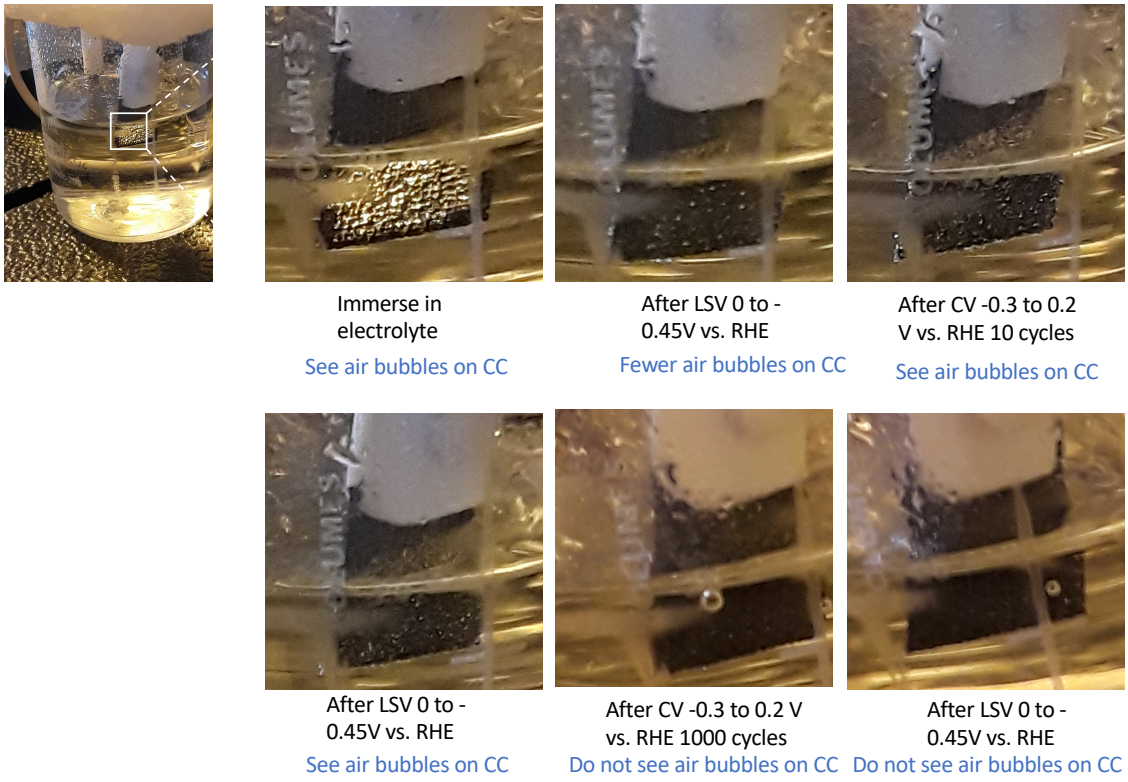

Figure 3.33. ce-MoS_2 2.2 on carbon cloth in electrolyte before and after electrochemical testing.

Figure 3.34 shows ce-MoS_2 2.3 on carbon cloth in electrolyte before and after electrochemical testing. The images illustrate that after electrochemical testing, the wettability of the electrode is improved.

Figure 3.34. ce-MoS_2 2.3 on carbon cloth in electrolyte before and after electrochemical testing.

Figure 3.35 shows FIST c-MoS_2 on ce-MoS_2 2.3 on carbon cloth in electrolyte before and after electrochemical testing. The images illustrate that after electrochemical testing, the wettability of the electrode is improved.

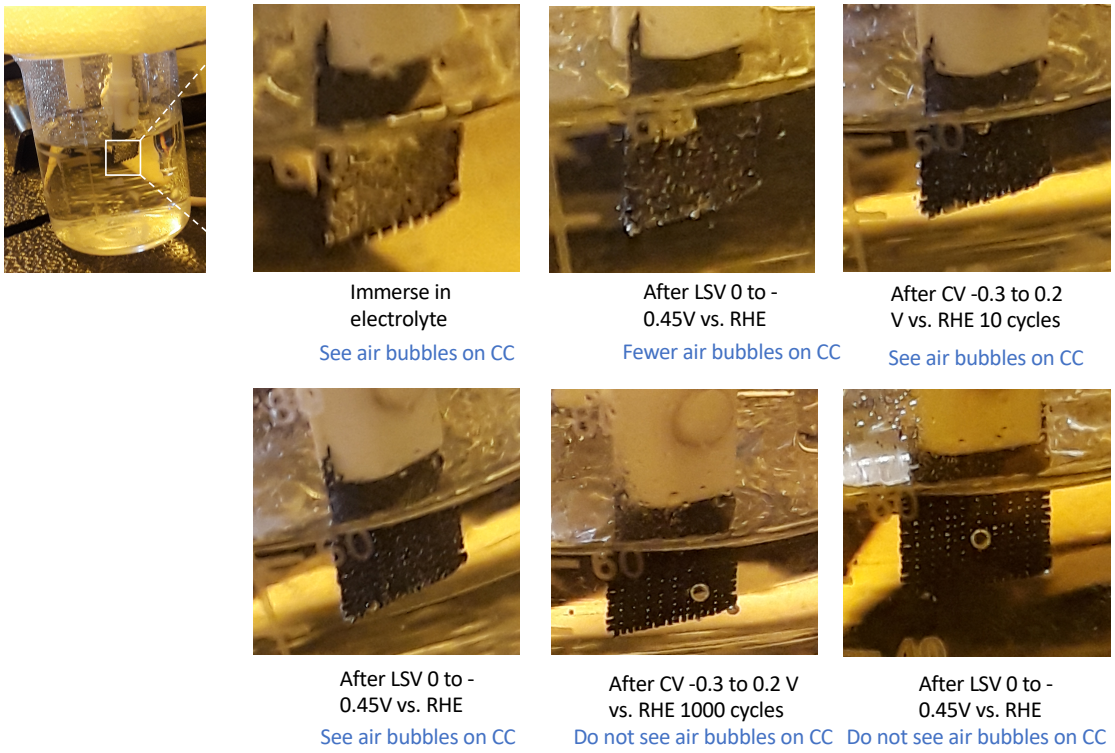

Figure 3.35. FIST c-MoS_2 on ce-MoS_2 2.3 on carbon cloth in electrolyte before and after electrochemical testing.

The decrease in the overpotential at 10 mA/cm^2 of the samples after CV 1,000 cycles could be because of the increase in surface area (capacitance) and the wettability.

3.11 Effect of the number of ce-MoS_2 dip coat steps on HER activity.
Figure 3.36 shows LSV plot and EIS plot of FIST c-MoS_2 on ce-MoS_2, c-MoS_2 on ce-MoS_2, and ce-MoS_2 on carbon cloth. Each plot shows data averaged from 3 samples. **EIS is performed at 0 V vs. Ag/AgCl.** Overpotential at 10 mA/cm^2, Tafel slope and exchange current density of all the MoS_2 catalysts are similar. The slight differences in behavior exhibited by the catalysts could be due to a slight difference in mass and surface area of ce-MoS_2 on carbon cloth. The data are summarized in Table 3.10 and 3.11.

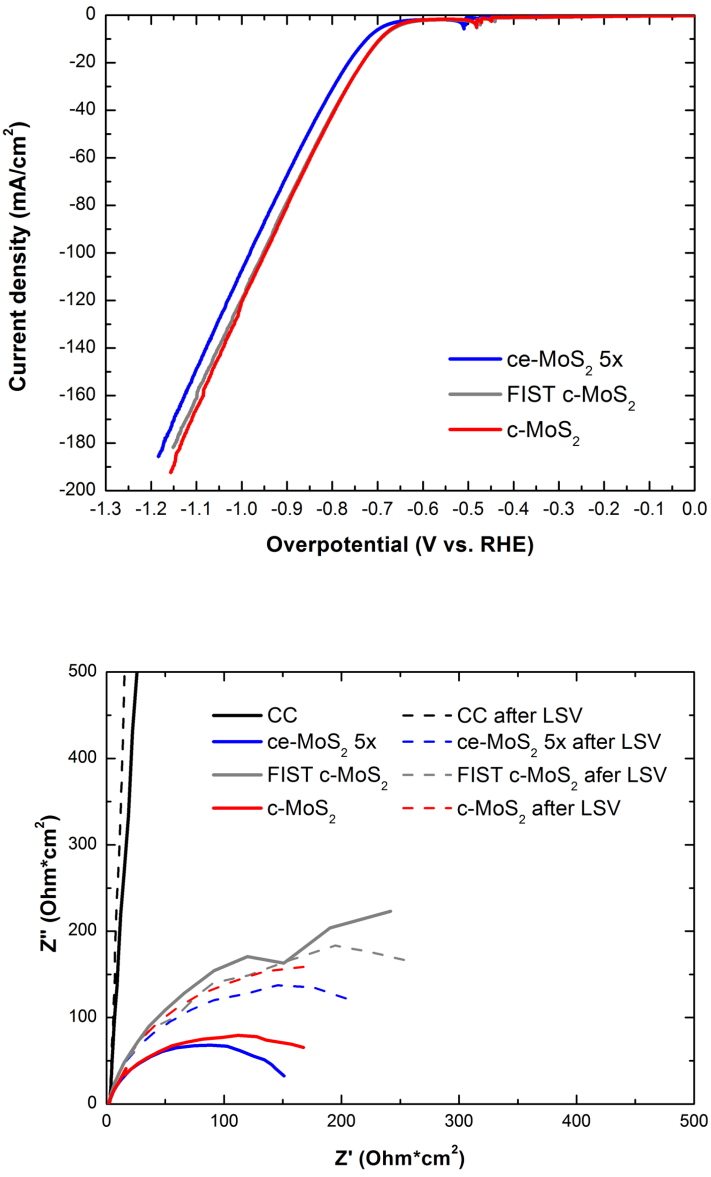

Figure 3.36. LSV plot and EIS plot.

Table 3.10. Experimental 3, conditions for effect of the number of ce-MoS_2 dip coat steps on HER activity (average data).

	Overpotential (mV)	Tafel slope (mV per dec)	Exchange current density ($\mu A/cm^2$)	Charge-transfer resistance (Ω)	Capacitance (mF/cm^2)	Mass loading ($\mu g/cm^2$)	Cycles	EHD Temperature (˚C)	Dip coat Temperature (˚C)
c-MoS_2 on ce-MoS_2 5x	-745	134.2	0.0276	>200	21.2	30.8	1	25˚C	25˚C
FIST c-MoS_2 on ce-MoS_2 5x	-735	135.2	0.0359	>300	31.7	28.2	1	25˚C	25˚C
ce-MoS_2 5x	-761	147.8	0.0687	150	16.3	N/A	1	N/A	25˚C
CC	N/A	N/A	N/A	>50,000	0.625	N/A	1	N/A	N/A

Note: The mass loading of c-MoS_2 before FIST process is between 23 to 39 $\mu g/cm^2$.

Table 3.11. Experimental 3, conditions for effect of the number of ce-MoS_2 dip coat steps on HER activity (all samples).

	Overpotential (mV)	Tafel slope (mV per dec)	Exchange current density ($\mu A/cm^2$)	Solution resistance (Ω)	Charge-transfer resistance (Ω)	Capacitance (mF/cm^2)	Mass loading ($\mu g/cm^2$)	Cycles	EHD Temperature (˚C)	Dip coat Temperature (˚C)
c-MoS_2 on ce-MoS_2 5x 3.1	-743	131.7	0.0222	1.98	180	16.1	30.8	1	25˚C	25˚C
c-MoS_2 on ce-MoS_2 5x 3.2	-745	141.3	0.0520	1.97	>250	27.5	23.1	1	25˚C	25˚C
c-MoS_2 on ce-MoS_2 5x 3.3	-746	129.4	0.0168	1.77	200	21.3	38.5	1	25˚C	25˚C
FIST c-MoS_2 on ce-MoS_2 5x 3.1	-741	130.0	0.00600	1.85	>300	25.6	30.8	1	25˚C	25˚C
FIST c-MoS_2 on ce-MoS_2 5x 3.2	-734	139.1	0.0516	1.94	>250	32.2	30.8	1	25˚C	25˚C
FIST c-MoS_2 on ce-MoS_2 5x 3.3	-731	135.5	0.0395	1.66	>200	40.8	23.1	1	25˚C	25˚C
ce-MoS_2 5x 3.1	-756	146.8	0.0690	1.89	160	25.6	N/A	1	N/A	25˚C
ce-MoS_2 5x 3.2	-777	174.7	0.343	1.85	200	15.6	N/A	1	N/A	25˚C
ce-MoS_2 5x 3.3	-755	130.1	0.0155	2.09	150	11.4	N/A	1	N/A	25˚C
CC	N/A	N/A	N/A	2.01	>50,000	0.625	N/A	1	N/A	N/A

Figure 3.37 shows LSV plot and EIS plot of FIST c-MoS_2 on ce-MoS_2 dip coat 1 time, c-MoS_2 on ce-MoS_2 dip coat 1 time, and ce-MoS_2 dip coat 1 time on carbon cloth. Each plot shows data averaged from 3 samples. **EIS is performed at 0 V vs. Ag/AgCl.** Overpotential at 10 mA/cm^2, Tafel slope and exchange current density of all the MoS_2 catalysts are similar. The slight differences in behavior exhibited by the catalysts could be due to a slight difference in mass and surface area of ce-MoS_2 on carbon cloth. The data are summarized in Table 3.12 and 3.13.

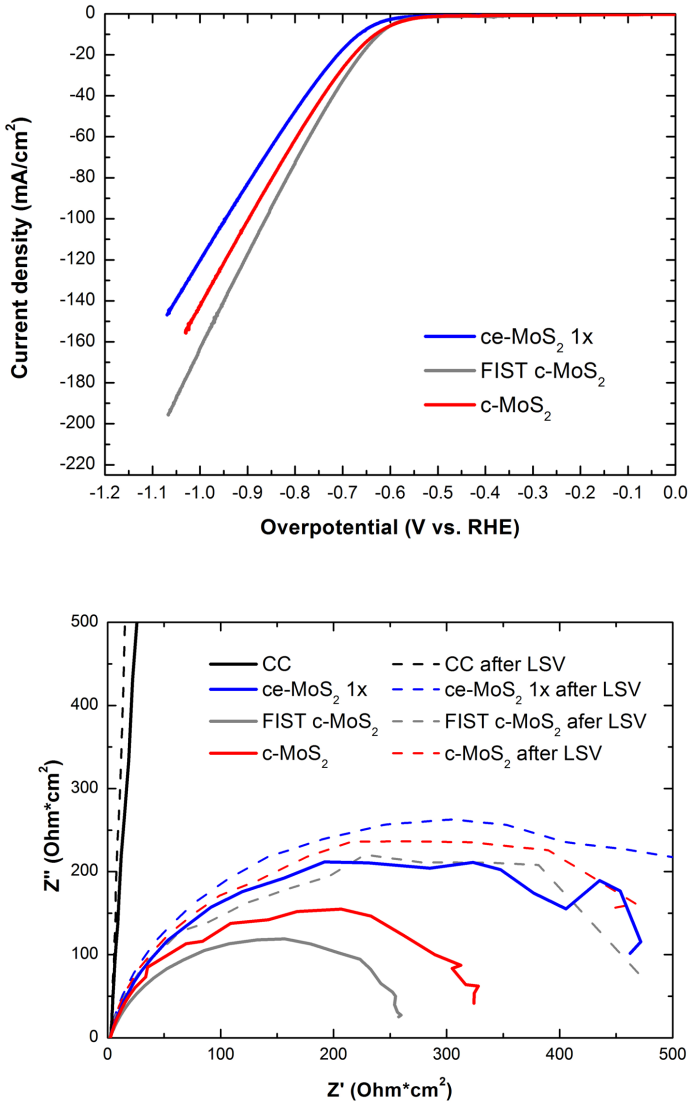

Figure 3.37. LSV plot and EIS plot.

Table 3.12. Experimental 3, conditions for effect of the number of ce-MoS_2 dip coat steps on HER activity (average data).

	Overpotential (mV)	Tafel slope (mV per dec)	Exchange current density ($\mu A/cm^2$)	Solution resistance (Ω)	Charge-transfer resistance (Ω)	Capacitance (mF/cm^2)	Mass loading ($\mu g/cm^2$)	Cycles	EHD Temperature (˚C)	Dip coat Temperature (˚C)
c-MoS_2 on ce-MoS_2 1x	-631	127	0.104	2.14	340	3.60	25.6	1	25˚C	25˚C
FIST c-MoS_2 on ce-MoS_2 1x	-624	99.7	0.00560	1.92	250	3.09	28.2	1	25˚C	25˚C
ce-MoS_2 1x	-666	114	0.0149	2.12	500	3.52	N/A	1	N/A	25˚C
CC	N/A	N/A	N/A	2.01	>50,000	0.625	N/A	1	N/A	N/A

Note: The mass loading of c-MoS_2 before FIST process is between 23 to 39 $\mu g/cm^2$.

Table 3.13. Experimental conditions for effect of the number of ce-MoS_2 dip coat steps on HER activity (all samples).

	Overpotential (mV)	Tafel slope (mV per dec)	Exchange current density ($\mu A/cm^2$)	Solution resistance (Ω)	Charge-transfer resistance (Ω)	Capacitance (mF/cm^2)	Mass loading ($\mu g/cm^2$)	Cycles	EHD Temperature (˚C)	Dip coat Temperature (˚C)
c-MoS_2 on ce-MoS_2 1x 3.1	-678	108	0.00526	2.07	250	5.70	23.1	1	25˚C	25˚C
c-MoS_2 on ce-MoS_2 1x 3.2	-682	99.6	0.00145	1.97	360	4.60	30.8	1	25˚C	25˚C
c-MoS_2 on ce-MoS_2 1x 3.3	-556	97.4	0.0206	2.37	360	2.77	23.1	1	25˚C	25˚C
FIST c-MoS_2 on ce-MoS_2 1x 3.1	-629	99.5	0.00485	2.05	310	2.63	23.1	1	25˚C	25˚C
FIST c-MoS_2 on ce-MoS_2 1x 3.2	-613	102	0.00947	1.99	260	3.62	23.1	1	25˚C	25˚C
FIST c-MoS_2 on ce-MoS_2 1x 3.3	-630	96.5	0.00301	1.71	210	3.14	38.5	1	25˚C	25˚C
ce-MoS_2 1x 3.1	-610	101	0.00982	2.33	540	2.37	N/A	1	N/A	25˚C
ce-MoS_2 1x 3.2	-711	108	0.00250	2.18	320	3.06	N/A	1	N/A	25˚C
ce-MoS_2 1x 3.3	-689	97.4	0.000878	1.84	540	6.79	N/A	1	N/A	25˚C
CC	N/A	N/A	N/A	2.01	>50,000	0.625	N/A	1	N/A	N/A

Overpotential at 10 mA/cm^2 of dip coat ce-MoS_2 1 time is lower than dip coat ce-MoS_2 5 times which could be due to ce-MoS_2 dip coat 1 time on carbon cloth having lower charge-transfer resistance.

3.12 Effect of the ce-MoS_2 coat drying temperature on HER activity.

Figure 3.38 shows LSV plot of FIST c-MoS_2 on ce-MoS_2 dip coat 5 times at 100˚C, c-MoS_2 on ce-MoS_2 dip coat 5 times at 100˚C, and ce-MoS_2 dip coat 5 times at 100˚C on carbon cloth. Each plot shows data averaged from 3 samples. **EIS is performed at 0 V vs. Ag/AgCl.** Overpotential at 10 mA/cm^2, Tafel slope and exchange current density of all the MoS_2 catalysts are similar. The slight differences in behavior exhibited by the catalysts could be due to a slight difference in mass and surface area of ce-MoS_2 on carbon cloth. The data are summarized in Table 3.14 and 3.15.

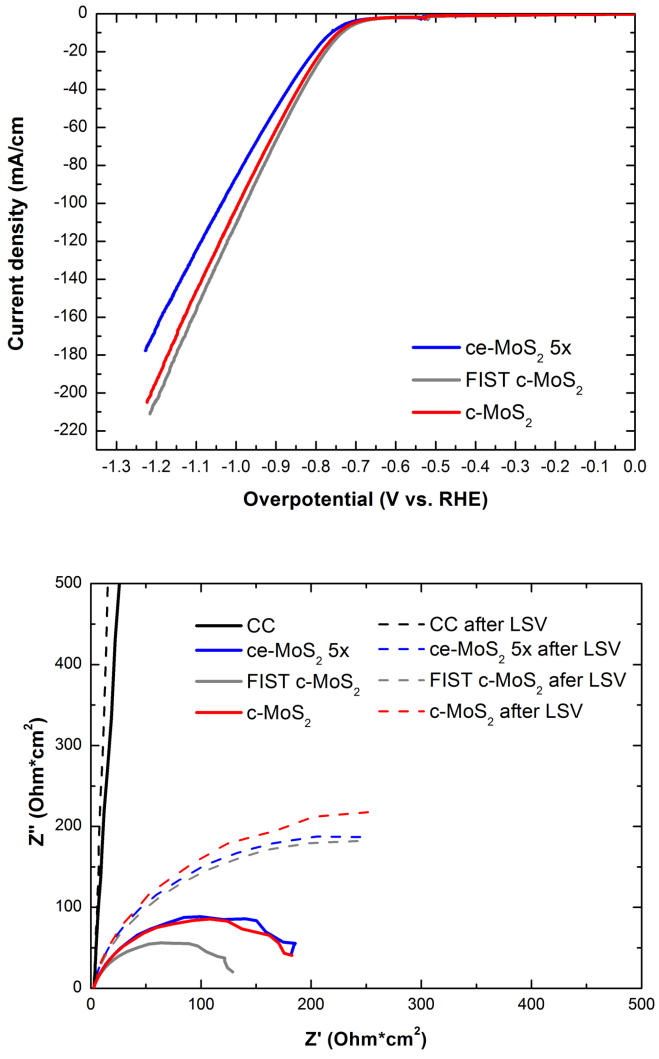

Figure 3.38. LSV plot and EIS plot.

Table 3.14. Experimental 4, conditions for effect of the ce-MoS_2 coat drying temperature on HER activity (average data).

	Overpotential (mV)	Tafel slope (mV per dec)	Exchange current density ($\mu A/cm^2$)	Solution resistance (Ω)	Charge-transfer resistance (Ω)	Capacitance (mF/cm^2)	Mass loading ($\mu g/cm^2$)	Cycles	EHD Temperature (˚C)	Dip coat Temperature (˚C)
c-MoS_2 on ce-MoS_2 5x	-695	108	0.00375	2.12	200	11.7	15.4	1	25˚C	100˚C
FIST c-MoS_2 on ce-MoS_2 5x	-693	116	0.00994	2.11	125	14.5	15.4	1	25˚C	100˚C
ce-MoS_2 5x	-724	116	0.00600	2.07	200	10.4	N/A	1	N/A	100˚C
CC	N/A	N/A	N/A	2.01	>50,000	0.625	N/A	1	N/A	N/A

The mass loading of c-MoS_2 before FIST process is 15.4 $\mu g/cm^2$.

Table 3.15. Experimental 4, conditions for effect of the ce-MoS_2 coat drying temperature on HER activity (all samples).

	Overpotential (mV)	Tafel slope (mV per dec)	Exchange current density ($\mu A/cm^2$)	Solution resistance (Ω)	Charge-transfer resistance (Ω)	Capacitance (mF/cm^2)	Mass loading ($\mu g/cm^2$)	Cycles	EHD Temperature (˚C)	Dip coat Temperature (˚C)
c-MoS_2 on ce-MoS_2 5x 4.1	-676	94.9	0.000768	2.26	250	11.3	15.4	1	25˚C	100˚C
c-MoS_2 on ce-MoS_2 5x 4.2	-704	108	0.00310	2.14	250	9.42	15.4	1	25˚C	100˚C
c-MoS_2 on ce-MoS_2 5x 4.3	-706	122	0.0156	1.97	140	17.2	15.4	1	25˚C	100˚C
FIST c-MoS_2 on ce-MoS_2 5x 4.1	-672	102	0.00254	2.43	100	16.5	15.4	1	25˚C	100˚C
FIST c-MoS_2 on ce-MoS_2 5x 4.2	-709	123	0.0169	1.90	110	17.7	15.4	1	25˚C	100˚C
FIST c-MoS_2 on ce-MoS_2 5x 4.3	-700	119	0.0122	2.01	200	11.1	15.4	1	25˚C	100˚C
ce-MoS_2 5x 4.1	-710	96.3	0.000436	2.34	300	6.97	N/A	1	N/A	100˚C
ce-MoS_2 5x 4.2	-728	126	0.0157	1.89	140	13.4	N/A	1	N/A	100˚C
ce-MoS_2 5x 4.3	-734	139	0.0513	1.98	150	12.8	N/A	1	N/A	100˚C
CC	N/A	N/A	N/A	2.01	>50,000	0.625	N/A	1	N/A	N/A

Exchange current density of dip coat ce-MoS_2 5 times at room temperature is higher than dip coat ce-MoS_2 5 times at 100˚C, which could be due to dip coat ce-MoS_2 at room temperature preserving 1T'-MoS_2. 1T'-MoS_2 has lower ΔG_H on the basal plane compare to 2H- MoS_2 (Chou et al., 2015).

3.13 Materials selection charts

The results of this work are added to the materials selection charts from chapter 1, in which possible targets for HER catalyst improvement were identified.

Figure 3.39 to figure 3.44 show the catalytic performance of MoS_2 based HER catalysts. The numbers correspond to row numbers from Table 1.1 in chapter 1. Numbers in red, blue and magenta relate to the present work.

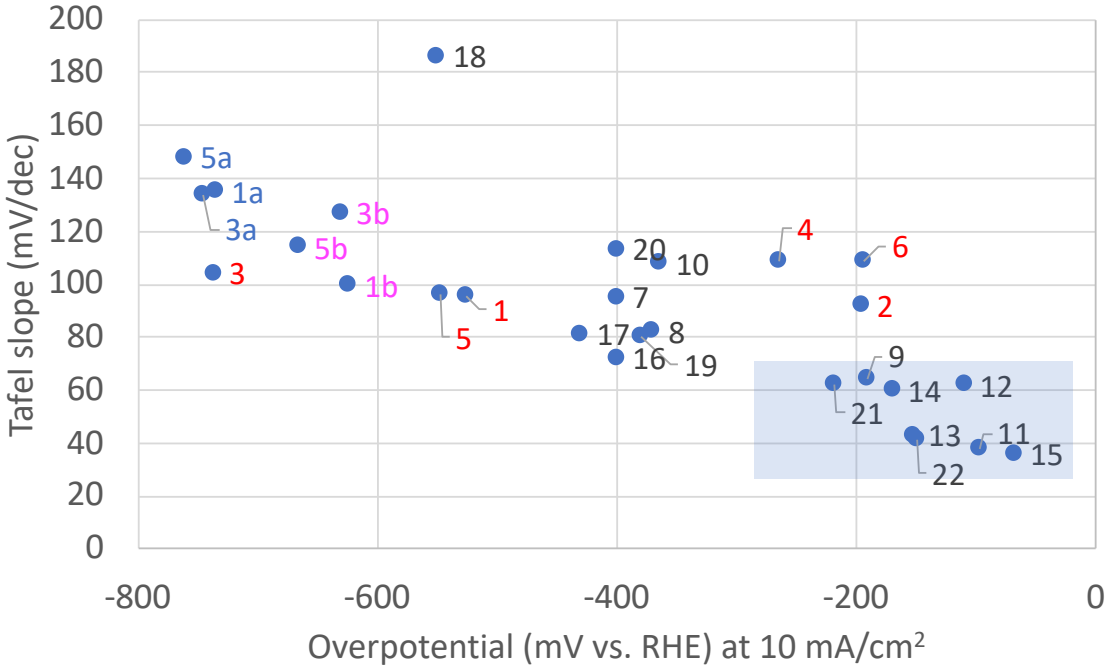

Figure 3.39. Overpotential at 10 mA/cm^2 and Tafel slope of MoS_2 based HER catalysts. The shaded area denotes the promising HER catalyst because small overpotential (absolute value) and Tafel slope are desired for HER catalyst. Within this shaded area, (i) the minimum of the overpotential is the overpotential at 10 mA/cm^2 of Pt wire (Chhetri et al., 2017); (ii) the maximum of the overpotential is the overpotential at 10 mA/cm^2 of most MoS_2 based catalysts; (iii) the minimum of Tafel slope is the Tafel slope of Pt wire (Kong et al., 2014); and (iv) the maximum of Tafel slope is the Tafel slope of most MoS_2 based catalysts. The Tafel slope from this work is considered high. The coverage of c-MoS_2 can be further optimized to reduce Tafel slope.

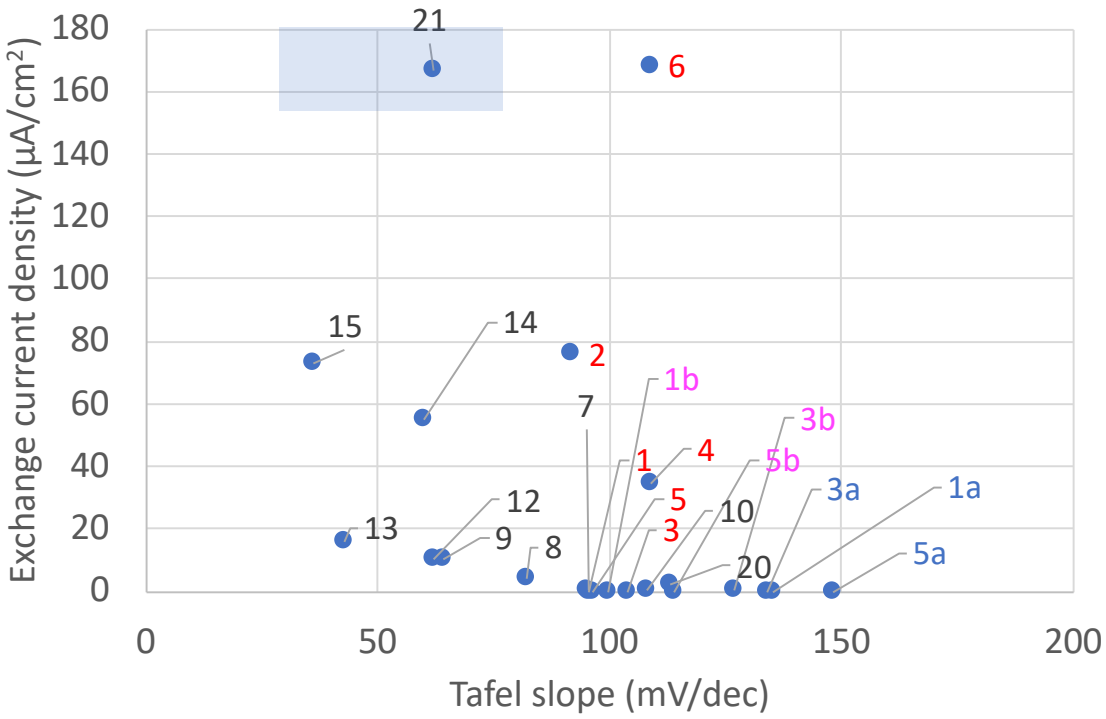

Figure 3.40. Exchange current density and Tafel slope of MoS_2 based HER catalysts. The shaded area denotes the promising HER catalyst because small Tafel slope and large exchange current density are desired for HER catalyst. Within this shaded area, (i) the minimum of exchange current density is the exchange current density of Li-MoS_2 on carbon fiber paper (Wang et al. 2013); (ii) the maximum of exchange current density is the exchange current density of 10 wt% Pt/C (Hsu et al., 2012). The shade area of Tafel slope is the same as figure 3.39. The large exchange current density of MoS_2 based catalysts after cyclic voltammetry (Number 2, 4 and 6) from this work stems from an increasing in the surface area of MoS_2 catalysts.

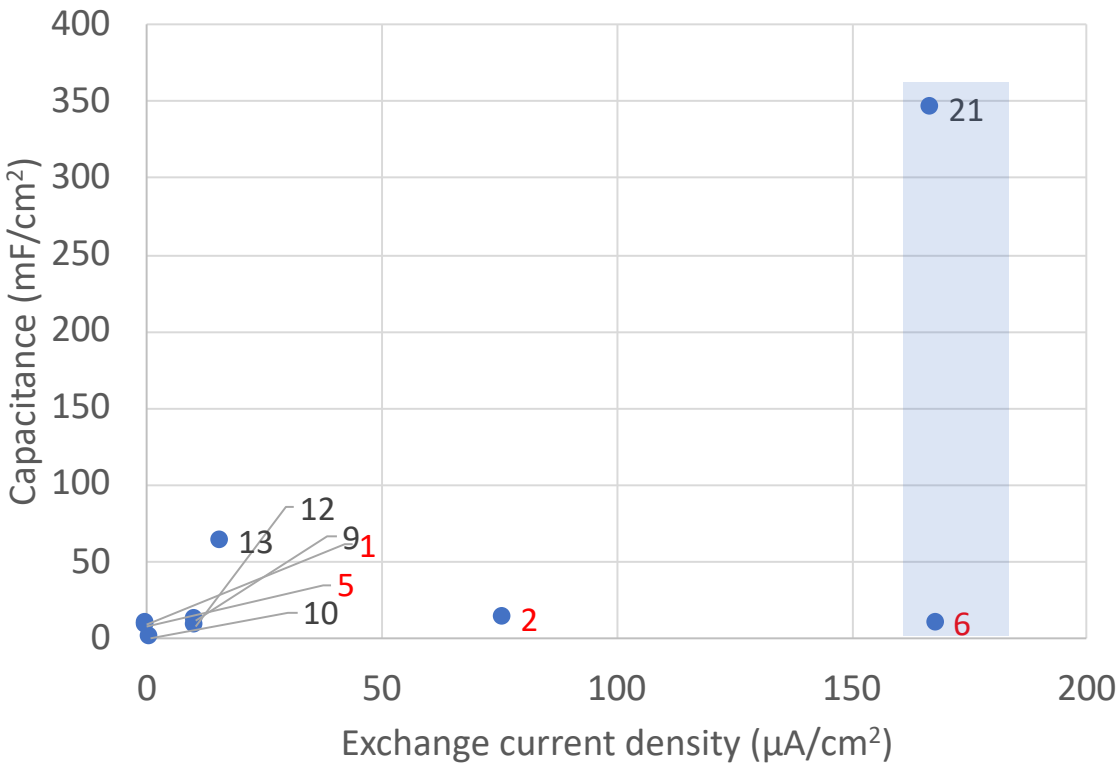

Figure 3.41. Capacitance and exchange current density of MoS_2 based HER catalysts. The shaded area denotes the promising HER catalyst because large capacitance and exchange current density are desired for HER catalyst. Within this shaded area, (i) the minimum of capacitance is the capacitance of most MoS_2 based catalysts; (ii) the maximum of capacitance is the capacitance of Li-MoS_2 on carbon fiber paper (Wang et al. 2013). The shaded area of exchange current density is the same as figure 3.40. The capacitance from this work is considered low. The coverage of c-MoS_2 can be further optimized to increase the capacitance.

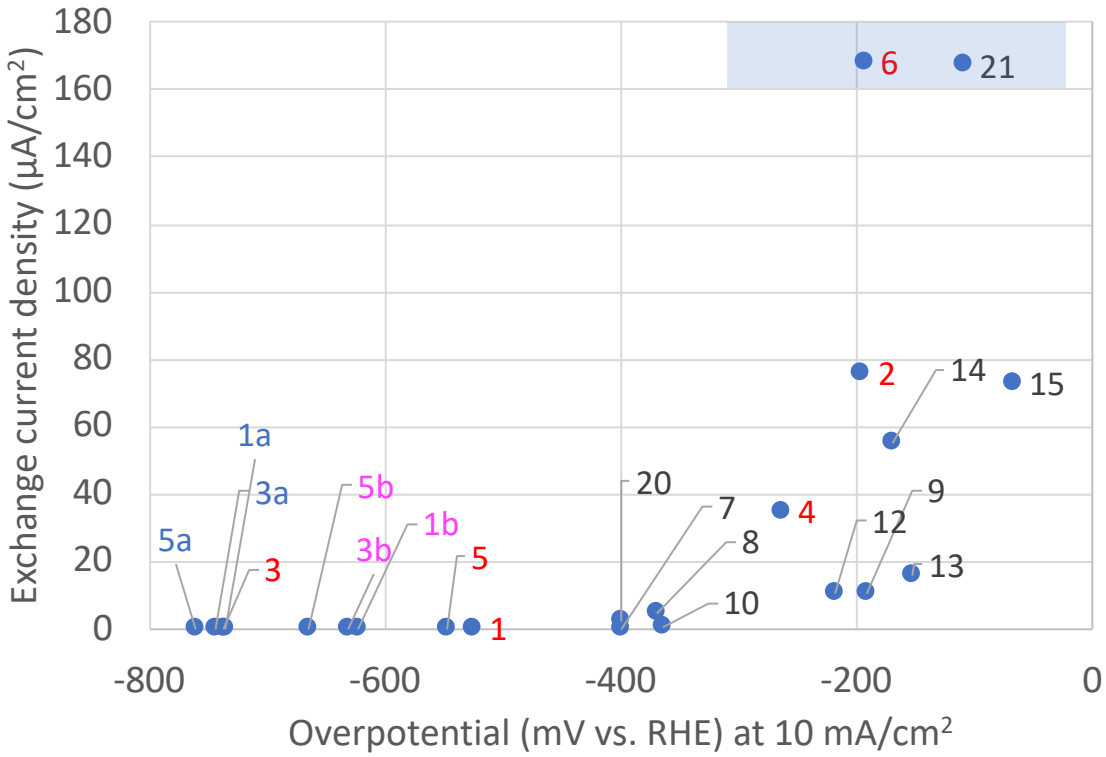

Figure 3.42. Exchange current density and overpotential of MoS_2 based HER catalysts. The shaded area denotes the promising HER catalyst because small overpotential and large exchange current density are desired for HER catalyst. The shaded area of overpotential and exchange current density are the same as figure 3.39 and 3.40, respectively. The exchange current density and overpotential at $10mA/cm^2$ of MoS_2 based catalysts after cyclic voltammetry (Number 6) from this work is in the desirable region for HER catalysts.

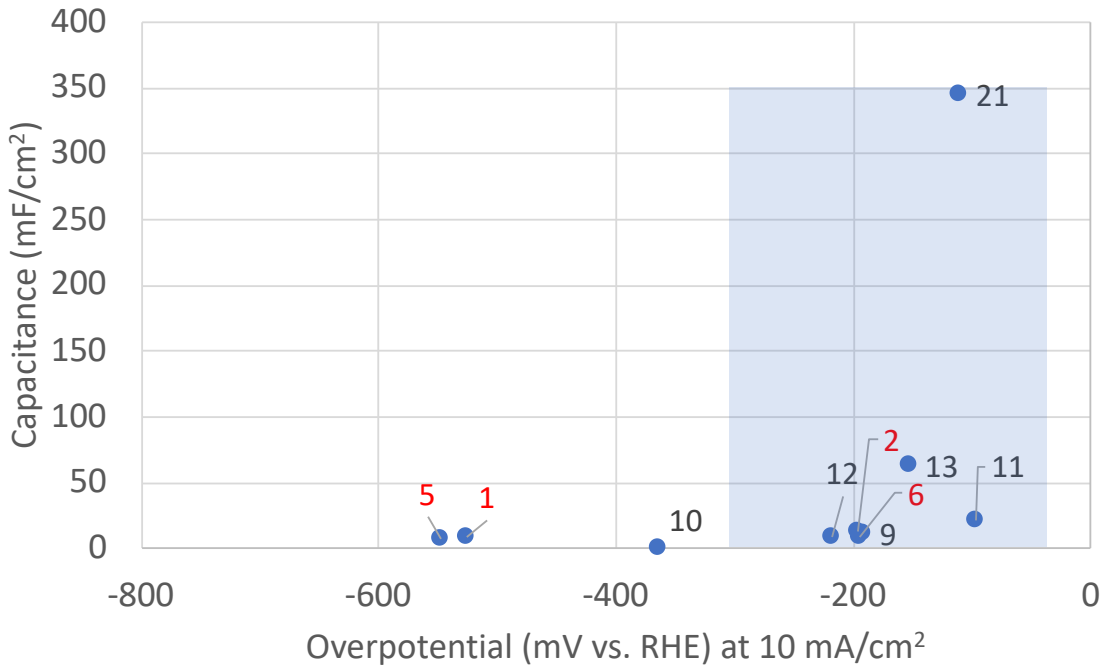

Figure 3.43. Capacitance and overpotential of MoS_2 based HER catalysts. The shaded area denotes the promising HER catalyst because small overpotential and large capacitance are desired for HER catalyst. The shaded area of overpotential and capacitance are the same as figure 3.39 and 3.41, respectively. The capacitance and overpotential at $10mA/cm^2$ of MoS_2 based catalysts after cyclic voltammetry (Number 2 and 6) from this work are in the desirable region for HER catalysts.

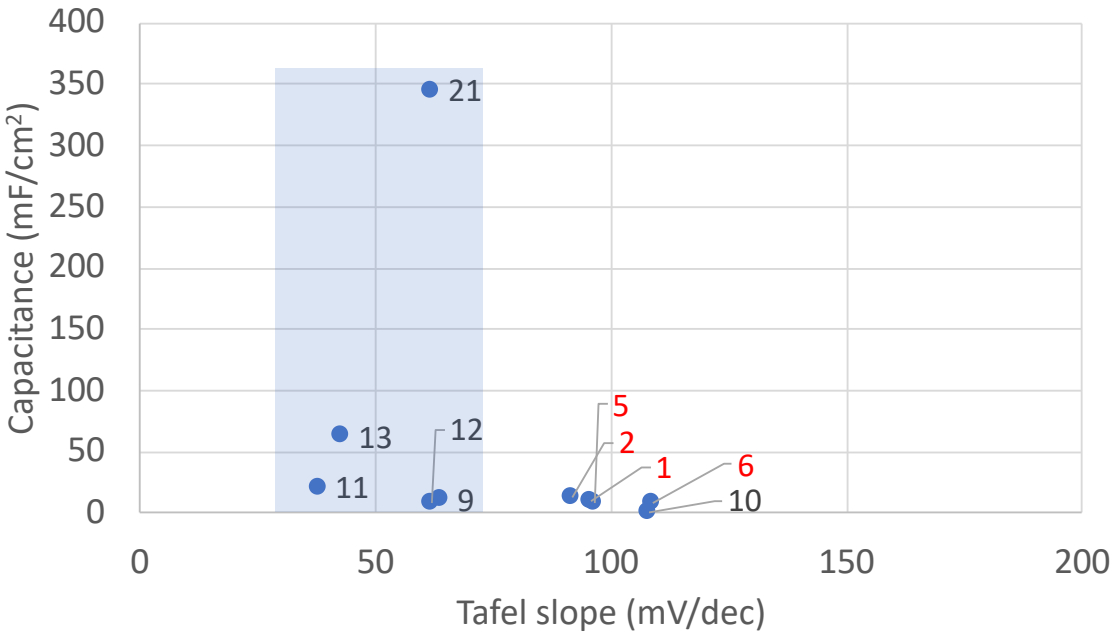

Figure 3.44. Capacitance and Tafel slope of MoS_2 based HER catalysts. The shaded area denotes the promising HER catalyst because small Tafel slope and large capacitance are desired for HER catalyst. The shaded area of Tafel slope and capacitance are the same as figure 3.39 and 3.41, respectively.

CHAPTER 4: Conclusions

[Hypothesis: High surface area and mass loading of friction induced structural transformation of crumpled MoS_2 (FIST c-MoS_2) could improve catalytic performance of the electrode for HER compared to c-MoS_2 and ce-MoS_2, by lowering the overpotential and Tafel slope.]

1. After cyclic voltammetry from 0.2 V to -0.3 V vs. RHE for 1,000 cycles, FIST c-MoS_2 on ce-MoS_2, c-MoS_2 on ce-MoS_2, and ce-MoS_2, all on carbon cloth, show similar overpotential at 10 mA/cm^2, and similar Tafel slope. The overpotential at 10 mA/cm^2 of all three catalysts is reduced after cyclic voltammetry, compared to the values beforehand, and the Tafel slope is relatively unaffected. The additional strain created in FIST c-MoS_2 structure does not have a significant effect on these measures of performance. At the same time, the observation that mechanical disturbance of c-MoS_2 does not lead to a significant *de*crease in electrode performance could be an encouraging indicator that c-MoS_2-based electrodes are robust.

2. Cyclic voltammetry leads to an increased surface area of all the MoS_2 catalysts. This conclusion is supported by capacitance data derived from EIS plots. The increased surface area promotes low overpotential at 10 mA/cm^2, and high exchange current density. From the materials selection charts in chapter 3, the MoS_2 catalysts in this work exhibit some of the lowest overpotentials at 10 mA/cm^2.

3. The decrease in the overpotential at 10 mA/cm^2 after CV 1,000 cycles could be due to the improvement in wettability.

4. The charge-transfer resistance of ce-MoS_2 on carbon cloth is lower after a single dip coating step, compared to 5 dip coating steps. The decreased charge-transfer resistance promotes low overpotential at 10 mA/cm^2, and low Tafel slope.

5. The degradation of MoS_2 catalysts after LSV is proved by charge-transfer resistance data from EIS plots: the increased charge-transfer resistance after LSV from 0 to -0.3 V vs. RHE indicates that there is a degradation of the electrodes.

CHAPTER 5: Outlook

5.1 Mass loading

In this work, mass loading of c-MoS_2 is around 0.1 of ce-MoS_2. Increasing the coverage of c-MoS_2, e.g. by electrospraying for longer times, might further reduce the Tafel slope.

5.2 Wettability

Wettability is one of the factors for lower overpotential at 10 mA/cm^2 for HER electrode. UV-ozone can be one of the methods to improve the wettability of carbon cloth or carbon paper (Bhimanapati et al., 2016). UV-ozone modification of mechanically exfoliated MoS_2 introduced S-O bonding (Azcatl et al., 2015) which reduced the contact angle of water and improved the wettability (Bhimanapati et al., 2016)). Addou et al. reported that UV-ozone treatment for 60 minutes can cause oxidation of the molybdenum in MoS_2 (Addou et al., 2015). The duration of exposure to UV-ozone can be adjusted to prevent molybdenum oxidation in MoS_2.

5.3 Pretreatment of the electrode

Negative potential can be applied to the electrode for different periods of time to test whether the pretreatment is a time-dependent process.

5.4 Effect of the temperature on HER activity

The temperature of the reaction can be varied to test whether the HER activity of MoS_2 catalyst is a temperature-dependent process.

5.5 Conducting support

Zhao et al. and Li et al. reported lower charge-transfer resistance, lower overpotential at 10 mA/cm^2 and lower Tafel slope of a hydrothermally blended hybrid of MoS_2 and reduced graphene oxide (Zhao et al., 2015; Li et al., 2011). However, the synthesis temperature of this MoS_2 hybrid is 200˚C, and the phase of MoS_2 is 2H phase. This leaves open the possibility that further lowering of the overpotential at 10 mA/cm^2 might be achievable if the phase of MoS_2 in the hybrid could be 1T'. The catalyst in the present work is synthesized at room temperature, thus preserving the 1T' phase after chemical exfoliation with lithium. The crumple structure of 1T'-MoS_2 hybrid with reduced graphene oxide has the potential to improve the catalytic performance of HER electrode.

5.6 Cobalt-modified MoS_2

ΔG_H close to 0 eV is desired for HER. Lower ΔG_H will lead to high surface coverage of hydrogen atoms adsorbed at the electrode surface, while larger ΔG_H will make the hydrogen atoms bond too weakly on the catalyst surface, thus slowing the HER kinetics (Gao et al., 2015). Bonde et al. reported that incorporation of cobalt into the MoS_2 can reduce ΔG_H at the S-edge from 0.18 eV to 0.10 eV (Bonde et al., 2008). Gao et al. reported lower overpotential at 10 mA/cm^2 and Tafel slope of MoS_2/$CoSe_2$ hybrid catalyst (Gao et al., 2015). However, the synthesis temperature of this MoS_2/$CoSe_2$ hybrid catalyst is 180˚C, and the phase of MoS_2 is 2H phase. The crumple structure of

1T'-MoS_2/$CoSe_2$ hybrid catalyst has the potential to improve the catalytic performance of HER electrode.

5.7 Preventing hydrogen bubbles from accumulating at the electrode surface
A rotating disk electrode (RDE) can be used to prevent hydrogen bubbles from accumulating at the electrode surface and blocking the active area for HER (Benck et al., 2014).

5.8 Substrate, geometric surface area and mass loading
In order to compare the exchange current density with others, the same conditions of substrate, geometric surface area and mass loading are required.

5.9 Surface characterization
X-ray photoelectron spectroscopy (XPS) can be performed before and after CV 1,000 cycles to explore whether cycling-dependent proton intercalation could provide an alternative to increased catalyst surface area as an explanation for the decrease in overpotential at 10 mA/cm^2 (Li et al., 2017).

5.10 Charge transfer resistance of the electrode before and after CV 1,000 cycles
EIS measurement can be performed at the same constant voltage (i.e. not the open circuit potential) before and after CV 1,000 cycles to compare charge-transfer resistance.

5.11 Possibility of scalable HER catalyst preparation
The synthesis of all the MoS_2 catalysts in this work is performed at room temperature, which could preserve the 1T'- MoS_2. These MoS_2 catalyst synthesis methods provide the possibility of scalable HER catalyst preparation.

REFERENCES

Abbott, D. et al., 1996. Simple Derivation of the Thermal Noise Formula Using Window-Limited Fourier Transforms and Other Conundrums. *IEEE Transaction on Education*, 39(1), pp.1-13.

Addou, R. et al., 2015. Impurities and Electronic Property Variations of Natural MoS_2 Crystal Surfaces. *ACS Nano.*, 9 ,9, pp.9124–9133.

Ali et al., 2012. Spin-on doping (SOD) and diffusion temperature effect on re-combinations/ideality factor for solar cell applications. *Chalcogenide Letters*, 9, 11, pp.457-463.

Allen, M.J. et al., 2009. Soft Transfer Printing of Chemically Converted Graphene. *Adv. Mater.*, 21, pp.2098–2102.

Azcatl, A., et al., 2015. HfO_2 on UV–O_3 exposed transition metal dichalcogenides: interfacial reactions study. *2D Mater.,* 2, pp.014004-014012.

Badwal, S.P.S. et al., 2014. Emerging electrochemical energy conversion and storage technologies. *Frontiers in Chemistry*, 2(79), pp.1-28.

Bard, A.J. et al., 1980. Electrochemical Methods: Fundamentals and Applications. John Wiley & Sons, Inc.

Benck, J.D. et al., 2014. Catalyzing the Hydrogen Evolution Reaction (HER) with Molybdenum Sulfide Nanomaterials. *ACS Catal.*, 4, pp.3957-3971.

Bhimanapati, G.R. et al., 2016. Growth and Tunable Surface Wettability of Vertical MoS_2 Layers for Improved Hydrogen Evolution Reactions *ACS Appl. Mater. Interfaces*, 8, 34, pp.22190-22195.

Bohning, J.J. et al., 1998. The Raman Effect. American Chemical Society International Historic Chemical Landmarks.

Bonde, J. et al., 2008. Hydrogen evolution on nano-particulate transition metal sulfides. *Faraday Discuss.*, 140, pp.219–231.

Bowen, D.K. et al., 1975. Microscopy of Materials. The Macmillan Press Ltd.

Callister, W.D., et al., 2014. Materials Science and Engineering - An Introduction. John Wiley & Sons, Inc.

Castellanos-Gomez, A. et al., 2013. Local Strain Engineering in Atomically Thin MoS_2. *Nano Lett.*, 13, pp.5361−5366.

Chakraborty, B. et al., 2012. Symmetry-dependent phonon renormalization in monolayer MoS_2 transistor. *Physical review B*, 85, pp.161403-1-4.

Chen, Z. et al., 2011. Core-shell MoO_3-MoS_2 Nanowires for Hydrogen Evolution: A Functional Design for Electrocatalytic Materials. *Nano Lett.*, 11, pp.4168–4175.

Chen, Y.-C. et al., 2017. Structurally Deformed $MoS_2$for Electrochemically Stable, Thermally Resistant, and Highly Efficient Hydrogen Evolution Reaction. *Adv. Mater.*, 29, pp.1703863-1703873.

Chhetri, M. et al., 2017. Electrocatalytic hydrogen evolution reaction activity comparable to platinum exhibited by the Ni/$Ni(OH)_2$/graphite electrode. *PNAS.*, pp. 1710443114-170443119.

Chhowalla, M. et al., 2013. The chemistry of two-dimensional layered transition metal dichalcogenide nanosheets. *Nature Chemistry*, 5, pp.263–275.

Chia, X. et al., 2014. Precise Tuning of the Charge Transfer Kinetics and Catalytic Properties of MoS_2 Materials via Electrochemical Methods. *Chem. Eur. J.*, 20, pp.17426-17432.

Chia, X. et al., 2015. Catalytic and Charge Transfer Properties of Transition Metal Dichalcogenides Arising from Electrochemical Pretreatment. *ACS Nano*, 9(5), pp.5164-5179.

Chou, S.S. et al., 2015. Understanding catalysis in a multiphasic two-dimensional transition metal dichalcogenide. *Nature Communications*, 6, pp.8311-8318.

Conway, B.E. et al., 2002. Interfacial processes involving electrocatalytic evolution and oxidation of H_2, and the role of chemisorbed H. *Electrochimica Acta*, 47, pp.3571-3594.

Deng, J. et al., 2014. Highly active and durable non-precious-metal catalysts encapsulated in carbon nanotubes for hydrogen evolution reaction. *Energy Environ. Sci.*, 7, pp.1919-1923.

Dhas, N.A. et al., 2005. Sonochemical Preparation of Hollow Nanospheres and Hollow Nanocrystals. *J. Am. Chem. Soc.*, 127, pp.2368-2369.

Ding, Q. et al., 2016. Efficient Electrocatalytic and Photoelectrochemical Hydrogen Generation Using MoS_2 and Related Compounds. *Chem 1*, pp.699-726.

Gao, M.-R. et al., 2015. An efficient molybdenum disulfide/cobalt diselenide hybrid catalyst for electrochemical hydrogen generation. *Nature Communication*, 6, pp.5982-5988.

Hafner, B., 2007. Scanning Electron Microscopy Primer. Characterization Facility, University of Minnesota—Twin Cities.

Hsu, I.J. et al., 2012. Atomic layer deposition synthesis of platinum–tungsten carbide core–shell catalysts for the hydrogen evolution reaction. *Chem. Commun.*, 48, pp.1063–1065.

Ishihara, H. et al., 2016. Electrohydrodynamic-assisted Assembly of Hierarchically Structured, 3D Crumpled Nanostructures for Efficient Solar Conversions. *Sci. Rep.*, *6*, pp.38701-38712.

Jaramillo, T.F. et al., 2007. Identification of active edge sites for electrochemical H_2 evolution from MoS_2 nanocatalysts. *Science*, 317, pp.100–102.

Jaworek, A., 2007. Electrospray droplet sources for thin film deposition. *J. Mater. Sci.*, 42, pp.266–297.

Jaworek, A. et al., 2008. Electrospraying route to nanotechnology: An overview. *Journal of Electrostatics*, 66, pp.197-219.

Joensen, P. et al., 1987. A study of single-layer and restacked MoS_2 by X- ray diffraction and X-ray absorption spectroscopy. *J. Phys. C: Solid State Phys.,* 20, pp.4043-4053.

Kong, D., et al., 2013. Synthesis of MoS_2 and $MoSe_2$ Films with Vertically Aligned Layers. *Nano Lett.*, 13, pp.1341−1347.

Kong, D. et al., 2014. $CoSe_2$ Nanoparticles Grown on Carbon Fiber Paper: An Efficient and Stable Electrocatalyst for Hydrogen Evolution Reaction. *J. Am. Chem. Soc.*, 136, pp.4897−4900.

Late, D.J. et al., 2012. Rapid Characterization of Ultrathin Layers of Chalcogenides on SiO_2/Si Substrates. *Adv. Funct. Mater.*, 22, pp.1894–1905.

Lauhon, L.J. et al., 2002. Epitaxial core–shell and core– multishell nanowire heterostructures. *Nature*, 420, pp.57-61.

Lennard-Jones, J.E., 1931. Cohesion. *Proc. Phys. Soc.*, 43, pp.461-482.

Li, G. et al., 2017. Activating MoS_2 for pH-Universal Hydrogen Evolution Catalysis. *J. Am. Chem. Soc.*, 139, pp.16194-16200.

Li, H., et al., 2016. Activating and optimizing MoS_2 basal planes for hydrogen evolution through the formation of strained sulfur vacancies. *Nat Mater.*, 15, pp.48-54.

Li, Y. et al., 2010. Hydrogen generation from photoelectrochemical water splitting based on nanomaterials. *Laser Photonics Rev. 4*, 4, pp.517–528.

Li, Y. et al., 2011. MoS_2 Nanoparticles Grown on Graphene: An Advanced Catalyst for the Hydrogen Evolution Reaction. *J. Am. Chem. Soc.*, 133, pp.7296–7299.

Lindsay, S.M., 2010. Introduction to Nanoscience. Oxford University Press Inc.

Luo, J. Y et al., 2011. Compression and Aggregation- Resistant Particles of Crumpled Soft Sheets. *ACS Nano*, 5, pp.8943– 8949.

Ma, L. et al., 2015. Efficient hydrogen evolution reaction catalyzed by molybdenum carbide and molybdenum nitride nanocatalysts synthesized via the urea glass route. *J. Mater. Chem. A*, 3, pp.8361-8369.

Nipane, A. et al., 2016. Few-Layer MoS_2 p-Type Devices Enabled by Selective Doping Using Low Energy Phosphorus Implantation. *ACS Nano.*, 10, pp.2128−2137.

Norskov, J. K. et al., 2005. Trends in the Exchange Current for Hydrogen Evolution. *Journal of The Electrochemical Society*, 152(3), pp.J23-J26.

Novoselov, K. S. et al., 2005. Two-dimensional atomic crystals. *PNAS.*, 102(30), pp.10451-10453.

Nyquist, H., 1932. *Regeneration Theory. Bell System Tech. J.*, 11(1), pp.126-147.

O'Hayre, R. et al., 2009. Fuel Cell Fundamentals. John Wiley & Sons, Inc.

Ottaviano, L. et al., 2017. Mechanical exfoliation and layer number identification of MoS2 revisited. *2D Mater.*, 4, pp.045013-045027.

Raman, C.V. et al., 1928. A New Radiation. *Indian J. Phys.*, 2*,* pp.387-396.

Rice, C. et al., 2013. Raman-scattering measurements and first-principles calculations of strain-induced phonon shifts in monolayer MoS_2. *Physical Review B*, 87, pp.081307(R).

Suen, N.-T. et al., 2017. Electrocatalysis for the oxygen evolution reaction: recent development and future perspectives. *Chem. Soc. Rev.*, 46, pp.337-365.

Tao, A.R. et al., 2008. Self-Organized Silver Nanoparticles for Three- Dimensional Plasmonic Crystals. *Nano Lett.*, 8, pp.4033–4038.

Tao, Y et al., 2013. Towards Ultrahigh Volumetric Capacitance: Graphene Derived Highly Dense but Porous Carbons for Supercapacitors. *Sci. Rep.*, 3, pp.2975-2983.

Temenoff, J.S. et al., 2009. Biomaterials: The Intersection of Biology and Materials Science. Pearson.

Tsai, C. et al., 2014a. Active edge sites in $MoSe_2$ and WSe_2 catalysts for the hydrogen evolution reaction: a density functional study. *Phys.Chem.Chem.Phys.*, 16, pp.13156-13164.

Tsai, C. et al., 2014b. Tuning the MoS_2 Edge-Site Activity for Hydrogen Evolution via Support Interactions. *Nano Lett.*, 14, pp.1381-1387.

Tsai, C. et al., 2017. Electrochemical generation of sulfur vacancies in the basal plane of MoS_2 for hydrogen evolution. *Nature Communications.*, 8, pp. 15113-15120.

Valiev, R.Z., et al., 2014. Bulk Nanostructured Materials. *The Minerals, Metals & Materials Society,* John Wiley & Sons, Inc.

Verble, J.L. et al., 1970. Lattice Mode Degeneracy in MoS2 and Other Layer Compounds. *Phys. Rev. Lett.*, 25, pp.362-365.

Voiry, D. et al., 2013. Conducting MoS_2 Nanosheets as Catalysts for Hydrogen Evolution Reaction. *Nano Lett.*, 13, pp.6222−6227.

Wang, L. et al., 2012. Solar water splitting: preserving the beneficial smaller feature size in porous α-Fe_2O_3 photoelectrodes during annealing. *J. Mater. Chem. A*, 1, pp.212-215.

Wang, H. et al., 2013. Electrochemical tuning of vertically aligned MoS_2 nanofilms and its application in improving hydrogen evolution reaction. *PNAS.*, 110(49), pp.19701-19706.

Xiang, Z. et al., 2016. MoS_2 nanosheets array on carbon cloth as a 3D electrode for highly efficient electrochemical hydrogen evolution. *Carbon*, 98, pp.84-89.

Yin, Y. et al., 2016. Contributions of Phase, Sulfur Vacancies, and Edges to the Hydrogen Evolution Reaction Catalytic Activity of Porous Molybdenum Disulfide Nanosheets. *J. Am. Chem. Soc.*, 138, pp.7965-7972.

Zhao, Y. et al., 2015. Well-Constructed Single-Layer Molybdenum Disulfide Nanorose Cross-Linked by Three Dimensional-Reduced Graphene Oxide Network for Superior Water Splitting and Lithium Storage Property. *Sci. Rep.*, 5, pp.8722-8732.